INSTITUTE OF PHYSICS PUBLISHING NANOTECHNOLOGY
Nanotechnology **15** (2004) S303–S315 PII: S0957-4484(04)70488-2

Formation of nucleotide base-pairs at the interface of a polydiacetylene cytosine derivatized monolayer

Jie Chen[1] **and Amir Berman**[1,2,3]

[1] Department of Biotechnology Engineering and the Institute of Applied Biosciences, Ben Gurion University, Israel
[2] Stadler Minerva Centre for Mesoscopic Macromolecular Engineering and the Ilse Katz Centre for Nanoscale Science and Technology, Ben Gurion University, Israel

E-mail: aberman@bgumail.bgu.ac.il

Received 15 October 2003
Published 17 March 2004
Online at stacks.iop.org/Nano/15/S303 (DOI: 10.1088/0957-4484/15/4/035)

Abstract
Langmuir monolayers of diacetylene lipids with a cytosinyl head-group (PDC), mixed with an alcohol derivative of the same lipid (PDOH), were formed on water and on guanosine solution, and were UV polymerized *in situ*. Brewster angle microscopy (BAM), atomic force microscopy (AFM) and visible light absorption spectroscopy were performed on the monolayers. It was found that the optimal ratio for the lipid mixtures is approximately 2:1 PDC/PDOH. For lipid mixtures with different ratios, the film decomposes into phases of the preferred composition and a second phase enriched with the excess compound. The stable mixed phase exhibits a distinct striated appearance along the polymer linear direction. Films formed on guanosine-containing subphase have similar phases; however, the stable striated phase appears more developed in the direction perpendicular to the polymer chains. A specific base-pair formation at the air–solution interface between the diacetylene monolayer and the free complementary nucleoside in the solution is suggested.

1. Introduction

Molecular-level surface engineering of organic and polymeric surfaces for specific interactions is crucial for tailor-made molecular recognition reactions, signal transduction, molecular electronics and possible related applications. It is imperative that functional binding sites be densely organized on the structured surface for the enhancement of the molecular interactions, the binding capacity and the signal produced.

Formation of elaborate surface motifs and two-dimensional arrays of hydrogen bonds is an attractive route for the construction of supramolecular surface assemblies. This approach was also used for the construction of complementary nucleoside interactions in media where similar interactions between monomers in aqueous media cannot take place due to hydrogen bonding with water [1]. Specific hydrogen bondings have been demonstrated for monolayers with predictable and cooperative properties of binding with complementary molecules [2] and for such macromolecules or surfaces [3–6]. Utilization of biological macromolecules or, alternatively, biomimicking of the nucleic acid hydrogen bond motifs for the construction of organized monolayers is of particular interest due to the possibility of interfacing with biological complementary macromolecules. This in turn will enable the formation of novel hybrid materials that manifest structural and stereochemical complementarities across synthetic polymer/biomacromolecule interfaces. Studies with this perspective are diverse (for overview see [7] and references therein) and include work on the formation of molecular constructs from DNA [8, 9], the formation of monolayers from nucleotide derived lipids [10, 2, 11, 6] and the usage of DNA fragments for nanostructuring of materials and prospective bionanometric devices [12–14].

In this study Langmuir monolayers of polymerizable, amphiphilic diacetylene cytosine derivatives are formed and studied. The rationale for this choice stems from the structural

[3] Author to whom any correspondence should be addressed.

features of the polydiacetylene polymer backbone structure. It is a rigid, yne–ene polyconjugated, linear structure that tends to organize in parallel and form large crystallites both in three dimensions and on surfaces [15]. The repeating periodicity along the polymer backbone is fixed at about 5.0 Å, representing the covalent bonds that constitute the rigid backbone [16–18]. The long range order and rigidity of the polymer film provide a scaffold for the ordered assembly. The polyconjugated backbones absorb light in the visible range and provide the polydiacetylene (PDA) with photoconduction properties [19]. Upon physical deformation of the polymer backbone, absorption is blue-shifted and the formerly bluish polymer appears reddish [20]. Colour change in polydiacetylene films can be the outcome of increased temperature [21], pH, charge [22], mechanical stress [23] or specific binding that sterically strains the film [24, 25]. The latter is the basis for several biosensory applications that are based on membrane mimetic processes that take place at the artificial membrane-like interface. Typically colour changes in polydiacetylene films or vesicles are irreversible; however, reversible colour change in vesicles of polymerized hydrazide diacetylene derivatives was also observed [26].

In this paper we report a study of polymerized diacetylene monolayers with cytosine (PDC) and alcohol (PDOH) moieties as the hydrophilic head-groups. The purpose of the study is to characterize and evaluate the mixed film properties and the order that stems from the properties of the pure components and their respective miscibilities. The pure components, having identical diacetylene alkyl chains, differ in their head-groups. The surface requirement of the PDC head-group is larger than that of the diacetylenic alkyl chain, while the PDOH head-group is smaller than the alkyl chain cross-section; thus a mixture of the two compounds at a certain ratio would allow the same overall surface requirement in the head-group as in the alkyl chain region. This would prevent disorder and lead to more stable mixed monolayers. The mixed cytosine–hydroxyl polydiacetylene monolayers (PDC/PDOH) are characterized by their interactions with complementary guanosine monomer from solution. The characterization was performed both at the air–solution interface and for solid-supported films after horizontal transfer (the Langmuir–Schaffer method). *In situ* recording and analysis of the compression (π–A) isotherms and the simultaneous recording of the domain shape evolution upon compression with BAM yielded valuable insights regarding the organization of the film. Further analysis by scanning probe microscopy and visible light absorption was performed on the solid-supported films.

Overall, we demonstrated the construction of an ordered assembly of a mixed Langmuir monolayer with a near stoichiometric ratio of 2:1 to 3:1 PDC/PDOH, which is capable of specific base-pair formation. This monolayer assembly is an attractive template for hybridization of nucleotide oligomers and construction of synthetic polymer–nucleic acid structured hybrid materials.

2. Materials and methods

10,12-pentacosadiynoic acid (PCDA), cytosine, cytidine (C), adenosine (A), guanosine (G) and thymidine (T) were purchased from Fluka. Octadecyltrichlorosilane (OTS) and chloroform were purchased from Aldrich. Trizma base (2-amino-2-hydroxymethyl-1,3-propanediol) was purchased from Sigma (USA).

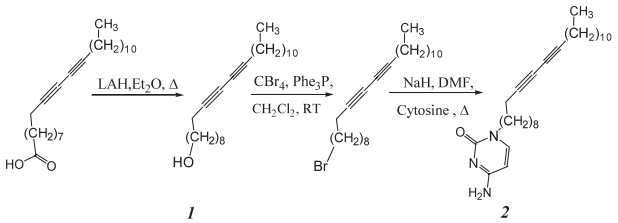

Scheme 1. Synthesis pathways for PDOH (***1***) and PDC (***2***).

The water used in this study was purified with a Milli-Q purification system and had a resistance of 18.2 mΩ cm^{-1}.

2.1. Synthesis

PCDA was used as the starting material for the synthesis of the pentacosadiyne–cytosinyl derivative (PDC, ***2***). The synthesis procedure was carried out in two steps. In the first, PCDA carboxylic acid was reduced to the alcohol derivative (PDOH, ***1***) by heating the PCDA diethyl-ether solution with lithium aluminium hydride for 12 h in reflux [27]. The product was the starting material for the second step but was also used as it is in diacetylene lipid mixtures. Alkylation of cytosine was carried out according to a reported procedure [28]. Briefly, PDOH was brominated by stirring with CBr_4 and a 1:1 stoichiometric ratio triphenylphosphine in dichloromethane solution at room temperature until reaction completion occurred (about 2 h). In the final alkylation step, cytosine was reacted with the brominated diacetylene lipid (PDBr). PDBr was added to a suspension of cytosine and sodium hydride in dimethylformamide (DMF) at room temperature and was stirred at RT for 24 h.

2.2. Preparation of the hydrophobized glass substrate

Microscope glass slides (0.15 mm thick) were cleaned in 'Piranha' solution (7:3 H_2SO_4/H_2O_2; caution: corrosive solution) for 90 min at 70 °C and were thoroughly rinsed with distilled water and oven dried (70 °C). The freshly cleaned slides were immersed in dilute solution (3:1000) of OTS in cyclohexane for 12 h. The slides were rinsed with pure cyclohexane to remove unbound OTS and were stored in cyclohexane until used.

2.3. Langmuir trough and film preparation

A Nima Langmuir film balance (50×7.5 cm^2) with symmetric compression was used. The trough was equipped with a Wilhelmy pressure sensor; 1 cm wide filter paper was used as a Wilhelmy plate.

A Brewster angle microscope, BAM2+ (NanoFilm Technology, Götingen, Germany) was operated during the compression of the PDC/PDOH mixed monolayers. The BAM and the Langmuir trough were vibration isolated with a Halcyonics MOD-2 active antivibration system.

2 mM total lipid concentration solutions in chloroform were used as spreading solutions. Pressure–area isotherms

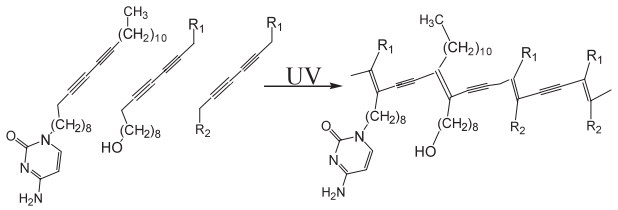

Scheme 2. Photocopolymerization of diacetylene monomers, with cytosine and alcohol head-groups depicted (R_1 = undecyl moiety; R_2 = cytosinyl or alcohol).

were produced on pure 0.05 M Trizma buffer (pH = 7.5, adjusted with HCl) or in the presence of 5 mM guanosine in the subphase buffered solution, at 25 °C. After spreading, 15 min were allowed for solvent evaporation before the compression commenced. The compression rate was 1.5 Å^2 molecule^{-1} min^{-1}. The films were compressed until collapse for the recording of complete isotherms, or until a uniform condensed monolayer was formed (at a surface pressure of 25 mN m^{-1} and as determined by BAM observations) for further analysis on a solid support. The compressed Langmuir films were polymerized at the air–solution interface with a hand-held UV lamp (λ = 254 nm) for 30 s, until the film turned pink.

2.4. Visible light spectroscopy

Visible light absorption spectroscopy was performed on a HP 8452A diode array UV–visible spectrophotometer. Photopolymerized monolayer films, transferred onto OTS-treated glass using a Langmuir–Schaffer horizontal transfer technique, were analysed.

2.5. AFM

AFM analyses were performed using a Park CP research AFM. The scanning modes were non-contact or with intermittent contact (tapping) in air. SiN_3 general purpose cantilevers (Veeco) with a 0.03 N m^{-1} force constant were used for scanning at 1–5 Hz rates, depending on the scan size.

3. Results and discussion

3.1. Pressure–area isotherms

A series of 11 PDC/PDOH spreading solutions were tested. PDC molar fractions varied from 0 to 100% with 10% increments (figure 1(a)). The corresponding compressibilities for the π–A isotherms were calculated as $C = -(1/A)(\partial A/\partial \pi)$ (figure 1(b)). The limiting areas (A_L) for the liquid condensed (LC) phase for each isotherm, as well as other transitions that took place during compression, were determined by calculation of the intercept of the tangent at the point of minimum compressibility with the area axis (figure 1(c)).

3.2. Discussion of isotherms and compressibility graphs

In the following sections several features of the mixed PDC/PDOH Langmuir films are discussed. These are based on the compression (π–A) isotherms and the corresponding compressibilities.

The isotherm of pure PDOH serves as a reference for the interpretation of the more complex isotherms of PDC/PDOH mixtures. The PDOH isotherm shape is typical for amphiphilic diacetylenic compounds. It shows a steep compression of the monolayer with limiting area $A_L \approx 30$ Å^2, followed by monolayer collapse, typically at π between 12 and 30 mN m^{-1} (depending on temperature and subphase composition) [16]. A second compressed phase with A_L that corresponds to a trilayer structure is formed after the collapse [29]. The monolayer to trilayer transformation takes place in the plateau region where the two phases coexist.

Figures 1(a) and (b) show several features that help to elucidate the properties of the mixed PDC/PDOH films. The analysis and detailed interpretation of the π–A isotherms (figure 1(a)) and compressibility data (figure 1(b)) is corroborated by Brewster angle microscope images, as shown in figures 1(c) and 4.

Compressibility graphs (figure 1(b)) reveal subtle features of the compression isotherms that are not shown in the π–A isotherms. In the following sections several of these are described and analysed.

3.3. Pressure offset

The pressure offset is the molecular area at which non-zero surface pressure is first detected (figure 1(a), around line I). The observed pressure-offset area increases monotonically with the increase of the PDC molar fraction (figure 2). Small negative deviations from the ideal mixing line are observed for PDC mole fractions below 0.5. The presence of guanosine in the subphase does not change these values. In contrast, positive deviations appear at higher PDC content. The maximum positive deviation is around PDC/PDOH = 0.7 mole fraction both in the presence and the absence of guanosine. The largest difference due to guanosine is observed for PDC/PDOH = 0.9. This implies that base-pair association may have taken place already at the uncompressed (gas-like) stage of the monolayer.

3.4. PDOH collapse

The feature that represents the collapse of the pure PDOH monolayer can be traced in compression isotherms with increasing PDC molar fraction (figure 1(a), around line II). As expected, the molecular area of the PDOH collapse feature decreases with decreasing mole fraction of PDOH.

The 'PDOH' phase coexists with the 'PDC-enriched' phase (described below). It gradually disappears as the 'PDC-enriched' phase becomes predominant at PDC mole fractions above 40%. This result is in agreement with results described below, from BAM and AFM images (figures 5 and 6, respectively).

3.5. Limiting area

The limiting area for the LC phase was calculated as described above and is presented graphically in figure 1(c) and plotted against the PDC mole fraction in figure 3. It is found that the LC phase limiting area for films at all mixing ratios varies only slightly from 35 ± 3 Å^2/molecule (figure 1(a), around line III). The limiting area for the 'pure' PDOH

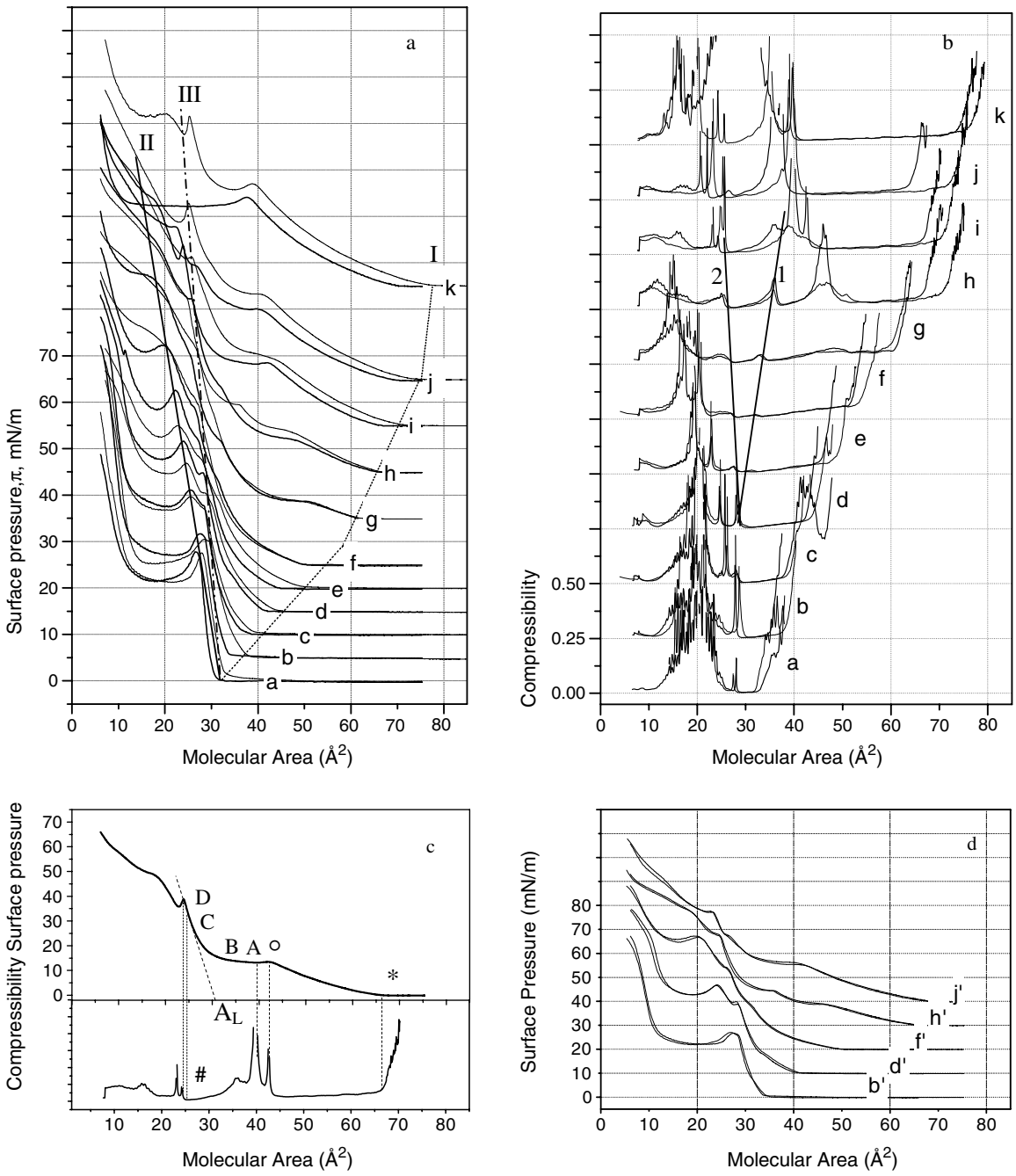

Figure 1. (a) Compression isotherms of a series of PDC/PDOH mixtures. From bottom to top, pure PDOH to pure PDC in 10% increments (a–k). Thin curve isotherms are for on 5 mM guanosine subphase, thick curves for on Trizma buffer subphase, pH = 7.5. Curves I, II, III mark transitions in the compression isotherms; see the text for details. (b) Compressibilities corresponding to the isotherms in (a). Thin lines: on 5 mM guanosine subphase; thick curves: on Trizma buffer subphase. Lines '1' and '2' mark the nucleation and collapse of the organized liquid condensed 2:1 PDC/PDOH monolayer, respectively. (c) Top panel: the π–A isotherm of 80% PDC on a Trizma base. Bottom panel: the corresponding compressibility graph. The pressure offset (∗), the onset of the liquid expanded (LE) to liquid condensed (LC) transition (○), the point of minimum compressibility (#) and a graphical representation of the determination of the limiting area (A_L) are shown; the additional vertical lines guide the eye to the main features. A–D correspond to BAM images in figure 4. (d) Compression isotherms of selected compositions on a subphase containing 5 mM of a base non-complementary to PDC (adenosine). For clarity and because of the insignificant differences between the traces, only isotherms for on adenosine and buffer are presented. Thick curve: buffer; thin curve: adenosine. The PDC content in the film is: b′—10%; d′—30%; f′—50%, h′—70%; j′—90%.

and PDC can be evaluated independently from figure 1(a): 35 Å^2/PDOH molecule (trace a) and 60 Å^2/PDC molecule (trace k). However, one needs to bear in mind that the hydroxyl head-group projection is smaller than that of the diacetylenic alkyl chain and therefore has a negligible effect on the limiting area. The film composition for which the LC phase is the most condensed is at 70% PDC, as is apparent from analysis of the limiting area, the compressibility and the maximum slope (figures 3(a)–(c)). This situation holds for films formed on both water and guanosine solution. The films that are formed

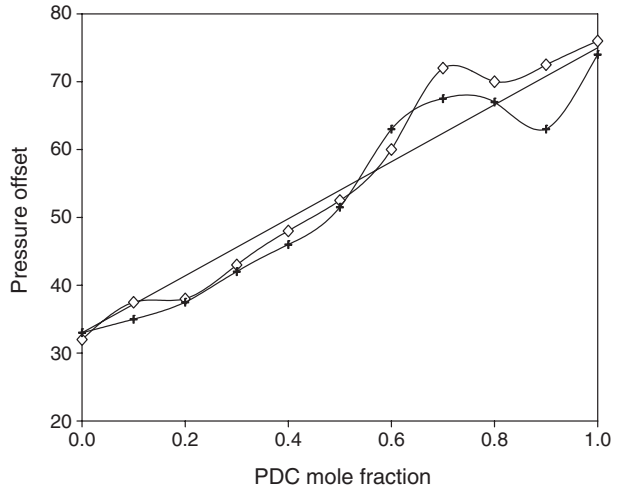

Figure 2. Pressure offset values for isotherms of mixed PDC/PDOH monolayers. The straight line is interpolated between the pressure offsets of the pure compounds. +: films on water subphase; ◇: on guanosine subphase.

on guanosine manifest better order, as judged from the smaller limiting area, lower compressibility and steeper slope.

These measurements were taken in the isotherm regions where the LC phase predominates, as is evident from the BAM images (figures 5 and 6). The extent of these regions, from nucleation to collapse, grows gradually from 40% PDC mole fraction to a maximum at 70% PDC mole fraction. These regions are indicated in figure 1(b) by the lines '1' and '2', that connect the nucleation and collapse of the LC phase, respectively.

In order to confirm that the specific interaction between the cytosine moiety on the Langmuir film interface and the guanosine in solution did indeed take place, films with 10, 30, 50, 70 and 90% PDC were compressed on 5 mM adenosine, timidyne and cytidine Trizma buffered solutions. Isotherms on non-complementary base solutions were found to be nearly identical to the isotherms in the absence of the base (figure 1(d)). Compression isotherms of films with higher than 70% PDC content on guanosine solution exhibit larger molecular area for the same surface pressure (figure 1(a)).

3.6. Brewster angle microscopy

BAM images provide structural insights into the compression isotherm data. Processes that take place on the monolayer during compression, such as domain nucleation and growth, collision, integration and collapse, are visualized (figure 4) and can be associated with their respective features on the compression isotherms (figure 1(c)). Moreover, the domain morphological features were found to distinctly differ among the various film compositions. Figure 5 shows BAM images of two series of films with incrementally lowered PDC content that are formed on subphase in the absence or presence of guanosine in the subphase.

3.7. BAM images of PDC/PDOH on buffer

Langmuir films of pure PDC and its mixtures with PDOH were imaged with BAM at the air–solution interface during

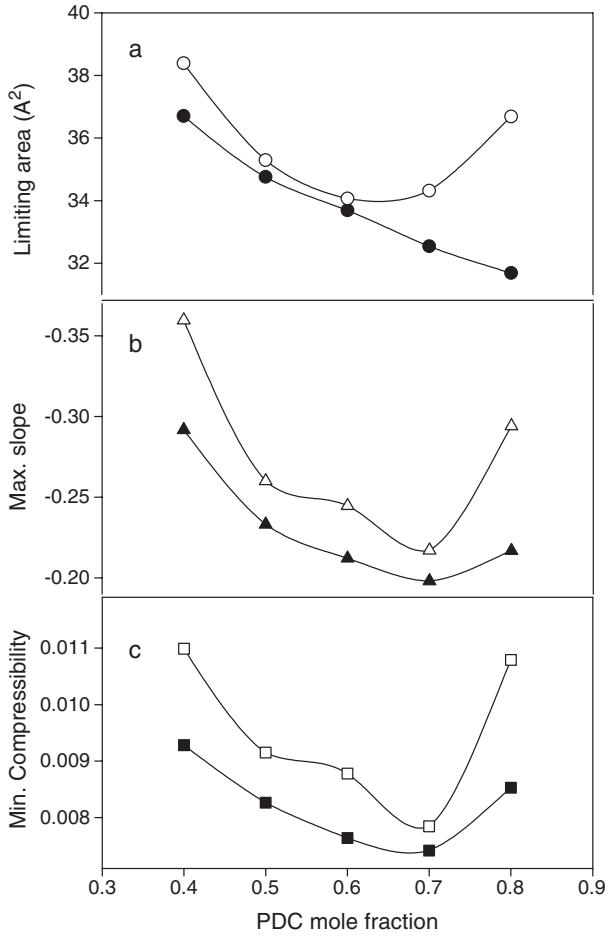

Figure 3. Dependences of the limiting area (a), maximum slope (b) and minimum compressibility (c) values on the film composition and on the presence of guanosine (open symbols) or its absence (filled symbols) in the subphase. Films with 70% PDC exhibit superior structural stability. Addition of guanosine in the subphase causes some expansion that is manifested in a higher limiting area and as a result a less steep slope and a higher compressibility. Yet, at 70% PDC the compressibility is similar to that for on pure water.

compression at $\pi \sim 20$ mN m^{-1} (figures 5(a)–(e)). The images depict the morphological evolution of the LC phase domains, as an outcome of the gradual relief of the steric disturbances in the planar packing arrangement. Figure 5(a) depicts the morphology of pure PDC domains. The domains appear spherulitic: a nucleation centre at their centre and an outwards growth direction. Dilution of PDC to 90% with PDOH (figure 5(b)) results in highly curved crescent-like domains. Further dilution to 80% reveals branched domains with two different features: primary shafts are linear, while the secondary branches are curved and reminiscent of the 90% PDC curved morphology (figures 4 and 5(c)). This dual morphology can be explained on the grounds of preferential composition of the mixed domains. The primary shafts are the first to nucleate (figure 4(a)) and as a result of its growth the surface solution becomes depleted with respect to the PDOH. Hence, further growth (secondary branches) takes place in a PDC-enriched composition, as judged from its similarity in morphology to that for 90% PDC. At lower PDC content (70%, 60% and below; figures 5(d) and (e)) the domains appear

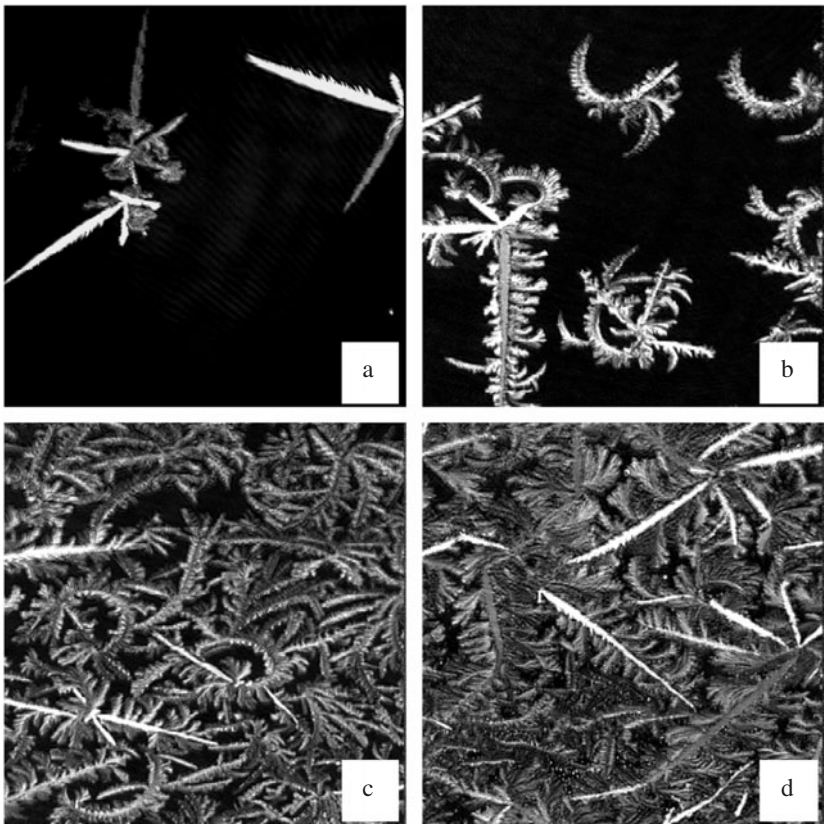

Figure 4. BAM images of 80% PDC/PDOH spreading solution in the absence of guanosine. (a)–(d) correspond to the notation in figure 1(c). Images were captured during the film's compression. (a) The film immediately after the liquid expanded to liquid condensed transition. The nascent LC domains exhibit predominantly straight morphology. (b) Further compression results in branching of the main domains' shafts. These however are curved, as opposed to the straight main branches, and reflect different PDC/PDOH ratios. (c) The monolayer near the maximum density stage, at which the compressibility is at a minimum. (d) The monolayer at the collapse point. Brighter areas indicate the formation of multilayers.

linear over hundreds of micrometres. This very long range order without apparent perturbations indicates that the domain organization is strain free. It follows that the steric disorder that originates from the size mismatch of the cytosine-bearing head-group and the DA-containing alkyl chain is completely relieved at around 70% mole fraction of PDC (about 2:1 mole ratio). The surface mixture of large cytosinyl head-groups with the small alcohol head-groups results in average head-group size that matches that of the diacetylenic alkyl chain.

3.8. BAM images of PDC/PDOH on guanosine solution

A similar series of BAM images taken during compression on 5 mM guanosine solution in Trizma buffer provide further information on the film organization and suggest that complementary base-pair binding took place (figures 5(f)–(j)). Figure 5(f) depicts the disordered spherulitic domains of pure PDC, with morphology similar to that formed in the absence of guanosine. Upon dilution to 90% with PDOH (figure 5(g)), the domains are smaller, about 25 μm in diameter, highly curved and made up of several branches that emerge from the centre. The higher domain curvature in the presence of guanosine indicates that the association between the cytosine head-groups and the complementary base formed an effective larger head-group. Figure 5(h) corroborates this assertion in that the primary shafts, which without guanosine appear straight (figure 5(c)), are slightly curved in the presence of guanosine. Further dilution to 70% reveals a new feature of extensive lateral expansion of the domains, which becomes equidimensional (figure 5(i)). This observation adds to previous indications that at a molar ratio of nearly 2:1 PDC:PDOH the film organization is optimal and it is nearly strain free.

At lower molar ratios BAM images in the presence and absence of guanosine become progressively more similar and the domains are elongated, gradually turning into the flat and featureless domains of pure PDOH.

3.9. Characterization of polymerized films transferred onto solid supports

3.9.1. AFM study of mixed PDC/PDOH films formed on water subphase. Langmuir films of PDC, PDOH and their mixtures were compressed to a surface pressure of 25 mN m^{-1}, UV polymerized on the aqueous phase and horizontally transferred to OTS-treated glass. The films were then investigated by AFM in order to gain information on their structural features at the submicrometre level (figures 6(a)–(h)). Pure PDC film on buffer shows a nanometre size cluster appearance, in which no linear motifs are observed. The nanosized domains are clustered, but do not form coherent structure. On a micrometre scale they form arc patterns (figure 6(a)).

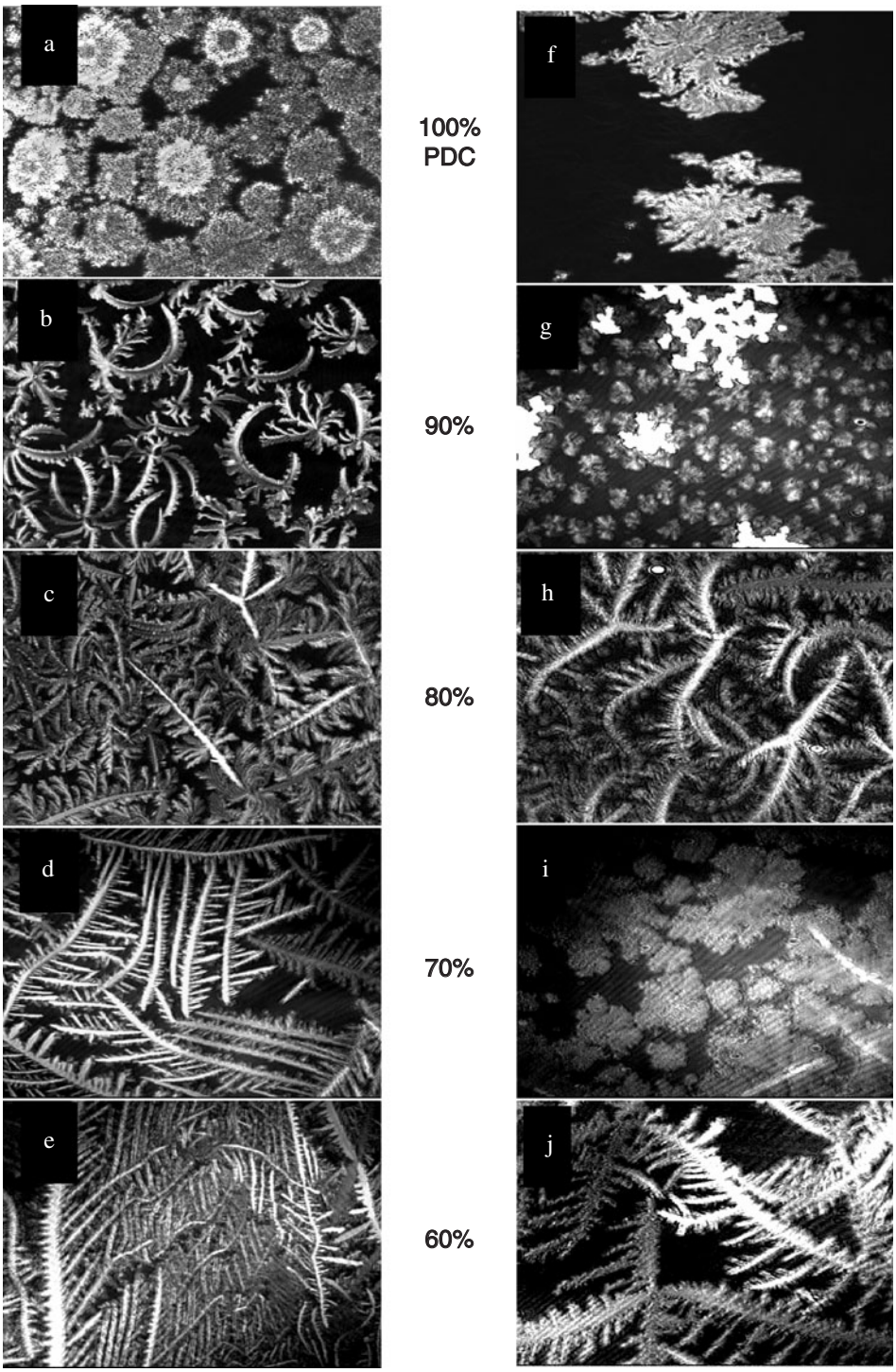

Figure 5. BAM images of PDC/PDOH mixtures on pure buffer ((a)–(e)) and on 5 mM guanosine in Trizma buffer ((f)–(j)). Film compositions: (a), (f) 100%; (b), (g) 90%; (c), (h) 80%; (d), (i) 70%; (e), (j) 60%. The scale is 450 μm on the long edge. Note the disordered morphology in (a), (f), the curved morphology in (b) and the higher curvature in (g). In (c), note the dual morphology of the main (straight) versus the curved secondary branches. In (d) note the long range of the undisturbed appearance. In (i), the domains exhibit planar rather than linear appearance in the absence of guanosine (d), suggesting enhanced lateral interactions in the presence of guanosine. In (e) and (j), the PDC content is below the optimal 2:1 ratio, the elongated morphology dominates and the effect of the guanosine is less pronounced as the cytidyl moieties are more spaced.

At 90% PDC film content, the film appears as a uniform but fragmented phase. The typical length between fractures in the direction of the polymer backbone is 0.2–0.5 μm. For comparison, undisturbed monolayers feature extended domains, tens to hundreds of micrometres without perturbations. Lower magnification AFM scans (figure 6(b), inset) reveal curved fan shape domains, in agreement with the BAM observation (figure 5(b)).

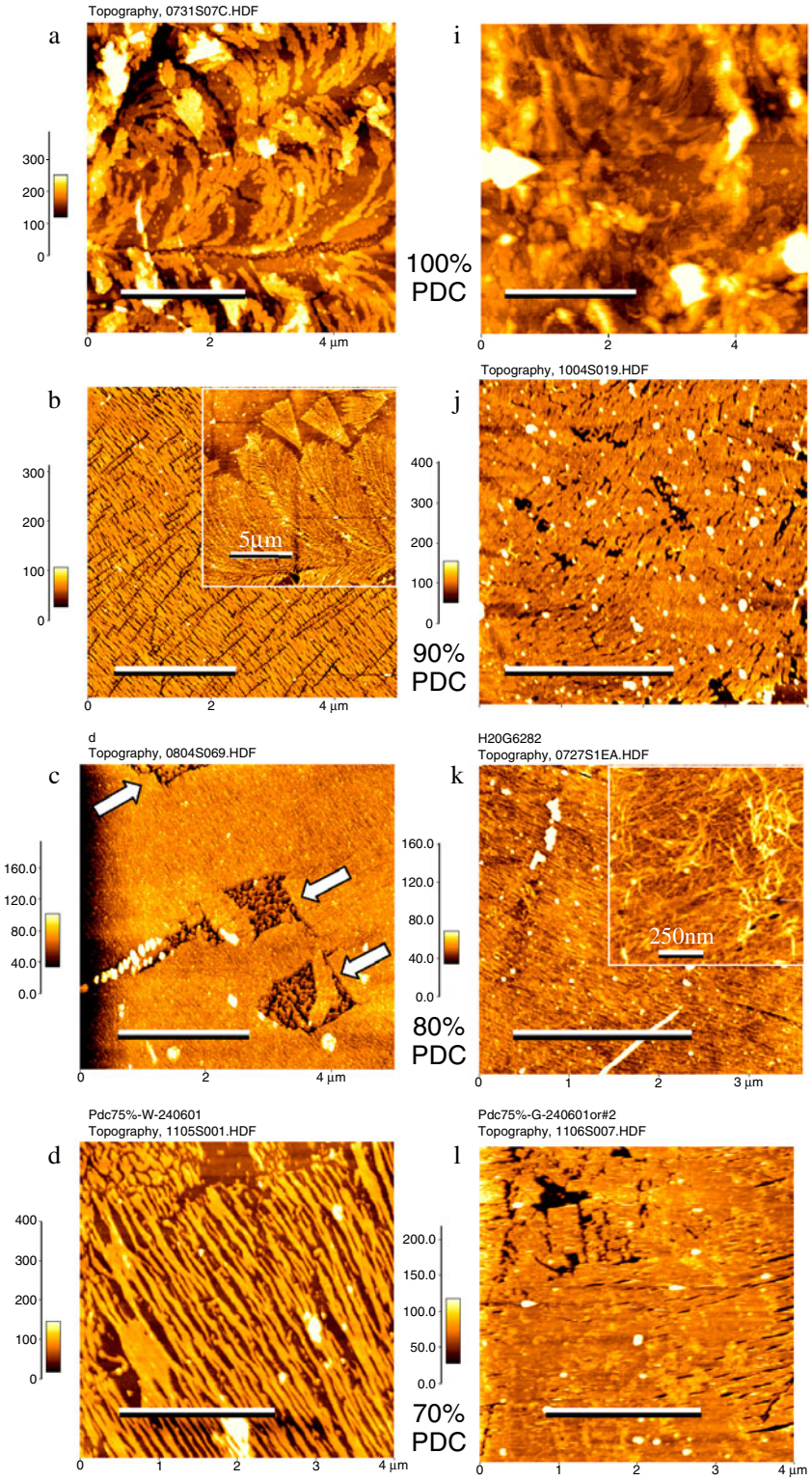

Figure 6. AFM images of the PDC/PDOH mixed film at different compositions on Trizma buffer (left, (a)–(h)) and on 5 mM guanosine buffered solution (right, (i)–(p)). The film compositions are: (a), (i) 100% PDC; (b), (j) 90%; (c), (k) 80%; (d), (l) 70%; (e), (m) 60%; (f), (n) 50% PDC; (g), (o) 20% PDC; (h), (p) pure PDOH. Note the disordered nanosized domains in (a) and (f). (b) and (g) exhibit uniform curved morphology; in (b) the film is more fractured compared with (g). Inset: a larger area view of the surface: long range curvature. (c) Extended ordered domains coexisting with limited areas of disordered material, reminiscent of (a). The film in (h) appears similar to that in (c). (d) and (j) show a uniform appearance of the extended linear domain, with near full coverage of the surface. In (j) the linearity is less apparent because of the better lateral interaction between threads. (e), (k), (f) and (l) show mixed films with the coexistence of two distinct phases. In (e), (f) the smooth domains represent PDOH-enriched phase and the striated or patchy domains the PDC/PDOH phase. In (k), (l) the PDC/PDOH phase appears similar to that in (j).

(This figure is in colour only in the electronic version)

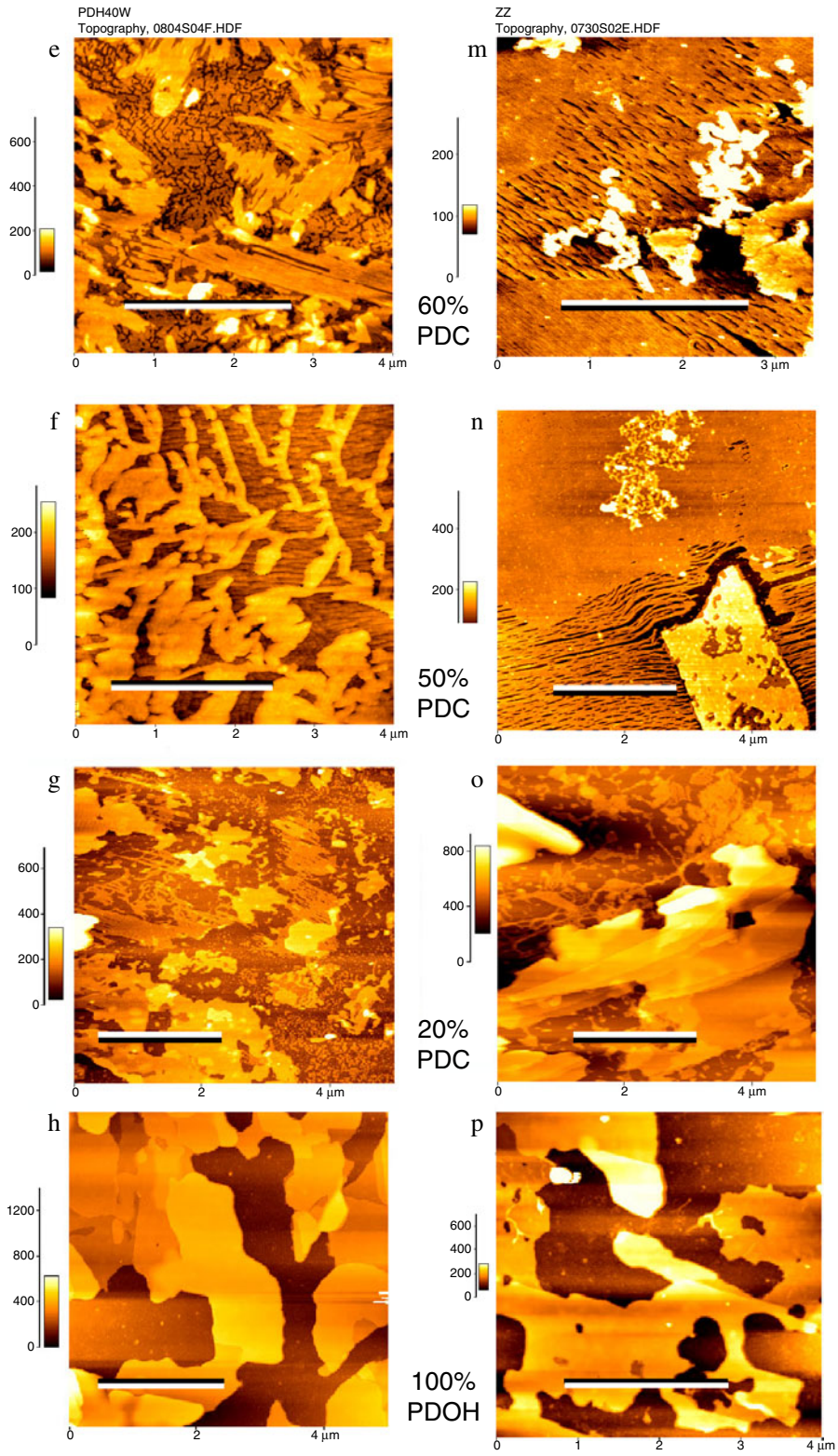

Figure 6. (Continued.)

Around 80% PDC content, the film is phase separated into a well ordered linear, striated phase with occasional disordered 'patches' roughly 50–150 nm across (figure 6(c)). The disordered phase (figure 6(c), arrows) resembles the pure PDC phase (figure 6(a)).

The imaged monolayer phases corroborate our earlier assertion that the PDC and PDOH lipids are miscible only within a narrow range of molecular ratio, namely, around 2:1 to 3:1 (67%–75%). Monolayers with this approximate composition have a distinct, long range, parallel organization

that is typical of organized thin films of polydiacetylene. At 70% PDC, the linear phase is at its maximum, totally covering the surface (figure 6(d)). Below the limits of this mixing ratio, coexistence of phases is observed: morphological features that resemble those of pure PDOH are observed alongside the ordered stripes of the mixed polymerized monolayer (figures 6(e)–(g)). At PDC content of around 50%, coexistence of PDOH-like domains and PDC-enriched domains is observed (figure 6(f)). The linear 'PDC-enriched' phase is clearly separated from the PDOH domains. In films with 20% PDC content, the typical smooth PDOH domains develop more elongated features (figure 6(g)), specific to polydiacetylene films [29], yet the majority of the surface is covered with smooth PDOH domains.

Pure PDOH domains are flat and featureless (figures 6(h), (p)), typically 1–3 μm across and vary in thickness from one to several layers. The lack of structural features within the PDOH domains supports the observation that compressed PDOH monolayers do not undergo UV photopolymerization [27]. It is likely that PDOH domains are organized in a manner that does not permit the formation of the linear yne–ene motif through topotactic polymerization. Images of pure PDOH films in the presence (figure 5(p)) and absence (figure 5(h)) of guanosine in the subphase are almost indistinguishable.

The AFM images (figures 6(a)–(h)) depict gradual development and reduction of the ordered mixed phase as the overall film composition changes. Occurrence of the PDC-enriched domains is becoming increasingly abundant as the molecular ratio approaches the 2:1 ratio.

3.9.2. AFM images of mixed PDC/PDOH films on guanosine subphase. Pure PDC films formed on guanosine solution show no long range order and are disorganized on a scale larger than a few tens of nanometres. PDC films appear more filamentary on guanosine subphase (figure 6(i)) compared to films formed on water (figure 6(a)).

At 90% PDC content the film appearance is uniform, with only one type of domain, as is the case for these films in the absence of guanosine. The overall domain shape is also curved and fan-like (figure 6(j)). The striations are wider and significantly less fractured in the polymer direction.

Films with 80% PDC content exhibit nearly uniform surface coverage. Occasionally, disordered threads emerging from the surface are observed. The thread length is several hundreds of nanometres and their diameter is around 3 nm. (Assuming a circular cross-section, the thread diameter is estimated from the AFM height profile, in order to account for tip broadening.) These threads are probably extruded from the planer film due to the association of guanosine with polymerized PDC/PDOH strands.

Films made with 70% PDC are uniform, as is the case for the same film composition in the absence of guanosine. Yet, in the presence of guanosine, the films appear less perturbed in the direction orthogonal to the polymer backbone. That is to say, lateral interactions between adjacent strands are stronger in the presence of guanosine in the subphase.

Films with less than 60% PDC that are formed on guanosine subphase do not differ significantly from those formed in its absence. In both cases the coexisting phases, mixed 2:1 PDC/PDOH and pure PDOH, are observed. The mixed phase, though, appears smooth and laterally interconnected, thus forming a flat and nearly featureless surface, as is the case for the 70% PDC films for which a uniform phase is formed. In many cases a 'woven' fabric-like pattern is observed in the 2:1 PDC:PDOH domains. This observation further indicates the formation of lateral interactions in the presence of guanosine. On the other hand, the PDOH phase is indistinguishable from the same phase formed in the absence of guanosine.

3.9.3. Visible light spectroscopy. Absorption spectra of the polymerized PDC/PDOH films in the visible range corroborate the observation obtained directly from the compression isotherms and BAM and AFM images. Two prominent absorption peaks at 490 and 540 nm correspond to the vibronic and electronic absorption bands (figure 7). The film appearance is pink to reddish. The absorption peak intensities at 530 nm and at 490 nm and the absorption peak widths at half-maximum ($HWHM_{530}$) for the different film compositions were derived from the spectra in figures 7(a) and (b) and are presented in table 1. The spectral evidence indicates that at approximately 2:1 PDC/PDOH ratio, both the absorption band (A_{540}) intensity and its width are at their respective maximum and minimum, which indicates higher film uniformity. Pure PDC films (figure 7(c)) exhibit broad absorption bands that indicate film irregularity, in agreement with the BAM (figures 5(a), (f)) and AFM (figures 6(a), (i)) observations of the disordered spherulitic growth pattern. Films that were produced in the presence of guanosine in the subphase absorb light at 4 nm longer wavelength (figures 7(c), (d)). This small, yet consistent spectral red-shift indicates that longer unperturbed conjugated segments are formed in the presence of guanosine.

4. Discussion

The results reported here indicate that mixtures of diacetylene lipids with cytosinyl and alcohol hydrophilic head-groups form a stable phase with a preferred molecular ratio of approximately 2–3 PDC molecules per PDOH molecule. This phase shows a characteristic striated appearance and differs significantly in morphological appearance from its pure components. The excess material, be it PDOH or PDC, is phase separated from the stable 2:1 phase. The spectral evidence, the compression isotherms and the evidence derived from them, the domain shape and the film surface texture, all point to the newly formed mixed film phase, with the approximately 2:1 composition, being better organized and hence more stable.

The periodicity of the polydiacetylene rigid backbone is fixed at approximately 5 Å [30–32]. The packing of neighbouring parallel polydiacetylene molecules is less stringently limited and varies between 5 and 6 Å. The nearly ideal packing of acidic polydiacetylene thin layers (10,12 pentacosadiynoic acid, for example) stems from the comparable cross-sections of the monomer heads and tails that give the molecule an overall cylindrical shape and therefore favour the formation of ordered monolayers. In PDC the cross-section of the cytosinyl head-group is larger than that of the aliphatic diacetylenic tail. Therefore, in the pure PDC film,

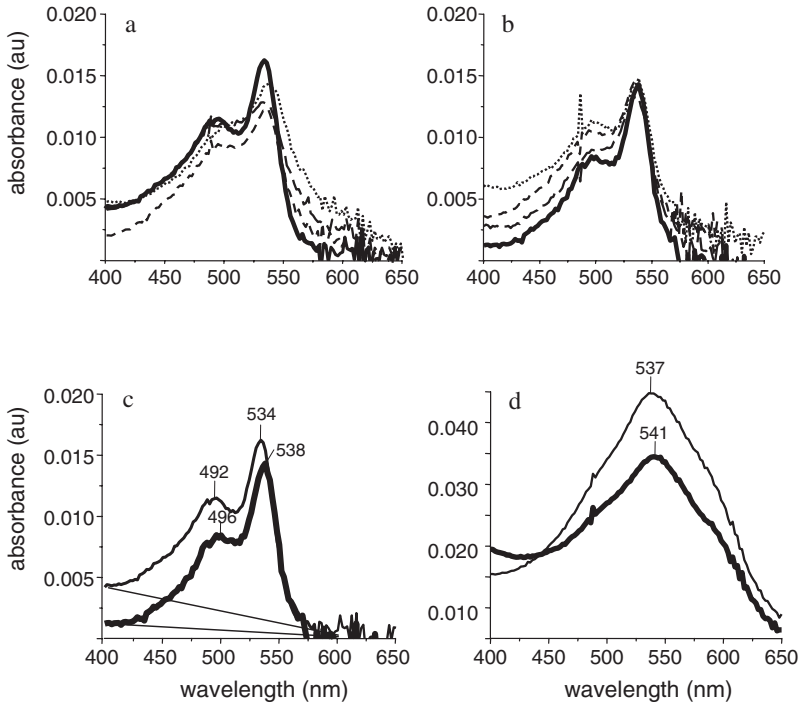

Figure 7. Visible spectra of mixed monolayer films. Films were formed on Trizma buffer (a) and on guanosine solution (b). Film compositions in (a), (b): 50% PDC (dotted curve), 70% PDC (solid curve), 80% PDC (short dashed curve) and 90% PDC (long dashed curve). Both (a) and (b) show sharper peaks and higher A(540)/A(490) ratios for PDC = 70%, indicating a higher degree of organization. The spectra are for 70% PDC (c) and 100% PDC (d) on water (thin curve) and on guanosine solution (thick curve). In (d), absorptions are broad and centred near $\lambda = 540$ nm. For all film compositions a small red-shift of $\sim$4 nm is observed when guanosine is present in the subphase ((c), (d)). The schematic illustration shows the film phase dependence on the PDC content in the spreading solution.

Table 1. Absorption spectra quantitative figures for PDC/PDOH films on water or guanosine solution. Absorptions at 490 and 540 nm were measured after background subtraction and expressed in mAU. Peak width was measured at half the peak height, in the high wavelength part of the absorption peak. Bold type: analysis of the 70% PDC spectra that indicate enhanced structural organization.

	Films on water subphase			Films on guanosine subphase		
% PDC	A(490)	A(540)	HWHM (540)	A(490)	A(540)	HWHM (540)
90	7.6	13	24	7	12.7	14
80	8.3	11	15	7.5	12	14
70	**9**	**14.5**	**13**	**8**	**15**	**14**
50	8.5	11.5	25	10	11	16

the monolayer packing is severely hindered, as is evident in the BAM and AFM images.

The formation of mixed PDC/PDOH monolayers with different molecular ratios relieves the packing strain in the monolayer. PDOH, a compound with the same aliphatic tail and a smaller head-group, is incorporated preferentially at a particular (2:1) ratio and copolymerizes with the PDC. It is not known at this stage whether the PDOH occupies a specific crystalline lattice position, or alternatively forms a random 2D solid solution. The excess PDOH at low PDC/PDOH ratios forms separate domains with the morphological character of pure PDOH. This observation indicates poor miscibility of these compounds at molecular ratios that depart from the optimal 2:1 PDC:PDOH.

At PDC content higher than the optimal ratio value, around 90% PDC, a second uniform phase with no evidence of phase separation is formed. It is distinguished from the ideal 2:1 phase in its curved 'fan'-like domains (figure 6(b), inset). The existence of this phase can also be explained by the partial miscibility of the compound used. At the 9:1 ratio the free energy of formation of the organized 2:1 phase is not achieved and 10% PDOH can be accommodated without phase separation. The outcome is the formation of an unfavourable, highly fragmented strained phase of bent diacetylene backbones (figures 6(b), (h)). The disturbed state of the film is also manifested in its broader visible absorbance spectrum. Yet this phase is better ordered than the pure PDC film, according to the visible absorbance spectrum and the other characterization methods that were applied.

On the basis of the AFM images of the series of PDC/PDOH films on water and on guanosine solution and supported by the BAM images, we constructed a phase diagram showing the surface phase dependence on the spreading solution composition (figure 8). The central part corresponds

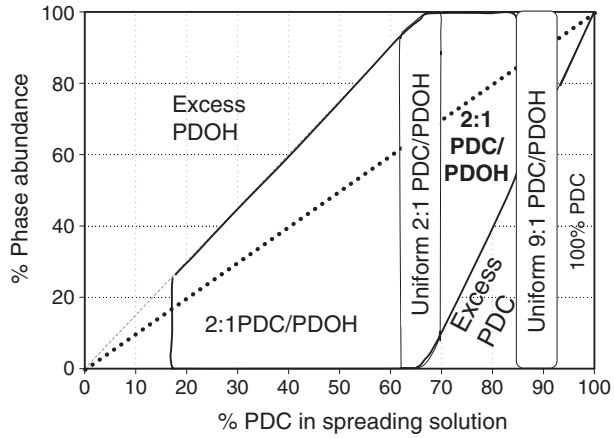

Figure 8. A reconstructed diagram of the surface phases of PDC/PDOH. The vertical direction is the approximate abundance of the different coexisting phases, according to their estimated relative areas. The boundaries between phases are drawn according to the 2:1 PDC/PDOH composition model. The diagonal dotted line is the expected composition of the film for ideally miscible components. The scheme shows the principal 2:1 PDC/PDOH phase increase in abundance until a maximum of around 70% PDC is reached. This phase coexists with the PDOH-enriched phase at lower PDC content and excess PDC at around 80% PDC. At 90% a uniform phase is formed which gradually transforms to 100% PDC.

to the mixed PDC/PDOH phase with ratio of 2 PDC per PDOH. At PDC content below 40%, the surface is dominated by the PDOH-enriched phase. When the PDC content exceeds 75%, the mixed phase coexists with the PDC-enriched phase. At 90% PDC a distorted yet uniform phase is prevalent.

Assessment of the overall effect of guanosine, present in the subphase during film preparation, can be readily carried out by examination of the AFM images. A marked difference between the appearances of films in the presence and absence of guanosine is evident. It appears that within the stable 2:1 phase, the effect of guanosine is to enhance the coherent structure of the film in the direction orthogonal to the polymer conjugated backbone. In contrast to the fibrillar appearance of the films in the absence of guanosine, in its presence long range continuity both along and across the polyconjugated direction is observed. While the large coherence length along the polymer direction is obvious, the continuity between adjacent parallel polymer molecules originates from the ordered two-dimensional organization, as discussed in the next section.

At 80% PDC content, the molecular ratio is above the optimal 2:1. AFM images of films that are formed in the presence of guanosine in solution indicate a phenomenon only observed at this composition (figure 6(i), inset). It is noteworthy that 'threads' are formed only in the presence of guanosine. This suggests that excess PDC is extracted from the film and associated with its complementary base to form rigid structures. This assumption conforms with the large persistence length of native dsDNA, where base-pair stacking is responsible for the DNA structural rigidity [33]. AFM trace analyses of these structures indicate that their height is about 3 nm. It is plausible that these assemblies are elongated micelles with one or more conjugated polymer molecules as the central backbone and stacked bases at the periphery.

4.1. Structural considerations

The limiting area for the compressed phase of 2:1 PDC/PDOH is 35 $Å^2$/molecule. Taking into account the yne–ene covalent bond length of 5 Å, the average distance between neighbouring polymer molecules is 7 Å (assuming a rectangular unit cell). This implies that within the 2:1 PDC/PDOH phase the area occupied by a single cytosinyl moiety is $35/0.67 = 52$ $Å^2$/PDC. Within this area, approximately 50 $Å^2$, a single base-pair is formed. The stacking periodicity of nucleotide base-pairs is 3.5 Å which corresponds to the van der Waals distance between aromatic compounds. The combined length of a nucleotide base-pair is approximately 11 Å, without the nucleoside sugar moieties [34]. This distance is greater than the spacing available between the neighbouring polymer chains. Accordingly, the projected area of a base-pair is nearly $3.5 \times 11 \approx 40$ $Å^2$. The long dimension of the base-pair is longer than the distance between the backbones and the stacking distance is shorter than the periodicity along it. Hence, a plausible organization is such that base-pairs are aligned diagonally with respect to the backbone direction. In this manner, base-pairs tethered on different backbones may be partially overlapping, thus enhancing the lateral interaction in the film. Alternatively, base-pairs can be inclined in the solution direction, thus projecting smaller areas onto the interface.

This analysis is based on the premises that Watson–Crick or another less common base-pairing type is indeed formed. The ability of forming biomimetic base-pairing via organized arrays of hydrogen bonds on surfaces is instrumental to the formation of hybrid surfaces of a new type and 'smart', responsive materials. The combination of natural oligonucleotide segments, that undergo interactions with surfaces that bear complementary moieties at approximately the native periodicity, may give rise to significant conformational shifts, which in turn will apply a moderate molecular-level twist on the polymer backbone. In the case of polydiacetylene backbone, such a twist is anticipated to result in electronic restructuring that can be revealed spectrally or by a direct electronic response.

It is assumed that the observed modest spectral shift as a result of the film's interaction with the complementary base is due to only monomers being used. Had short oligomers been used, the spectral response might be expected to be clearer due to cumulative synergy between neighbouring binding events, which are predicted to add and contribute to the film response.

Acknowledgments

AB thanks the Institute for Applied Biosciences, BGU and the Israel Ministry of Science for initial funding of this project. The authors thank S Geresh and J-P Lelouch for assistance in organic synthesis procedures.

References

[1] Berti D, Luisi P L and Baglioni P 2000 *Colloids Surf.* A **167** 95–103
[2] Shimada S, Masaki A, Hayamizu K, Matsuda H, Okada S and Nakanishi H 1997 *Chem. Commun.* 1421–2
[3] Marchi-Artzner V, Lehn J M and Kunitake T 1998 *Langmuir* **14** 6470–8

[4] Marchi-Artzner V, Artzner F, Karthaus O, Shimomura M, Ariga K, Kunitake T and Lehn J M 1998 *Langmuir* **14** 5164–71
[5] Weck M, Fink R and Ringsdorf H 1997 *Langmuir* **13** 3515–22
[6] Li C, Huang J G and Liang Y Q 2000 *Langmuir* **16** 7701–7
[7] Bashir R 2001 *Superlatt. Microstruct.* **29** 1–16
[8] Winfree E, Liu F, Wenzler L A and Seeman N C 1998 *Nature* **394** 539–44
[9] Seeman N C 2003 *Nature* **421** 427–31
[10] Shimomura M, Nakamura F, Ijiro K, Taketsuna H, Tanaka M, Nakamura H and Hasebe K 1996 *Thin Solid Films* **285** 691–3
[11] Radler U, Heiz C, Luisi P and Tampe R 1998 *Langmuir* **14** 6620–4
[12] Alivisatos A P, Johnsson K P, Peng X G, Wilson T E, Loweth C J, Bruchez M P and Schultz P G 1996 *Nature* **382** 609–11
[13] Elghanian R, Storhoff J J, Mucic R C, Letsinger R L and Mirkin C A 1997 *Science* **277** 1078–81
[14] Braun E, Eichen Y, Sivan U and Ben-Yoseph G 1998 *Nature* **391** 775–8
[15] Lieser G, Tieke B and Wegner G 1980 *Thin Solid Films* **68** 77–90
[16] Tieke B and Lieser G 1982 *J. Colloid Interface Sci.* **88** 471–86
[17] Kuriyama K, Kikuchi H and Kajiyama T 1996 *Langmuir* **12** 6468–72
[18] Kuriyama K, Kikuchi H and Kajiyama T 1998 *Langmuir* **14** 1130–8
[19] Fisher N E 1994 *J. Phys.: Condens. Matter* **6** 2047–58
[20] Huo Q, Russell K C and Leblanc R M 1999 *Langmuir* **15** 3972–80
[21] Kaneko F, Shibata M and Kobayashi S 1992 *Thin Solid Films* **210** 548–50
[22] Cheng Q and Stevens R C 1998 *Langmuir* **14** 1974–6
[23] Carpick R W, Sasaki D Y and Burns A R 2000 *Langmuir* **16** 1270–8
[24] Charych D, Cheng Q, Reichert A, Kuziemko G, Stroh M, Nagy J O, Spevak W and Stevens R C 1996 *Chem. Biol.* **3** 113–20
[25] Charych D H, Nagy J O, Spevak W and Bednarski M D 1993 *Science* **261** 585–8
[26] Jonas U, Shah K, Norvez S and Charych D H 1999 *J. Am. Chem. Soc.* **121** 4580–8
[27] Spevak W R 1993 *The Presentation of Biological Ligands on the Surface of Polymerized Monolayers and Liposomes* (Berkeley, CA: University of California Press) p 199
[28] Mullah K B and Bentrude W G 1991 *J. Organ. Chem.* **56** 7218–24
[29] Sasaki D Y, Carpick R W and Burns A R 2000 *J. Colloid Interface Sci.* **229** 490–6
[30] Kuriyama K, Kikuchi H and Kajiyama T 1998 *Langmuir* **14** 1130–8
[31] Lieser G, Tieke B and Wegner G 1980 *Thin Solid Films* **68** 77–90
[32] Tieke B and Lieser G 1982 *J. Colloid Interface Sci.* **88** 471–86
[33] Rivetti C, Guthold M and Bustamante C 1996 *J. Mol. Biol.* **264** 919–32
[34] Cantor C R and Schimmel P R 1980 *Biophysical Chemistry. Part 1: The Conformation of Biological* (New York: Freeman)

CRYSTAL GROWTH & DESIGN
XXXX
VOL. 0, NO. 0
1−5

Nanocrystalline Ag_2S on Polydiacetylene Langmuir Films

Nataly Belman,[†,#] Yuval Golan,*[,†,#] and Amir Berman*[,‡,#]

Department of Materials Engineering, Department of Biotechnology Engineering and the Ilse Katz Center of Nanotechnology, Ben-Gurion University of the Negev, Beer-Sheva 84105, Israel

Received July 19, 2004; Revised Manuscript Received August 25, 2004

ABSTRACT: Silver sulfide (Ag_2S) nanocrystals were prepared in ambient conditions by exposing crystalline polydiacetylene (PDA) Langmuir films at the air−$AgNO_3$ solution interface to H_2S gas. The deposited nanocrystals were studied by atomic force microscopy (AFM), transmission electron microscopy (TEM), high-resolution TEM (HRTEM), fast Fourier transform (FFT) analysis of HRTEM images, ultrahigh-resolution scanning electron microscopy (UHR-SEM), and X-ray powder diffraction (XRD). PDA Langmuir films played a dominant role in controlling the size and lateral arrangement of the chemically deposited Ag_2S nanocrystals. Two distinct nanocrystal populations were obtained: small nanocrystals of ca. 8 nm in diameter arranged along the strands on the PDA film, and larger Ag_2S nanocrystals of ca. 50 nm were formed in the voids between the PDA domains. The concentration of the Ag^+ ions in the subphase controlled the nanocrystal film morphology and surface coverage. The linearly arranged nanocrystals were not crystallographically oriented with respect to the PDA film template, as opposed to PbS and CdS (divalent metal ion sulfides) that were previously shown to be oriented along the conjugated direction of the PDA film.

Introduction

Polydiacetylene (PDA) is an anisotropic, robust conjugated polymer that changes its color from blue to red upon thermal, mechanical, or chemical stimulation.[1−4] PDA is an intrinsically semiconducting conjugated material. Its conductivity increases when excess electrons or holes are supplied to the π-electron backbone system.[1,3]

The 2D crystal structure of PDA Langmuir films was determined using electron diffraction (ED) in the transmission electron microscope (TEM),[4,5] atomic force microscopy (AFM), Fourier transform infrared spectroscopy (FTIR),[6] and grazing incidence X-ray diffraction (GIXD).[7] PDA Langmuir film is formed by compression of the amphiphilic long-chain diacetylene monomers, 10,12-pentacosadiynoic acid (PCDA) $CH_3(CH_2)_{11}C{\equiv}C-C{\equiv}C(CH_2)_8COOH$, in the Langmuir trough on water subphase. During compression, the film undergoes a monolayer-to-trilayer transition, which can be followed in the resulting pressure−area per molecule ($\pi-A$) isotherm.[8−11] Notably, the PCDA monolayer on pure water is unstable and cannot be easily polymerized.[11] UV irradiation of the compressed trilayer results in a polymerized PDA layer.[10,11] Each 20−40 linear polymer chains are organized in parallel strands 10−30 nm wide. These strands, in turn, are organized in parallel and form 2D crystalline domains that are randomly oriented in-plane.[11,12] The length of the strands can reach several micrometers and span the entire size of a crystalline domain.

Silver sulfide (Ag_2S) is a good prospective photoelectric and thermoelectric material. Ag_2S has three common forms. α-Ag_2S is the ambient-temperature monoclinic phase (C_{2h}^5 ($P2_1/n$)). At 177 °C, α-Ag_2S transforms to a β-Ag_2S body-centered cubic (BCC) structure and at 592 °C the BCC phase transforms to a face-centered cubic (FCC) γ-Ag_2S phase.[13−16] Monoclinic α-Ag_2S is a semiconductor with a direct band gap of $E_g \approx 1$ eV at room temperature[15−18] and relatively high absorption coefficient (about 10^4 cm^{-1}). It has a wide variety of potential applications, such as infrared detectors and photosensitive films in optoelectronic devices, thermopower cells, and solar-selective coatings.[17] Nanocrystalline Ag_2S thin films are of special importance to solar, photographic, and near-IR photon-detection devices.[15]

Various methods for the deposition of nanocrystalline α-Ag_2S were applied.[15−26] Hydrothermal and solvothermal methods were demonstrated for the synthesis and assembly of α-Ag_2S nanorod and nanoparticle arrays. Alkanethiol was used as a template by reacting silver thiolate micellar solution with Na_2S.[19] α-Ag_2S nanocrystals were formed by the conversion of silver thiolate polymers using sodium sulfide.[15] α-Ag_2S nanoparticles were prepared in Nylon 11 films by exposing an evaporated film of Ag on Nylon 11 to a mixture of H_2S/O_2 mixed gases.[24] Nanospherical α-Ag_2S/poly(vinyl alcohol) (PVA) composites were prepared by sonochemical irradiation of an ethylenediamine-water solution of elemental sulfur and silver nitrate acetate in the presence of PVA.[25] Poly(vinylpyrrolidone) (PVP)-Ag_2S nanocomposites were prepared through in-situ reaction of PVP/$AgNO_3$ with CS_2 as the sulfur source in ethanol at room temperature.[26]

PDA has been previously used as a substrate for crystal growth at the air−solution interface. Oriented growth of calcite, nano-CdS, and nano-PbS on PDA have been previously reported. Calcite crystals that were formed on the PDA film were uniform in orientation.[10,27]

* To whom correspondence should be addressed. A.B. Phone: 972-8-6472400. Fax: 972-8-6472983. E-mail: aberman@bgumail.bgu.ac.il. Y.G.: Phone: 972-8-6461474. Fax: 972-8-6472944. E-mail: ygolan@bgumail.bgu.ac.il.
† Department of Materials Engineering.
‡ Department of Biotechnology Engineering.
# Ilse Katz Center of Nanotechnology.

10.1021/cg049752l CCC: $27.50
Published on Web 00/00/0000

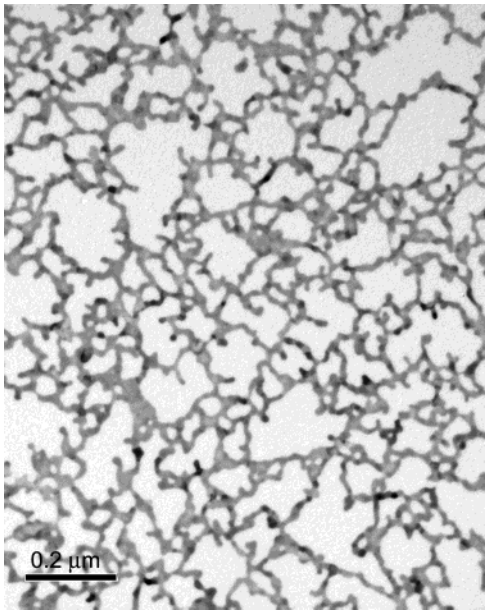

Figure 1. BF TEM image of Ag_2S crystals generated at the air−water interface by exposing 1 mM $AgNO_3$ solution (in the absence of PDA) to H_2S.

TEM observation showed that CdS nanocrystals precipitated along the PDA linear strands, producing unidirectional assemblies of semiconducting material. The corresponding ED spot pattern showed four zone axes of coexisting orientations, which sowed a common 220 diffraction pair that was aligned in the direction of the PDA linear backbone.[10,28] AFM and TEM studies on the chemical deposition of PbS nanocrystals on PDA Langmuir films showed that the $PbCl_2$ subphase concentration controlled the surface coverage of the nanocrystal films. TEM and ED indicated that the nanocrystals were aligned with the linear PDA film (as observed for CdS on PDA), with a uniaxial orientation relationship in which the $\langle 110 \rangle_{PbS}$ direction was parallel to the linear direction of the polymer substrate. Three distinct, coexisting orientations were observed with typical nanocrystal morphologies corresponding to each orientation.[12,29]

While all previous studies of nanocrystal deposition on PDA employed divalent metal ions (Cd^{2+}, Pb^{2+}, Ca^{2+}) in the subphase, in the present work we have used for the first time monovalent Ag^+ ions as the metal ion source. Conventional TEM imaging, high-resolution TEM (HRTEM), fast Fourier transform (FFT) analysis of HRTEM images, ultrahigh-resolution scanning electron microscopy (UHR-SEM), AFM and X-ray diffraction (XRD) analyses were carried out to investigate the morphology of the Ag_2S nanocrystals and their relationship with the PDA substrate.

Experimental Procedures

Materials. 10,12 Pentacosadiynoic acid ($CH_3(CH_2)_{11}C{\equiv}C-C{\equiv}C(CH_2)_8COOH$; PCDA) ≥97% HPLC (Fluka), chloroform stabilized with Amylene (HPLC, Bio Lab Ltd. Israel), $AgNO_3$ 99.998% (Aldrich), octadecyltrichlorosilane (OTS) 90+% (Aldrich), cyclohexane 99.5% (Aldrich), and 0.5% H_2S in N_2 (Maxima, Israel) were used without further purification. Distilled water (18.2 MΩ cm) was obtained using a Millipore filter system.

Langmuir Film Preparation. A Nima (Coventry, UK) Langmuir trough (model 611) was filled with distilled water. 2 mM PCDA in chloroform was carefully spread onto the water surface and held for 15 min at zero pressure prior to compression to allow for solvent evaporation. Compression was done at a rate of 10 cm^2/min until a surface pressure of 25 mN/m was reached. During compression, the film undergoes an ordered monolayer-to-trilayer transition. Finally, UV irradiation of the films was performed with a hand-held UV lamp (λ = 254 nm at a distance of 15 cm), resulting in a polymerized "blue phase" PDA layer.[10,11]

Ag_2S Deposition. After PDA deposition and polymerization, the water subphase was replaced with ca. three trough volumes (3 × 170 mL) of the $AgNO_3$ aqueous solution using a two-channel peristaltic pump, keeping a constant water level. Injection of H_2S gas into the airtight enclosure over the PDA film lead to the deposition of nanocrystalline Ag_2S at the air−solution interface.

Sample Characterization. For TEM and UHR−SEM characterization, the PDA/Ag_2S and Ag_2S nanocrystals that were grown in the absence of PDA were transferred onto a holey carbon-coated, 300 mesh copper grid (SPI supplies #3630C, West Chester, PA) by simply lowering the grids under the air−solution interface and lifting them together with the film of interest using sharp tweezers. The samples were then blotted with filter paper and dried at 40 °C.

TEM analysis was carried out using a JEOL 2010 Fas-TEM or Philips Tecnai G^2 microscopes operating at 200 and 120 keV, respectively.

UHR-SEM was used to study the morphology of films. Samples were examined uncoated in a JEOL JSM 7400F UHR-SEM.

For AFM characterization the PDA/Ag_2S film was transferred onto a glass slides using the Langmuir-Schäffer method. Prior to transfer, the glass slides were hydrophobized by self-assembly of an OTS monolayer. This was carried out by immersing the slides in a solution of 300 μL of OTS in 100 mL of cyclohexane for 8 h. AFM measurements were performed at ambient conditions using a Digital Instruments Dimension 3100 mounted on an active antivibration table. The 512 × 512

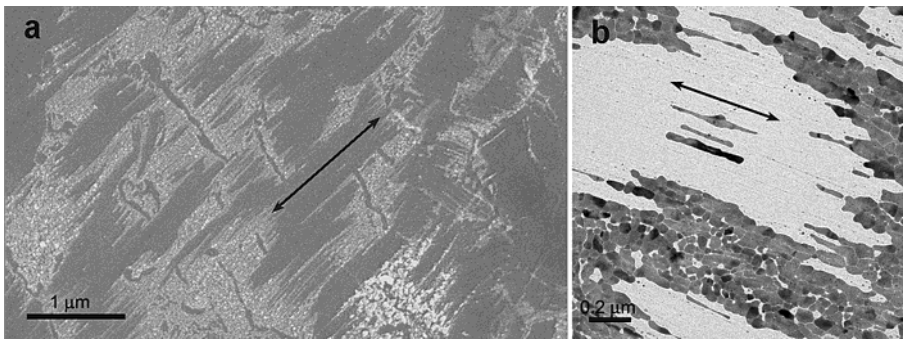

Figure 2. (a) SE UHR-SEM image of Ag_2S nanocrystals on PDA. (b) BF TEM image of Ag_2S nanocrystals on PDA. The PDA backbone direction is shown by arrows. The Ag_2S nanocrystals were deposited in the presence of PDA Langmuir film from an aqueous subphase of 1 mM $AgNO_3$.

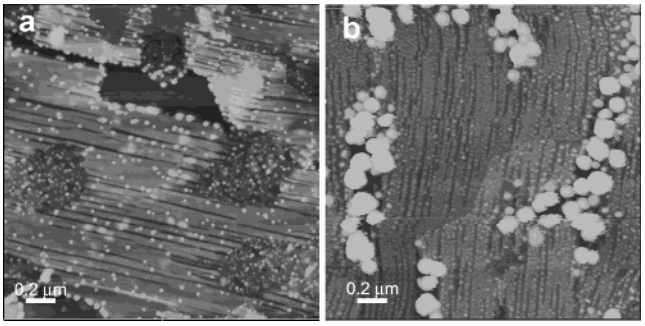

Figure 3. AFM images of Ag_2S nanocrystals on PDA. The Ag_2S nanocrystals were deposited in the presence of PDA Langmuir film from an aqueous subphase of (a) 0.03 mM, (b) 0.3 mM $AgNO_3$.

pixel images were taken in tapping mode with a scan size of 2 μm using a 100 μm scanner at a scan rate of 1 Hz.

X-ray powder data were collected in transmission geometry with a Huber G670 Image Foil Guinier Camera using $CuK\alpha_1$ radiation (wavelength of 1.54056 Å) emitted by a rotating anode source operating at 40 kV and 100 mA.

Results

In a control experiment, Ag_2S was deposited at the air−water interface in the absence of PDA by directly exposing an aqueous solution of 1 mM $AgNO_3$ to H_2S gas. As shown in the bright field (BF) TEM image in Figure 1, the nanocrystals are randomly distributed on the surface, forming a partial film of interconnected particles that are about 20−100 nm in size. The corresponding ED pattern (not shown) verified, as expected, that the crystals were randomly oriented on the solution subphase and matched the monoclinic α-Ag_2S structure (JCPDS powder diffraction file #14−0072). This preparation was used as a reference sample for similarly deposited Ag_2S in the presence of PDA.

Ag_2S deposited in the presence of a PDA Langmuir film resulted in the formation of discrete crystalline nanocrystals. A secondary electron (SE) UHR-SEM image of Ag_2S nanocrystals (prepared from a subphase concentration of 1 mM $AgNO_3$) on PDA is shown on Figure 2a. The striped dark areas are the PDA domains with nanosized Ag_2S material, while the bright areas are Ag_2S crystals deposited in voids between PDA domains or in defects within the domains. It can be seen that the nanocrystal film morphology follows the linear morphology of the polymer. A BF TEM image of the same Ag_2S particulate film is shown in Figure 2b. It demonstrates that the PDA is covered with small Ag_2S nanocrystals that are arranged along the PDA backbone direction with sizes ranging 4−12 nm. Larger Ag_2S nanocrystals appeared in the voids of the PDA domains forming elongated, needle-shaped deposits that are aligned with the linear PDA backbone direction (arrows in Figure 2a,b). The width of the deposits was in the range 15−60 nm.

AFM images of Ag_2S particulate films generated by the exposure of a PDA Langmuir film to H_2S gas on aqueous solutions of 0.03 and 0.3 mM $AgNO_3$ are shown in Figure 3, panels a and b, respectively. At low solution concentrations only a few nanocrystals that were randomly arranged along the PDA strands were observed. Higher nanocrystal coverage in the PDA voids compared to the coverage on the surface of the PDA domains is evident. In the higher solution concentration the PDA domains were covered with linearly arranged nanocrystals, following the PDA linear pattern. In the PDA voids and defects regions, larger Ag_2S crystals were observed, as was also demonstrated by UHR-SEM and TEM. The AFM-measured height of the nanocrystals arranged on PDA film template was 5−10 nm and 40−110 nm for the larger nanocrystals in the PDA voids.

Linearly arranged Ag_2S nanocrystals (Figure 4a) that were deposited on PDA from a 0.3 mM $AgNO_3$ solution were analyzed using HRTEM. To determine the nanocrystals orientation with respect to the PDA, FFT analyses of a large number of individual particles HRTEM images were performed. Figure 4b depicts one such image and FFT (insets). The insets show FFT analysis from different areas of the crystal (black frames) that indicate the crystal orientation. It can be clearly seen that the nanocrystal consists of several crystalline grains and is not a single crystal. Each FFT pattern is different, indicating that each nanocrystal is differently oriented. A HRTEM image of Ag_2S nanocrystal deposited on PDA from a 0.03 mM $AgNO_3$ solution is shown on Figure 4c. A typical nanocrystal consists of a number of small grains with dimensions of 3−4 nm. Notably, there is no orientation relationship between these grains.

The crystalline phase was unequivocally identified by

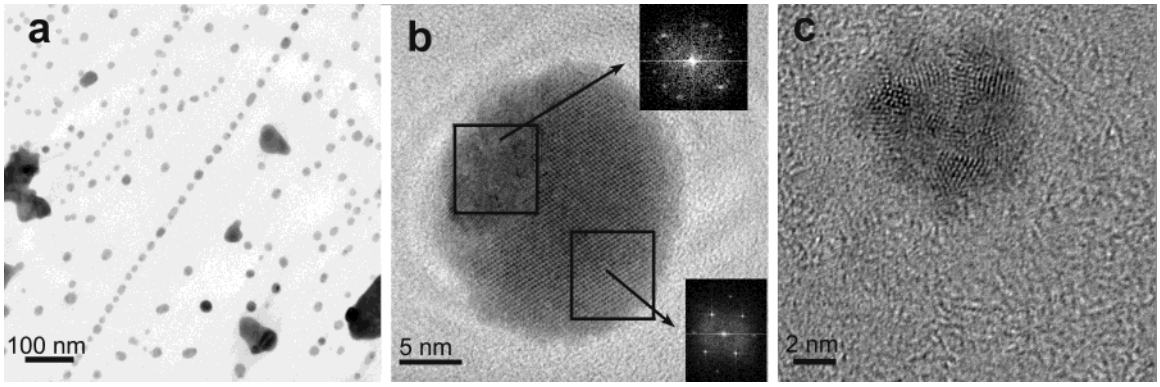

Figure 4. (a) BF TEM image showing Ag_2S nanocrystals linearly arranged on PDA. (b) HRTEM image of one polycrystalline nanoparticle. The insets show FFT analyses obtained from corresponding areas in the crystal (outlined). Images (a) and (b) show Ag_2S nanocrystals that were deposited on PDA from a 0.3 mM $AgNO_3$ solution. (c) HRTEM image of Ag_2S polycrystalline nanoparticle deposited on PDA from a 0.03 mM $AgNO_3$ solution.

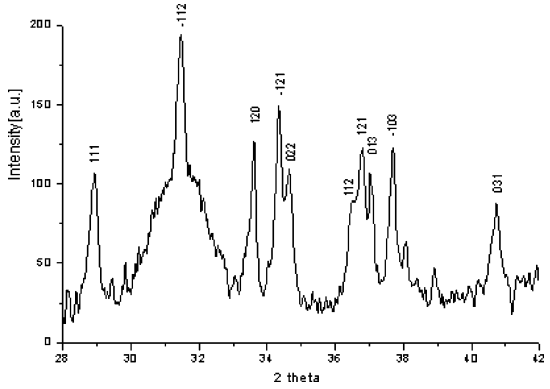

Figure 5. X-ray diffraction spectrum of Ag_2S nanocrystals on PDA. The Ag_2S nanocrystals were deposited from a subphase concentration of 1 mM $AgNO_3$ solution.

XRD as monoclinic α-Ag_2S. An XRD spectrum of Ag_2S nanocrystals on PDA is shown in Figure 5. The Ag_2S nanocrystals were deposited from a subphase concentration of 1 mM $AgNO_3$ solution. Two nanocrystal populations can be identified from profile analysis of the strong ($\bar{1}12$) peak shape, as well as from other lower intensity peaks. The tall narrow peaks correspond to the population of large crystals and the broader peaks from the population of the smaller crystals (in agreement with Figures 2 and 3). The crystal coherence length p of the small crystals was estimated from the width of the ($\bar{1}12$) and of the large crystals was averaged from (111), (120), ($\bar{1}03$), and (031) diffraction peaks using the Schërrer formula:

$$p \approx K_W \frac{\lambda_0}{\Delta 2\theta \cos \theta}$$

where λ_0 is the wavelength (1.540560 Å), θ is the position of the (hkl) diffraction peak, and $\Delta 2\theta$ is the full width at half-maximum (fwhm) of the same diffraction peak in radians. $K_w = 0.9$ is the shape factor used for roughly spherical crystal geometries.[30] For the diffraction spectrum shown in Figure 5, the results of the Schërrer analysis yielded coherence lengths of $p = 20-40$ nm and 4−5 nm for big and small crystals, respectively, which is in good agreement with the values we observed by TEM.

Discussion

The Ag_2S nanocrystals grown under PDA Langmuir film templates are significantly different from Ag_2S crystals formed at the air−solution interface in the absence of PDA. In the presence of PDA, two crystal populations were obtained: small, ca. 8 nm nanocrystals arranged along the PDA strands and larger Ag_2S crystals of ca. 50 nm in the voids of the PDA. In the absence of PDA, the deposited Ag_2S crystals are roughly 50 nm, as is the case for the deposited material in the PDA voids. The morphology and size of the deposited crystals in the absence of PDA is reminiscent of very recently reported chemically deposited Ag_2Se nanocrystals.[31] The presence of a PDA Langmuir film at the air−solution interface has been shown to play an imperative role in ordering Ag_2S nanocrystals into linear arrays along the polymer strands. The effect of subphase concentration on the nanocrystals surface coverage and film morphology was studied by AFM investigation. In low $AgNO_3$ concentrations, low surface coverage and irregular arrangement of the nanocrystals on PDA was obtained (Figure 3a). In the PDA voids, the deposited material is of similar size distribution as that in absence of the PDA substrate. At higher $AgNO_3$ concentrations (0.3 and 1.0 mM), higher coverage of the surface was obtained, with the nanoparticles organized in linear rows that follow the linear direction of the polymer (see Figure 3b). In the PDA voids, the deposited nanocrystals are of the same size and morphology as of those obtained in the absence of PDA (Figure 1).

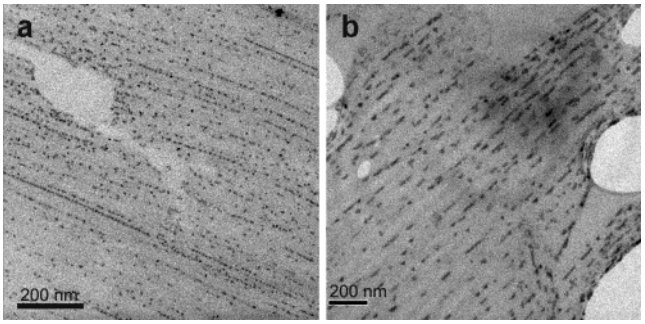

Figure 6. TEM BF images of (a) CdS and (b) PbS nanocrystals on PDA (reprinted with permission from ref 29. Copyright 2003 American Chemical Society).

The nanocrystal orientation on the PDA could not be determined directly using ED in the TEM due to the weak diffraction signal. FFT analysis of the HRTEM images (Figure 5) showed that the linearly arranged nanocrystals did not have a specific orientation with respect to the PDA film template. This observation is very different from that obtained from divalent metal sulfides on PDA (CdS, PbS) that showed a well-defined uniaxial alignment along the linear direction of the polymer.[10,12,28,29]

In our previous studies, CdS[10,28] and PbS[12,29] nanocrystals were prepared by exposing PDA Langmuir films to H_2S gas at the air−solution interface ($CdCl_2$ and $PbCl_2$ aqueous solutions). The CdS (Figure 6a) and PbS (Figure 6b) nanocrystals were arranged in linear rows along the PDA strands, and did not tend to grow in the PDA voids. On the other hand, in the case of $AgNO_3$ aqueous solutions only a few Ag_2S nanocrystals were arranged along the PDA strands with most of the material appears in the PDA domains voids (Figures 2 and 3).

The lower solubility of Ag_2S ($K_{sp} = 3 \times 10^{-50}$) compared with that of CdS and PbS ($K_{sp} = 10^{-28}$) at 25 °C implies higher tendency to form stable nanocrystalline solid deposits.[32]

Yet, we observe that PDA substrate has an inhibitory effect to Ag_2S nucleation, compared with the enhancing effect in the cases of CdS and PbS. Moreover, in the latter cases a well-defined crystallographic alignment between the PDA substrate and the incipient nanocrystals was evident,[10,12,28,29] in contrast to the Ag_2S case where no unique crystallographic orientation was observed. Also, the spherical shapes of nano-Ag_2S might indicate a different interaction between the PDA surface and the mineral, compared to pyramidal or flat triangular shape of the PbS nanocrystals on PDA.[29]

The valency of the metal ions present in the subphase is implicated in the different nucleation behavior of the

metal sulfides on PDA. PDA films consist of amphiphilic PCDA molecules that are topochemically photopolymerized into linear arrays at the air−water interface, forming micrometer sized 2D crystals. It follows that the immersed carboxylate headgroups form a regular 2D array that preferably binds divalent ions by forming salt-bridges. The introduction of H_2S gas induces nanocrystal epitaxial nucleation at the organic−inorganic interface that results in linear rows along the PDA strands.[12,29] Therefore, PDA can be considered to be a catalyst for the divalent nanocrystals growth, acting by lowering the free energy of nucleation on the surface. Monovalent Ag^+ ions, that are electrostatically attracted to the carboxylate groups on the PDA surface, require twice as many ions for electric neutrality, presumably forming a dense charged layer, which is incommensurate with the PDA structure. Thus, the PDA apparently inhibits oriented nanocrystal nucleation of Ag_2S as opposed to its catalytic effect in the case of divalent ions. Studies of sulfides of other monovalent metal ions are underway in order to examine the role of the metal cation valency on the nucleation of semiconductor nanocrystals on PDA.

Conclusions

In summary, we have showed that PDA Langmuir films play a dominant role in controlling the lateral arrangement and size of chemically deposited Ag_2S nanocrystals. In the absence of PDA, Ag_2S is deposited as interconnected particles that are about 50 nm in size that are randomly oriented at the air−solution interface. In the presence of PDA, two crystal populations are obtained: small, ca. 8 nm nanocrystals arranged along the PDA strands, and larger Ag_2S crystals of ca. 50 nm that are found in the voids of the PDA film. The linearly arranged nanocrystals did not have a specific orientation with respect to the PDA film template. These results indicate that the valency of the metal ions present in the subphase is an important factor in the nucleation and growth of metal sulfide nanocrystals on PDA.

Acknowledgment. We thank Dr. D. Mogilyanski for carrying out the XRD measurements, L. Burlaka and Dr. Y. Levi-Kalisman for performing the TEM and SEM studies, R. Golan and J. Jopp for expert assistance with AFM. We are also most grateful to Dr. V. Ezersky for carrying out the TEM characterization and for insightful discussions. This work was supported by a research grant from Intel Corporation, and by the US-Israel Binational Science Foundation, Grant #2002059.

References

(1) Okawa, Y.; Aono, M. *Riken Rev.* **2001**, *37*, 3−6.
(2) Saito, A.; Urai, Y.; Itoh, K. *Langmuir* **1996**, *12*, 3938−3944.
(3) Lu, Y.; Yang, Y.; Sellinger, A.; Lu, M. *Nature* **2001**, *410*, 913−917.
(4) Kuriyama, K.; Kikuchi, H.; Kajiyama, T. *Langmuir* **1996**, *12*, 6468−6472.
(5) Kuriyama, K.; Kikuchi, K.; Kajiayama, T. *Langmuir* **1998**, *14*, 1130−1138.
(6) Lio, A.; Reichert, A.; Ahn, D. J.; Nagy, J. O. *Langmuir* **1997**, *13*, 6624−6532.
(7) Lifshitz, Y., M. Sc. Dissertation, Department of Materials Engineering, Ben Gurion University of Negev, 2004, pp 47−48.
(8) Wang, S.; Li, Y.; Ramirez, J.; Wang, P. G.; Leblanc, R. M. *Langmuir* **1997**, *13*, 1677−1681.
(9) Wang, S.; Lunn, R.; Krafft, M. P.; Leblanc, R. M. *Langmuir* **2000**, *16*, 2882−2886.
(10) Berman, A.; Charych, D. *J. Cryst. Growth* **1999**, *198/199*, 796−801.
(11) Sasaki, D. Y.; Carpick, R. W.; Burns, A. R. *J. Colloid Interface Sci.* **2000**, *229*, 490−495.
(12) Belman, N.; Berman, A.; Ezersky, V.; Lifshitz, Y.; Golan, Y. *Nanotechnology* **2004**, *15*, S316−S321.
(13) Wyckoff, R. W. G. *Crystal Structures*; Wiley: New York, 1965; Vol. 1.
(14) Hull, S.; Keed, D. A.; Sivia, D. S.; Madden, P. A.; Wilson, M. *J. Phys.: Condens. Matter* **2002**, *14*, L9-L17.
(15) Schaaff, T. G.; Rodinone, A. J. *J. Phys. Chem. B* **2003**, *107*, 10416−10422.
(16) Bruhwiler, D.; Leiggener, C.; Calzaferri, G. In *Proceedings of the 13th International Zeolite Conference*; Galarneau, A., Renzo, F. D., Fajula, F., Vedrine, J., Eds.: Montpelier: France, 2001; pp 1−6.
(17) Peng, X. S.; Meng, G. W.; Zhang, J.; Wang, X. F.; Zhao, L. X.; Wang, Y. W.; Zhang, L. D. *Mater. Res. Bull.* **2002**, *37*, 1369−1375.
(18) Bruhwiler, D.; Leiggener, C.; Glaus, S.; Calzaferri, G. *J. Phys. Chem. B* **2002**, *106*, 3770−3777.
(19) Lu, Q.; Gao, F.; Zhao, D. *Nanotechnology* **2002**, *13*, 741−745.
(20) Motte, L.; Pileni, M. P. *J. Phys. Chem. B* **1998**, *102*, 4104−4109.
(21) Sun, Y.; Riggs, J. E.; Rollins, H. W.; Guduru, R. *J. Phys. Chem. B* **1999**, *103*, 77−82.
(22) Wang, C.; Zhang, X.; Qian, X.; Wang, W.; Qian, Y. *Mater. Res. Bull.* **1998**, *33*, 1083−1086.
(23) Maghraoui, H. M.; Dachraoui, M.; Belgacem, S.; Buhre, K. D.; Kunst, R.; Cowache, P.; Lincot, D. *Thin Solid Films* **1996**, *288*, 217−223.
(24) Akamatsu, K.; Takei, S.; Mizuhata, M.; Kajinami, A.; Deki, S.; Takeok, S.; Fujii, M.; Hayashi, S.; Yamamoto, K. *Thin Solid Films* **2000**, *359*, 55−60.
(25) Kumar, R. V.; Palchik, O.; Koltypin, Y.; Diamant, Y.; Gedanken, A. *Ultrason. Sonochem.* **2002**, *9*, 65−70.
(26) Qian, X.; Yin, J.; Feng, S.; Liu, S.-h.; Zhu, Z.-k. *J. Mater. Chem.* **2001**, *11*, 2504−2506.
(27) Berman, A.; Ahn, D. J.; Lio, A.; Reichert, M. S. A.; Charych, D. *Science* **1995**, *296*, 515−519.
(28) Berman, A.; Charych, D. *Adv. Mater.* **1999**, *11*, 296−300.
(29) Berman, A.; Belman, N.; Golan, Y. *Langmuir* **2003**, *19*, 10962−10966.
(30) van Huis, M. A.; van Veen, A.; Schut, H.; Eijt, S. W. H.; Kooi, B. J.; De Hosson, J. Th. M.; Hibma, T. *Rev. Adv. Mater. Sci.* **2003**, *4*, 60−64.
(31) Batabyal, S. K.; Basu, C.; Das, A. R.; Sanyal, G. S. *Cryst. Growth Des.* **2004**, *4*, 509−511.
(32) Hodes, G. *Chemical Solution Deposition of Semiconductor Films*; Marcel Dekker: New York, 2003.

CG049752L

Continuum Mech. Thermodyn. (2005)
DOI 10.1007/s00161-004-0200-6

ORIGINAL ARTICLE

A. D. Drozdov · M. Gottlieb

Constitutive equations for non-affine polymer networks with slippage of chains

Received: 19 November 2004 / Accepted: 9 December 2004 / Published online: 25 May 2005

Abstract A model is derived for isothermal three-dimensional deformation of polymers with finite strains. A polymer fluid is treated as a permanent network of chains bridged by junctions (entanglements). Macrodeformation of the medium induces two motions at the micro-level: (i) sliding of junctions with respect to their reference positions that reflects non-affine deformation of the network, and (ii) slippage of chains with respect to entanglements that is associated with unfolding of back-loops. Constitutive equations are developed by using the laws of thermodynamics. Three important features characterize the model: (i) the symmetry of relations between the elongation of strands and an appropriate configurational tensor, (ii) the strong nonlinearity of the governing equations, and (iii) the account for the volumetric deformation of the network induced by stretching of chains. The governing equations are applied to the numerical analysis of extensional and shear flows. It is demonstrated that the model adequately describes the time-dependent response of polymer melts observed in conventional rheological tests.

Keywords Polymer fluids · Non-affine networks · Chain stretching · Constitutive equations · Viscoplasticity

1 Introduction

This paper deals with modeling the time-dependent response of dense polymer fluids (melts and concentrated solutions) at finite strains. Although this subject has been a focus of attention in the past three decades, it is difficult to mention constitutive equations that adequately describe the characteristic features of the viscoelastic behavior of polymer fluids observed in extensional and shear flows, on the one hand, and that are relatively simple for their numerical implementation, on the other.

Conventional constitutive equations for polymer fluids based on the concept of non-affine networks [1–4] presume that strands in a network are rigidly connected with junctions, whereas the junctions can slide with respect to their positions in the bulk medium. An important advantage of this approach is that the sliding process is described by ordinary differential equations (whose form is determined by appropriate kinematic hypotheses), which implies that the governing equations can be implemented for numerical simulation of flows in domains with complicated geometries. Another advantage of these models is that they do not distinguish between flows of dense and dilute polymer systems, because, from the physical standpoint, deformation of a strand between entanglements in a polymer melt is treated in the same way as deformation of a chain in a dilute polymer solution. This allows such phenomena as strain hardening in transient extensional flows and stress overshoot in start-up shear flows (which are observed experimentally in solutions, as well as in melts) to be described

Communicated by S. H. Faria

A. D. Drozdov (✉) · M. Gottlieb
Department of Chemical Engineering, Ben-Gurion University of the Negev, P.O. Box 653, Beer-Sheva 84105, Israel
E-mail: aleksey@bgumail.bgu.ac.il

by the same governing equations. Constitutive equations for permanent non-affine networks may easily be extended to transient networks (where active strands separate from their junctions and dangling strands merge with the network [6, 7], or, in other words, where chains leave the tubes formed by surrounding molecules due to curvilinear diffusion and new topological constraints are created being induced by the entanglement–disentanglement process [8]). Regretfully, this extension is either overly simplified (when the rates of breakage and reformation of strands are assumed to be determined by macro-deformation [9]), or leads to overly complicated integral governing equations which cannot be applied to the numerical simulation of engineering problems. Some compromise between the two extremes is based on the Peterlin's approximation, but its mathematical basis is rather questionable. It should be noted that in this brief discussion, we do not distinguish between the classical non-affine models with sliding junctions and new micro-mechanical approaches [10–13], where "segmental stretch" is associated with slippage of strands with respect to their junctions (which move affinely with the bulk medium), because they result in the same classes of governing equations.

From the kinematical standpoint, an important difference between dense (melts and concentrated solutions) and dilute polymer fluids consists in the fact that in the dense systems, changes in the elongation of strands and in the orientation of appropriate tubes may occur independently (due to the reptative motion of chains inside their tubes), whereas in the dilute systems, the position of the end-to-end vector for a chain uniquely determines its orientation and elongation. This means that the set of independent variables in the description of the mechanical response of dense systems should necessarily include an analog of the elongation ratio for an "average" chain and an analog of the conformational tensor for an "average" tube. Although this fact was recognized about two decades ago [8], it was presumed that the elongation of chains may be disregarded in the analysis of conventional rheological tests, because the characteristic rate of this process (the inverse of the maximum Rouse time) noticeably exceeds the characteristic rate of macro-deformation. This hypothesis was questioned in several studies, which demonstrated that the account for chain stretching could substantially improve the quality of fitting observations (see [14, 15] and the bibliography therein). However, no physical mechanism was clearly indicated that could slow down substantially the Rouse relaxation time.

Important progress in the analysis of dense polymer systems has been done in the pom–pom model and its modifications [16–21]. First, it was found that pulling arms of highly branched polymers inside a tube for the backbone part of the pom–pom molecule and their withdrawal from the tube may serve as a mechanism necessary for relatively slow elongation of an "average" chain. Secondly, a relatively simple set of governing equations was developed for the elongation ratio of the backbone chain and the configurational tensor for the orientation of the tube.

The pom–pom model has a number of advantages that were mentioned in the original publications. Some shortcomings of the differential version of the pom–pom constitutive equations were discussed in [19], where predictions of this model were compared with experimental data. From the mathematical standpoint, the most important disadvantage of the differential version of this model is that the governing equations for the elongation ratio and the configurational tensor are not symmetric: the kinetic equation for the backbone stretch includes the configurational tensor, whereas the governing equation for the latter is independent of the elongation ratio. Among other inconsistencies of the pom-pom model, one can mention (i) the linear dependence of the elastic recovery force on the backbone stretch (even for Gaussian chains, this linearity is violated in a network of compressible chains by the presence of the entropic contribution into the strain energy driven by volume delation) [15], and (ii) the fact that the third principal invariant of the configurational tensor does not equal unity (as it should be expected for incompressible fluids where this tensor coincides with the left Cauchy–Green tensor [19]).

At first sight, these remarks appear to be contradictory, because we refer to compressible chains in (i) and to incompressible deformations in (ii), which requires some explanation. To clarify this assertion, we consider transformation of the initial configuration of a polymer fluid into its actual (deformed) configuration as a superposition of three transformations: (i) from the initial state into the first intermediate state characterized by sliding of junctions with respect to their reference positions (motion of tubes with respect to their environment), (ii) from the first intermediate state to the second intermediate state determined by sliding of strands with respect to entanglements (stretching of chains with respect to their tubes), and (iii) from the second intermediate state to the actual state (this transformation is associated with elastic deformation of chains). Observations on polymer melts demonstrate that macro-deformation (from the initial to actual state) is incompressible. Conventional models for non-affine networks presume that transformation from the initial to the first intermediate state (sliding of junctions) is incompressible as well. However, the stretching of strands changes the volume occupied by macromolecules, which implies that their elastic deformation should be compressible to ensure the incompressibility of macro-deformation. Within this scenario, the conclusion (i) refers to elastic deformation of chains, whereas the statement (ii) deals with macro-deformation of a polymer fluid.

The objective of this work is twofold: (i) to derive differential constitutive equations for a polymer fluid that are similar to the pom–pom model, but that are free from the above shortcomings, and (ii) to perform numerical simulation of extensional and shear flows and to demonstrate that the governing equations describe qualitatively the most important phenomena observed in experiments.

Unlike the pom–pom model, we do not restrict ourselves to highly branched polymers, presuming that the unfolding of back-loops and removal of unstable loops may serve as a relatively slow mechanism for stretching even linear macromolecules [22]. Another difference between this study and previous publications is that we do not use configurational tensors and develop governing equations by using the conventional apparatus of continuum mechanics. As our goal is to derive a model that can be implemented for numerical simulation of complex flows, we confine ourselves to deterministic constitutive equations and disregard stochastic processes associated with random constraint release at chain stretching [14, 23, 24].

The study is organized as follows. Kinematic equations for sliding of junctions and slippage of chains with respect to entanglements are developed in Sect. 2. Constitutive equations for a dense polymer fluid are derived in Sect. 3 by using the laws of thermodynamics. The set of adjustable parameters in the governing equations is discussed in Sect. 4. Uniaxial extensional flows and shear flows are studied in Sects. 5 and 6, respectively, where explicit expressions are developed for steady viscosities, whereas transient regimes of deformation are analyzed numerically. Some concluding remarks are formulated in Sect. 7.

2 Kinematics of a network with sliding junctions

We begin with the analysis of the deformation of an individual strand, whose ends are connected to two nearby junctions (entanglements) located at points with radius vectors $\mathbf{R}_1$ and $\mathbf{R}_2$ in the initial (stress-free) state. These points of the bulk medium occupy the positions in the actual (deformed) state at an arbitrary instant $t \geq 0$ that are determined by the radius vectors $\mathbf{r}_1(t)$ and $\mathbf{r}_2(t)$. Transformation of the initial state into the actual state is described by the deformation gradient $\mathbf{F}(t)$.

Two dissipative processes are introduced at the micro-level:

1. sliding of junctions (entanglements) with respect to their reference positions in the bulk medium,
2. slippage of chains with respect to appropriate entanglements.

The sliding of junctions reflects non-affine deformation of the network. It is characterized by the deformation gradient $\mathbf{F}_n(t)$. Due to the sliding process, at arbitrary time $t \geq 0$, the vector $\mathbf{r}_n(t)$ from one junction point to the other reads

$$\mathbf{r}_n(t) = \mathbf{F}_n(t) \cdot \quad \mathbf{R},$$

where $\mathbf{R} = \mathbf{R}_2 - \mathbf{R}_1$, and the dot stands for inner product.

Slippage of a chain with respect to its entanglements is treated as elongation (contraction) of a strand between its junctions that is described by the deformation gradient

$$\mathbf{F}_s(t) = \lambda(t)\mathbf{I}, \tag{1}$$

where $\lambda(t) \quad 0$ is the strand elongation and $\mathbf{I}$ denotes the unit tensor. Equation (1) describes deformation of a strand, at which its length is increased by a factor of λ (stretching of an appropriate chain in its tube), while its direction (characterized by the position of the tube) remains unchanged. The coefficient λ in Eq. (1) is treated as an additional state variable in the model which depends on time and the position of a chain, but which is independent of the chain direction (an isotropic sliding). For the sake of brevity, the dependence of all functions on radius vector $\mathbf{R}$ is omitted.

The transition from the initial end-to-end vector of the strand $\mathbf{R}$ to its current end-to-end vector $\mathbf{r}\ (t)$ induced by sliding of junctions and slippage of chains with respect to entanglements is characterized by the deformation gradient

$$\mathbf{F}\ (t) = \mathbf{F}_s(t) \cdot \mathbf{F}_n(t). \tag{2}$$

The subscript index " " denotes viscoplastic deformation, as we associate the dissipative processes (sliding of junctions and slippage of chains) with viscoplasticity of polymer networks.

The elastic deformation gradient $\mathbf{F}_e(t)$ is determined as the deformation gradient from the intermediate state of a strand, characterized by the end-to-end vector $\mathbf{r}\ (t)$, to its actual state, described by the end-to-end vector $\mathbf{r}(t)$. The multiplicative decomposition formula for the deformation gradient $\mathbf{F}(t)$ reads

$$\mathbf{F}(t) = \mathbf{F}_e(t) \cdot \mathbf{F}\ (t). \tag{3}$$

Substitution of expressions (1) and (2) into Eq. (3) implies that

$$\mathbf{F}(t) = \lambda(t)\mathbf{F}_e(t) \cdot \mathbf{F}_n(t). \tag{4}$$

Differentiation of Eq. (4) with respect to time results in

$$\frac{d\mathbf{F}}{dt}(t) = \frac{d\lambda}{dt}(t)\mathbf{F}_e(t) \cdot \mathbf{F}_n(t) + \lambda(t)\frac{d\mathbf{F}_e}{dt}(t) \cdot \mathbf{F}_n(t) + \lambda(t)\mathbf{F}_e(t) \cdot \frac{d\mathbf{F}_n}{dt}(t).$$

Introducing the velocity gradients by the conventional formulas

$$\mathbf{L}(t) = \frac{d\mathbf{F}}{dt}(t) \cdot \mathbf{F}^{-1}(t), \quad \mathbf{L}_e(t) = \frac{d\mathbf{F}_e}{dt}(t) \cdot \mathbf{F}_e^{-1}(t), \quad \mathbf{l}_n(t) = \frac{d\mathbf{F}_n}{dt}(t) \cdot \mathbf{F}_n^{-1}(t), \tag{5}$$

we find that

$$\mathbf{L}(t) = \mathbf{L}_e(t) + \mathbf{L}_n(t) + \mathbf{L}_s(t), \tag{6}$$

where

$$\mathbf{L}_n(t) = \mathbf{F}_e(t) \cdot \mathbf{l}_n(t) \cdot \mathbf{F}_e^{-1}(t), \quad \mathbf{L}_s(t) = D_s(t)\mathbf{I}, \quad D_s(t) = \frac{1}{\lambda(t)}\frac{d\lambda}{dt}(t). \tag{7}$$

The left and right Cauchy–Green tensors for elastic deformation are given by

$$\mathbf{B}_e(t) = \mathbf{F}_e(t) \cdot \mathbf{F}_e^{\top}(t), \quad \mathbf{C}_e(t) = \mathbf{F}_e^{\top}(t) \cdot \mathbf{F}_e(t), \tag{8}$$

where $\top$ stands for transpose. Differentiating the first equality in Eq. (8) with respect to time and using Eq. (5), we arrive at the kinetic equation for the left Cauchy–Green tensor

$$\frac{d\mathbf{B}_e}{dt}(t) = \mathbf{L}_e(t) \cdot \mathbf{B}_e(t) + \mathbf{B}_e(t) \cdot \mathbf{L}_e^{\top}(t). \tag{9}$$

It follows from Eqs. (6), (7) and (9) that

$$\frac{d\mathbf{B}_e}{dt}(t) = [\mathbf{L}(t) \cdot \mathbf{B}_e(t) + \mathbf{B}_e(t) \cdot \mathbf{L}^{\top}(t)] - [\mathbf{L}_n(t) \cdot \mathbf{B}_e(t) + \mathbf{B}_e(t) \cdot \mathbf{L}_n^{\top}(t)] - 2D_s(t)\mathbf{B}_e(t). \tag{10}$$

Differentiation of the other equality in Eq. (8) results in

$$\frac{d\mathbf{C}_e}{dt}(t) = 2\mathbf{F}_e^{\top}(t) \cdot \mathbf{D}_e(t) \cdot \mathbf{F}_e(t), \tag{11}$$

where

$$\mathbf{D}_e(t) = \frac{1}{2}[\mathbf{L}_e(t) + \mathbf{L}_e^{\top}(t)] \tag{12}$$

is the rate-of-strain tensor for elastic deformation. Equations (6) and (7) imply that

$$\mathbf{D}(t) = \mathbf{D}_e(t) + \mathbf{D}_n(t) + D_s(t)\mathbf{I}, \tag{13}$$

where the rate-of-strain tensors $\mathbf{D}(t)$ and $\mathbf{D}_n(t)$ are introduced by the formulas similar to Eq. (12). Substituting expression (13) into Eq. (11), we obtain

$$\frac{d\mathbf{C}_e}{dt}(t) = 2[\mathbf{F}_e^{\top}(t) \cdot \mathbf{D}(t) \cdot \mathbf{F}_e(t) - \mathbf{F}_e^{\top}(t) \cdot \mathbf{D}_n(t) \cdot \mathbf{F}_e(t) - D_s(t)\mathbf{C}_e(t)]. \tag{14}$$

Equations (10) and (14) describe the evolution of the left and right Cauchy–Green tensors for an arbitrary sliding process. Following [1], we suppose that the vorticity tensor for sliding of junctions $\Omega_n(t)$ is proportional to the vorticity tensor for macro-deformation $\Omega(t)$,

$$\Omega_n(t) = \quad (t)\Omega(t), \tag{15}$$

where $\quad(t) \in (0, 1)$ is a coefficient of proportionality, and

$$\Omega(t) = \frac{1}{2}[\mathbf{L}(t) - \mathbf{L}^{\top}(t)], \quad \Omega_n(t) = \frac{1}{2}[\mathbf{L}_n(t) - \mathbf{L}_n^{\top}(t)].$$

Without loss of generality, we write

$$\mathbf{D}_n(t) = \quad (t)\mathbf{D}(t) + \mathbf{d}_n(t), \tag{16}$$

where $\mathbf{d}_n(t)$ is a new symmetric tensor. It follows from Eqs. (15) and (16) that

$$\mathbf{L}_n(t) = \quad (t)\mathbf{L}(t) + \mathbf{d}_n(t). \tag{17}$$

Substitution of expressions (16) and (17) into Eqs. (10) and (14) results in the differential equations

$$\frac{d\mathbf{B}_e}{dt}(t) = (1 - \quad (t))(\mathbf{L}(t)\cdot\mathbf{B}_e(t) + \mathbf{B}_e(t)\cdot\mathbf{L}^\top(t)) - (\mathbf{d}_n(t)\cdot\mathbf{B}_e(t) + \mathbf{B}_e(t)\cdot\mathbf{d}_n(t)) - 2D_s(t)\mathbf{B}_e(t), \tag{18}$$

$$\frac{d\mathbf{C}_e}{dt}(t) = 2[(1 - \quad (t))\mathbf{F}_e^\top(t)\cdot\mathbf{D}(t)\cdot\mathbf{F}_e(t) - \mathbf{F}_e^\top(t)\cdot\mathbf{d}_n(t)\cdot\mathbf{F}_e(t) - D_s(t)\mathbf{C}_e(t)]. \tag{19}$$

Our aim now is to derive kinetic equations for the principal invariants $J_{ek}(t)$ $(k = 1, 2, 3)$ of the tensor $\mathbf{C}_e(t)$. For this purpose, we introduce the temporal notation

$$\mathbf{d}(t) = (1 - \quad (t))\mathbf{D}(t) - \mathbf{d}_n(t)$$

and present Eq. (19) in the form

$$\frac{d\mathbf{C}_e}{dt}(t) = 2[\mathbf{F}_e^\top(t)\cdot\mathbf{d}(t)\cdot\mathbf{F}_e(t) - D_s(t)\mathbf{C}_e(t)]. \tag{20}$$

It follows from Eqs. (8) and (20) that

$$\begin{aligned}
\frac{d\mathbf{C}_e^2}{dt}(t) &= 2\big[\mathbf{F}_e^\top(t)\cdot\big(\mathbf{d}(t)\cdot\mathbf{B}_e(t) + \mathbf{B}_e(t)\cdot\mathbf{d}(t)\big)\cdot\mathbf{F}_e(t) - 2D_s(t)\mathbf{C}_e^2(t)\big],\\
\frac{d\mathbf{C}_e^3}{dt}(t) &= 2\big[\mathbf{F}_e^\top(t)\cdot\big(\mathbf{d}(t)\cdot\mathbf{B}_e^2(t) + \mathbf{B}_e(t)\cdot\mathbf{d}(t)\cdot\mathbf{B}_e(t) + \mathbf{B}_e^2(t)\cdot\mathbf{d}(t)\big)\cdot\mathbf{F}_e(t) - 3D_s(t)\mathbf{C}_e^3(t)\big].
\end{aligned} \tag{21}$$

According to Eqs. (20) and (21), the first invariants $I_{ek}(t) = \mathbf{I} : \mathbf{C}_e^k(t)$ of the tensors $\mathbf{C}_e^k(t)$ obey the differential equations

$$\begin{aligned}
\frac{dI_{e1}}{dt}(t) &= 2[\mathbf{B}_e(t) : \mathbf{d}(t) - D_s(t)I_{e1}(t)],\\
\frac{dI_{e2}}{dt}(t) &= 4\big[\mathbf{B}_e^2(t) : \mathbf{d}(t) - D_s(t)I_{e2}(t)\big],\\
\frac{dI_{e3}}{dt}(t) &= 6\big[\mathbf{B}_e^3(t) : \mathbf{d}(t) - D_s(t)I_{e3}(t)\big],
\end{aligned} \tag{22}$$

where the colon stands for convolution. The principal invariants $J_{ek}(t)$ of the tensor $\mathbf{C}_e(t)$ are calculated as

$$J_{e1}(t) = I_{e1}(t), \quad J_{e2}(t) = \frac{1}{2}\big(I_{e1}^2(t) - I_{e2}(t)\big), \quad J_{e3}(t) = \frac{1}{3}\big(I_{e3}(t) - I_{e1}^3(t) + 3I_{e1}(t)J_{e2}(t)\big). \tag{23}$$

We differentiate Eq. (23) with respect to time, use Eq. (22), and, after simple algebra, arrive at the formulas

$$\begin{aligned}
\frac{dJ_{e1}}{dt}(t) &= 2[\mathbf{B}_e(t) : \mathbf{d}(t) - D_s(t)J_{e1}(t)],\\
\frac{dJ_{e2}}{dt}(t) &= 2\big[\big(J_{e1}(t)\mathbf{B}_e(t) - \mathbf{B}_e^2(t)\big) : \mathbf{d}(t) - 2D_s(t)J_{e2}(t)\big],\\
\frac{dJ_{e3}}{dt}(t) &= 2[\mathbf{I} : \mathbf{d}(t) - 3D_s(t)]J_{e3}(t).
\end{aligned}$$

Returning to the initial notation, we find from these equations that the derivative of an arbitrary smooth function of the principal invariants of the tensor $\mathbf{C}_e(t)$ reads

$$\begin{aligned}
\frac{d}{dt}(J_{e1}(t), J_{e2}(t), J_{e3}(t)) = 2\big[&\quad {}_1(t)\mathbf{B}_e(t) + \quad {}_2(t)\big(J_{e1}(t)\mathbf{B}_e(t) - \mathbf{B}_e^2(t)\big)\\
&+ \quad {}_3(t)J_{e3}(t)\mathbf{I}\big] : [(1 - \quad (t))\mathbf{D}(t) - \mathbf{d}_n(t)]\\
&- 2[\quad {}_1(t)J_{e1}(t) + 2\quad {}_2(t)J_{e2}(t) + 3\quad {}_3(t)J_{e3}(t)]D_s(t),
\end{aligned} \tag{24}$$

where

$$_k(t) = \frac{\partial}{\partial J_{ek}}(J_{e1}(t), J_{e2}(t), J_{e3}(t)).$$

Our purpose now is to apply Eq. (24) in order to develop constitutive equations for a polymer fluid by using the laws of thermodynamics.

3 Constitutive equations

A polymer is treated as an incompressible network of chains bridged by junctions (entanglements) that slide with respect to their reference positions. The incompressibility condition for macro-deformation implies that for any $t \geq 0$,

$$\mathbf{I} : \mathbf{D}(t) = 0. \tag{25}$$

It is assumed that the sliding process also induces volume-preserving transformation,

$$\mathbf{I} : \mathbf{D}_n(t) = 0.$$

This condition together with Eqs. (16) and (25) results in

$$\mathbf{I} : \mathbf{d}_n(t) = 0. \tag{26}$$

With reference to [25, 26], the following expression is adopted for the strain energy per unit mass W at a fixed temperature :

$$W(t) = \frac{1}{2}k_B N \quad [(J_{e1}(t) - 3) - \quad \ln J_{e3}(t)], \tag{27}$$

where k_B is Boltmann's constant, N is the number of strands per unit mass, and is a positive constant that will be determined later. The first term on the right-hand side of Eq. (27) describes the entropic strain energy of non-interacting Gaussian chains, while the other term characterizes the entropy of their interaction (when chains are treated as an ideal gas of particles). The negativity of the second term at three-dimensional extension (J_{e3} 1) means that the entropy of an ensemble of chains increases with its volume.

An important shortcoming of expression (27) is that it implies the same order of magnitude for shear and bulk moduli [27]. Another disadvantage of this formula is that it leads to unrealistic results for the ratio of the lateral strain to the longitudinal strain at uniaxial compression [28]. Finally, our numerical analysis demonstrates that the presence of the logarithmic term in Eq. (27) is insufficient to ensure "finite extensibility" of strands at uniaxial extension with constant strain rates: the function $\lambda(t)$ accepts physically unrealistic values at relatively large strain rates within the experimental time-scale. To guarantee reasonable constraints on the elongation ratio λ, an additional function of volumetric strain should be introduced on the right-hand side of Eq. (27). This function is associated with hydrostatic pressure necessary to maintain the stress-free state of a network in its initial configuration. Three functions are conventionally employed to describe the dependence of strain energy on volume deformation [29–31]:

$$U = \frac{\mu_1}{2}(J_{e3} - 1)^2, \quad U = \frac{\mu_1}{2}(\ln J_{e3})^2, \quad U = \frac{\mu_1}{2}\left(J_{e3}^{-} - 1\right). \tag{28}$$

In these equations, μ_1 (an analog of the bulk modulus) and (a dimensionless exponent) are positive constants. As the last formula in Eq. (28) (the so-called general Blatz–Ko medium [32]) has a number of advantages compared to the other relations, we chose the extra term in Eq. (27) in this form.

It is worth noting that the summation of contributions (27) and (28) into the strain energy of a network should be performed with caution, because Eq. (27) describes the entropic strain energy per unit mass, whereas Eq. (28) determines the elastic strain energy per unit volume in the unloaded state. The latter means that for a small element with mass m and volume $_n$ in the intermediate state determined by sliding of junctions, the total strain energy reads

$$(t) = \int_m W(t)dm + \int_n U(t)d\ _n, \tag{29}$$

where dm is mass element, and $d\ _n$ is volume element. Due to the incompressibility condition for the sliding process, the latter quantity coincides with the volume element in the initial state, and, as a consequence, it is independent of time. Differentiation of Eq. (29) with respect to time implies that

$$\frac{d}{dt}(t) = \int_{\ m} \frac{dW}{dt}(t)dm + \int_{\ _n} \frac{dU}{dt}(t)d\ _n.$$

Bearing in mind that

$$dm = \ d\ , \tag{30}$$

where $\ $ is density, and $d\ $ is volume element in the actual state, and

$$\frac{d}{d\ _n} = \sqrt{J_{e3}},$$

we find that

$$\frac{d}{dt}(t) = \int \left[\ \frac{dW}{dt}(t) + \frac{1}{\sqrt{J_{e3}(t)}}\frac{dU}{dt}(t)\right]d\ , \tag{31}$$

where $\ $ is the volume occupied by element $\ m$ in the deformed state.

Applying formula (24) to expressions (27) and (28) and using Eqs. (25) and (26), we obtain

$$\frac{dW}{dt}(t) = k_B N\ \ \{\mathbf{B}_e(t) : [(1 - \ \ (t))\mathbf{D}(t) - \mathbf{d}_n(t)] - (J_{e1}(t) - 3\ \ )D_s(t)\},$$
$$\frac{dU}{dt}(t) = 3\mu_1 J_{e3}^{-\ \ (t)}D_s(t).$$

Substitution of these equations into Eq. (31) results in

$$\frac{d}{dt}(t) = \int\ \ \mu\Big[\mathbf{B}_e(t) : ((1 - \ \ (t))\mathbf{D}(t) - \mathbf{d}_n(t)) - (J_{e1}(t) - 3\ \ - 3\ \ J_{e3}^{-\ \ -\frac{1}{2}}(t))D_s(t)\Big]d\ , \tag{32}$$

where $\mu = \ k_B N\ $, and $\ = \mu_1/\mu$.

For isothermal deformations of an incompressible medium at the reference temperature $\ $, the Clausius–Duhem inequality reads

$$\int_{\ m} Q(t)dm = -\frac{d}{dt}(t) + \int\ \ \ '(t) : \mathbf{D}(t)d\ \ \geq 0,$$

where Q is internal dissipation per unit mass, $\ $ is the Cauchy stress tensor, and the prime stands for the deviatoric component of a tensor. Using Eqs. (30) and (32), we present this equation in the differential form

$$Q(t) = [\ \ (t) - \mu(1 - \ \ (t))\mathbf{B}_e(t)]' : \mathbf{D}(t) + \mu\mathbf{B}'_e(t) : \mathbf{d}_n(t)$$
$$+\mu\Big(J_{e1}(t) - 3\ \ - 3\ \ J_{e3}^{-\ \ -\frac{1}{2}}(t)\Big)D_s(t), \tag{33}$$

To derive Eq. (33) we employed the formulas

$$\mathbf{B}_e : \mathbf{D} = \mathbf{B}'_e : \mathbf{D}, \quad \mathbf{B}_e : \mathbf{d}_n = \mathbf{B}'_e : \mathbf{d}_n,$$

which follow from Eqs. (25) and (26). The following expression is adopted for the internal dissipation per unit volume:

$$Q(t) = 2\ _n(t)\mathbf{d}_n(t) : \mathbf{d}_n(t) + 3\ _s(t)D_s^2(t). \tag{34}$$

The first term on the right-hand side of Eq. (34) describes dissipation of energy driven by sliding of junctions, whereas the other term determine internal dissipation induced by sliding of chains with respect to entanglements (as the latter motion is one-dimensional, the coefficient 3 is introduced instead of 2). Substituting expression (34) into Eq. (33) and equating appropriate terms, we arrive at the governing equation

$$(t) = -P(t)\mathbf{I} + \mu(1 - \ \ (t))\mathbf{B}_e(t), \tag{35}$$

where $P(t)$ is an unknown pressure, and the kinetic equations for $\mathbf{d}_n(t)$ and $D_s(t)$,

$$\mathbf{d}_n(t) = \frac{\mu}{2\ _n(t)}\mathbf{B}'_e(t), \quad D_s(t) = \frac{\mu}{3\ _s(t)}\Big[J_{e1}(t) - 3\quad - 3\ \ J_{e3}^{-\ -\frac{1}{2}}(t)\Big]. \tag{36}$$

Combining the first equality in Eq. (36) with Eq. (18) and bearing in mind that $\mathbf{B}'_e = \mathbf{B}_e - \frac{1}{3}J_{e1}\mathbf{I}$, we arrive at the formula

$$\frac{d\mathbf{B}_e}{dt}(t) = (1 - \quad (t))(\mathbf{L}(t)\cdot\mathbf{B}_e(t) + \mathbf{B}_e(t)\cdot\mathbf{L}^\top(t)) - \frac{\mu}{_n(t)}\left(\mathbf{B}_e^2(t) - \frac{1}{3}J_{e1}(t)\mathbf{B}_e\right) - 2D_s(t)\mathbf{B}_e(t). \tag{37}$$

It follows from Eqs. (7) and (37) that the function

$$\mathbf{b}_e(t) = \lambda^2(t)\mathbf{B}_e(t) \tag{38}$$

satisfies the equation

$$\frac{d\mathbf{b}_e}{dt}(t) = (1 - \quad (t))(\mathbf{L}(t)\cdot\mathbf{b}_e(t) + \mathbf{b}_e(t)\cdot\mathbf{L}^\top(t)) - \frac{\mu}{_n(t)}\ ^2(t)\left(\mathbf{b}_e^2(t) - \frac{1}{3}j_{e1}(t)\mathbf{b}_e(t)\right), \tag{39}$$

where $j_{e1} = \mathbf{I} : \mathbf{b}_e$ is the first invariant of the tensor $\mathbf{b}_e$, and

$$(t) = \frac{1}{\lambda(t)}. \tag{40}$$

Equation (7) together with the second equality in Eq. (36) results in

$$\frac{d\lambda}{dt}(t) = \frac{\mu}{3\ _s(t)}\Big[J_{e1}(t) - 3\quad - 3\ \ J_{e3}^{-\ -\frac{1}{2}}(t)\Big]\lambda(t).$$

It follows from this equation that no elongation of chains occurs in the initial state (where $J_{e1} = 3$ and $J_{e3} = 1$) if the coefficient equals $1 -$. Taking into account this condition, we find that

$$\frac{d\lambda}{dt}(t) = \frac{\mu}{3\ _s(t)}\Big[(J_{e1}(t) - 3) - 3\ \ \Big(J_{e3}^{-\ -\frac{1}{2}}(t) - 1\Big)\Big]\lambda(t). \tag{41}$$

Bearing in mind that $J_{e1} = \ ^2 j_{e1}$ and $J_{e3} = \ ^6$ [the latter formula follows from Eqs. (4) and (8) and the incompressibility conditions for macro-deformation and sliding of junctions], we find from Eqs. (40) and (41) that the function (t) obeys the differential equation

$$\frac{d}{dt}(t) = -\frac{\mu}{_s(t)}\left[\left(\frac{1}{3}\ ^2(t)j_{e1}(t) - 1\right) + \quad (1 - \ ^{-6}\ ^{-3}(t))\right]\ \ (t). \tag{42}$$

Substitution of expressions (38) and (40) into Eq. (35) implies that

$$(t) = -P(t)\mathbf{I} + \mu(1 - \quad (t))\ \ ^2(t)\mathbf{b}_e(t). \tag{43}$$

Formulas (39), (42) and (43) provide a set of constitutive equations for a polymer fluid at an arbitrary three-dimensional deformation with finite strains. The structure of these relations is similar to that of the governing equations in the pom–pom model: (i) the deviatoric part of the stress tensor is proportional to the square of the dimensionless ratio , and (ii) the set of kinetic equations consists of independent evolution equations for the scalar function (t) and the tensor function $\mathbf{b}_e(t)$. However, Eqs. (39) and (42) substantially differ from appropriate equations in the pom-pom model: (i) these equations are symmetric in the sense that the evolution of the deformation tensor $\mathbf{b}_e$ is affected by the ratio , and the evolution of depends on $\mathbf{b}_e$, (ii) Eq. (39) for the deformation tensor is strongly nonlinear even when the ratio adopt its equilibrium value $= 1$, and (iii) "recovery" of the function (t) after instantaneous unloading is described by two micro-mechanisms that are associated with the entropic (the first term in Eq. (42)) and elastic (the other term in this equation) contributions into the strain energy.

4 Adjustable parameters

Equations (39), (42) and (43) involve three positive parameters, μ, and , and three positive functions of time, (t), $_s(t)$ and $_n(t)$. On the one hand, the presence of adaptive functions in governing equations makes the model rather flexible to describe observations. On the other hand, three unknown functions cannot be determined with a reasonable level of accuracy by fitting observations in conventional rheological tests. The latter implies the necessity to introduce phenomenological relations that express the parameters , $_s$ and $_n$ in terms of some quantities that can be found experimentally.

To simplify the analysis, we treat and $_s$ as strain-independent material parameters and assume the viscosity $_n$ to be a function of the strain-rate intensity

$$D_i(t) = (2\mathbf{D}(t) : \mathbf{D}(t))^{\frac{1}{2}}. \tag{44}$$

Two types of polymer fluids are considered. For a type-I fluid, the viscosity $_n$ increases with D_i following the power-law

$$_n = \ ^0_n \left[1 + K \left(\frac{D_i}{D_i^0} \right)^a \right], \tag{45}$$

where ^0_n is the viscosity of sliding of junctions at the zero strain rate, D_i^0 is some reference strain rate intensity, and a is a positive exponent. For a type-II fluid, the viscosity $_n$ decreases with D_i following the Storr formula

$$_n = \ ^0_n \left[1 + K \left(\frac{D_i}{D_i^0} \right)^a \right]^{-1}. \tag{46}$$

It is worth emphasizing at this stage the only two sources of "phenomenological" relations are employed to design the model: (i) the generalized Blatz–Ko formula (28) for the energy of inter-chain interactions, and (ii) the conventional Storr formulas (45) and (46) for the dependence of viscosity on strain rate.

For both types of polymer fluids, the constitutive equations are determined by eight material constants that have transparent physical meaning: (i) the coefficient of proportionality between the vorticity tensors for sliding of junctions and macro-deformation, (ii) the viscosity for slippage of chains with respect to entanglements $_s$, (iii) the zero-strain rate viscosity for sliding of junctions with respect to their reference positions ^0_n, (iv) the coefficient K and the exponent a that characterize the effect of strain-rate intensity on the viscosity of sliding, (v) the elastic modulus μ, (vi) the ratio of moduli associated with elastic and entropic contributions into the strain energy density , and (vii) the exponent that describes changes in the strain energy density induced by volume deformation.

Our aim now is to demonstrate that these parameters can be found by fitting experimental data in conventional tests.

5 Uniaxial extension

We begin with the analysis of stresses at uniaxial extension of a polymer fluid. Points of the medium refer to Cartesian coordinates $\{X_i\}$ $(i = 1, 2, 3)$ in the stress-free state and to Cartesian coordinates $\{x_i\}$ in the deformed state. The current position of entanglements between chains is determined by the Cartesian coordinates $\{\ _i\}$. Uniaxial extension of an incompressible medium is described by the formulas

$$x_1 = k(t)X_1, \quad x_2 = k^{-\frac{1}{2}}(t)X_2, \quad x_3 = k^{-\frac{1}{2}}(t)X_3, \tag{47}$$

where $k(t)$ is the elongation ratio. It is assumed that the sliding process is described by the equations similar to Eq. (47),

$$_1 = \ (t)X_1, \quad _2 = \ ^{-\frac{1}{2}}(t)X_2, \quad _3 = \ ^{-\frac{1}{2}}(t)X_3, \tag{48}$$

where (t) is an unknown function of time. It follows from Eqs. (47) and (48) that

$$\mathbf{F} = k\mathbf{e}_1\mathbf{e}_1 + k^{-\frac{1}{2}}(\mathbf{e}_2\mathbf{e}_2 + \mathbf{e}_3\mathbf{e}_3), \quad \mathbf{F}_n = \ \mathbf{e}_1\mathbf{e}_1 + \ ^{-\frac{1}{2}}(\mathbf{e}_2\mathbf{e}_2 + \mathbf{e}_3\mathbf{e}_3), \tag{49}$$

where $\mathbf{e}_i$ are base vectors of the frame $\{X_i\}$. Substitution of expressions (49) into Eq. (4) implies that

$$\mathbf{F}_e = \frac{1}{\lambda}\left[\frac{k}{\ }\mathbf{e}_1\mathbf{e}_1 + \left(\frac{\ }{k}\right)^{\frac{1}{2}}(\mathbf{e}_2\mathbf{e}_2 + \mathbf{e}_3\mathbf{e}_3)\right]. \tag{50}$$

Combining Eqs. (8) and (50), we find that

$$\mathbf{B}_e = \frac{1}{\lambda^2}\left[\left(\frac{k}{\ }\right)^2\mathbf{e}_1\mathbf{e}_1 + \frac{\ }{k}(\mathbf{e}_2\mathbf{e}_2 + \mathbf{e}_3\mathbf{e}_3)\right].$$

This equation together with Eq. (38) results in

$$\mathbf{b}_e = \left[\left(\frac{k}{\ }\right)^2\mathbf{e}_1\mathbf{e}_1 + \frac{\ }{k}(\mathbf{e}_2\mathbf{e}_2 + \mathbf{e}_3\mathbf{e}_3)\right]. \tag{51}$$

Substitution of expressions (40) and (51) into Eq. (43) implies that

$$= \ {}_1\mathbf{e}_1\mathbf{e}_1 + \ {}_2(\mathbf{e}_2\mathbf{e}_2 + \mathbf{e}_3\mathbf{e}_3),$$

where

$${}_1 = -P + \mu(1 - \ )^{\ 2}\left(\frac{k}{\ }\right)^2, \qquad {}_2 = -P + \mu(1 - \ )^{\ 2}\frac{\ }{k}.$$

It follows from these equations that the stress difference $\ = \ {}_1 - \ {}_2$ is given by

$$= \mu(1 - \ )^{\ 2}\left[\left(\frac{k}{\ }\right)^2 - \frac{\ }{k}\right]. \tag{52}$$

Equation (51) implies that

$$j_{e1} = \left(\frac{k}{\ }\right)^2 + 2\frac{\ }{k}. \tag{53}$$

Substitution of this expression into Eq. (42) results in the differential equation

$$\frac{d}{dt} = -\frac{\mu}{\ _s}\left[\left(\frac{1}{3}\ {}^2\left(\left(\frac{k}{\ }\right)^2 + 2\frac{\ }{k}\right) - 1\right) + \ (1 - \ {}^{-6}\ {}^{-3})\right]\ . \tag{54}$$

It follows from Eq. (47) that

$$\mathbf{L} = \frac{\dot{k}}{k}\left[\mathbf{e}_1\mathbf{e}_1 - \frac{1}{2}(\mathbf{e}_2\mathbf{e}_2 + \mathbf{e}_3\mathbf{e}_3)\right], \tag{55}$$

where $\dot{k} = dk/dt$. This equality together with Eq. (44) implies that

$$D_i = \frac{|\dot{k}|}{k}\sqrt{3}. \tag{56}$$

We now substitute expressions (51) and (55) into Eq. (39). Omitting simple algebra, we arrive at the kinetic equation for the function $\ (t)$

$$\frac{d}{dt} = \ \frac{\ }{k}\frac{dk}{dt} + \frac{\mu}{3\ _n}\frac{k^3 - \ {}^3}{k}\ {}^2. \tag{57}$$

Equations (52), (54) and (57) determine the stress difference $\ $ for an arbitrary deformation program. Our aim now is to study in detail two rheological tests: deformation with a constant strain rate and stress relaxation.

5.1 Deformation with a constant strain rate

For an extensional flow with a constant strain rate $\dot{}$, Eq. (57) is simplified. Bearing in mind that

$$k(t) = \exp(\dot{}\, t), \tag{58}$$

we search a solution of Eq. (57) in the form

$$(t) = z(t)\exp(\dot{}\, t), \tag{59}$$

where $z(t)$ is an unknown function. Substitution of expressions (58) and (59) into Eq. (57) implies the differential equation

$$\frac{dz}{dt} + (1 - \quad)\dot{}\, z = \frac{\mu}{3\ {}_n(\dot{})}\frac{1 - z^3}{z}\ {}^2. \tag{60}$$

It follows from Eqs. (54) and (59) that

$$\frac{d}{dt} = -\frac{\mu}{{}_s}\left[\left({}^2\frac{1 + 2z^3}{3z^2} - 1\right) + \quad(1 - \quad {}^{-6}\ {}^{-3})\right]\ . \tag{61}$$

The initial conditions for Eqs. (60) and (61) are given by

$$z(0) = 1, \qquad (0) = 1. \tag{62}$$

According to Eq. (52), the transient elongational viscosity ${}^{+}_{e} = \qquad /\dot{}$ is determined as

$${}^{+}_{e} = \mu(1 - \quad)\ {}^2\frac{1 - z^3}{\dot{}\, z^2}. \tag{63}$$

Assuming that $z(t) \to z_0$ and $\quad(t) \to \quad {}_0$ as $t \to \infty$, we find from Eq. (60) that

$$\mu\frac{1 - z_0^3}{z_0^2}\ {}^2_0 = 3(1 - \quad)\ {}_n(\dot{})\dot{}. \tag{64}$$

The steady elongational viscosity ${}_e = \lim_{t\to\infty}\ {}^{+}_{e}(t)$ is calculated from Eqs. (63) and (64),

$${}_e(\dot{}) = 3\ {}_n(\dot{})(1 - \quad)^2. \tag{65}$$

It follows from Eqs. (44)–(46), (56), (58) and (65) that ${}^0_n = \frac{1}{3}\ {}^0_e(1 - \quad)^{-2}$, where ${}^0_e$ is the zero strain rate elongational viscosity, whereas the coefficients a and K in Eqs. (45) and (46) can be found in the approximation of an appropriate experimental dependence ${}_e(\dot{})$.

Equation (65) determines the steady elongational viscosity ${}_e$ for an arbitrary strain rate $\dot{}$. A surprising conclusion of our analysis is that the steady elongational viscosity is independent of the ratio . The parameter ${}_0$ that characterizes an average elongation of chains at large times is, however, a function of . To find this dependence, we consider the steady-state solution of Eq. (61). As the elongation ratio λ remains finite, it follows from Eq. (61) that ${}_0$ obeys the equation

$${}^2_0\frac{1 + 2z_0^3}{3z_0^2} = 1 - \quad\left(1 - \quad {}^{-6}_0\ {}^{-3}\right). \tag{66}$$

At relatively large strain rates, when the dimensionless ratio $M = 3(1 - \quad)\ {}_n(\dot{})/(\mu\dot{})$ is large compared with unity, Eq. (64) implies that $z_0 \ll 1$. Neglecting z_0^3 in Eq. (64), we find that

$$\left(\frac{{}_0}{z_0}\right)^2 = M.$$

With the same level of accuracy, Eq. (66) implies that

$$\left(\frac{{}_0}{z_0}\right)^2 = 1 - \quad\left(1 - \quad {}^{-6}_0\ {}^{-3}\right).$$

Table 1 Material parameters for type-I and type-II polymer fluids

Fluid		μ kPa			$_s$ kPa·s	^0_n kPa·s	a	K	D_i^0 s^{-1}
Type-I	0.6	80.0	0.5	1.0	300.0	10.0	0.2	15.0	$0.1\sqrt{3}$
Type-II	0.2	50.0	0.5	1.0	300.0	600.0	0.2	1.2	$0.1\sqrt{3}$

Combination of these equations results in $_0^{-6\ -3} = M - 1 +$. At $M \gg 1$, the right-hand side of this equation can be replaced by M, which implies that

$$_0 = \left(\frac{}{M}\right)^{\frac{1}{6\ +3}}.$$

Returning to the initial notation, we find from this equation that the average elongation ratio for slippage of chains λ_0 in a steady extensional flow with the strain rate $\dot{}$ reads

$$\lambda_0 = \left[\frac{_e(\dot{})\dot{}}{\mu\ \ (1-\ \ )}\right]^{\frac{1}{6\ +3}}. \tag{67}$$

Equation (67) implies that λ_0 is inversely proportional to the modulus μ_1 in Eq. (28). The latter confirms the necessity to account for the elastic contribution into the strain energy density of a polymer network.

To demonstrate how the transient elongational viscosity ^+_e evolves with time, we integrate Eqs. (60) and (61) numerically with initial conditions (62). Integration is performed by the Runge–Kutta method with the time step $t = 1.0 \cdot 10^{-4}$ s for the type-I and type-II polymer fluids with the material parameters listed in Table 1. To assess the effect of the dimensionless ratio , two values of this quantity are considered: $= 1.0$ and $= 10.0$. The strain rates under investigation range from 0.1 to 30.0 s^{-1}, the values conventionally employed in extensional tests. The results of numerical simulation are presented in Figs. 1 to 3.

In Fig. 1, the transient elongational viscosity ^+_e is plotted versus time. For both types of polymer fluids, given a strain rate $\dot{}$, the elongational viscosity monotonically increases with t and reaches its steady-state value within the experimental time-scale (except for deformation with the smallest strain rate $\dot{}_{\min} = 0.1$ s^{-1}). The instant when the graph of ^+_e in extensional flow with a strain rate $\dot{}$ deviates from that for $\dot{}_{\min}$ decreases with strain rate, as well as the instant when the transient viscosity reaches its steady value. The growth of by an order of magnitude weakly affects the elongational viscosity.

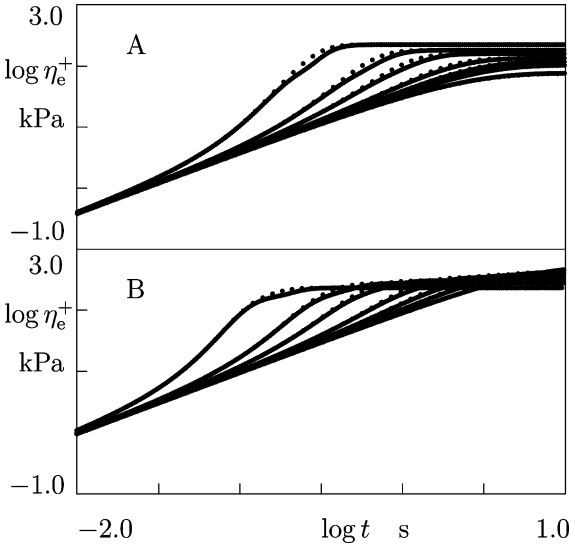

Fig. 1 The transient elongational viscosity ^+_e versus time t at uniaxial extension of type-I fluid **A** and type-II fluid **B** with the strain rates $\dot{} = 0.1$, 0.5, 1.0, 2.0, 5.0, 10.0 and 30.0 s^{-1}, from bottom to top, respectively. *Solid lines*: $= 1.0$. *Dotted lines*: $= 10.0$

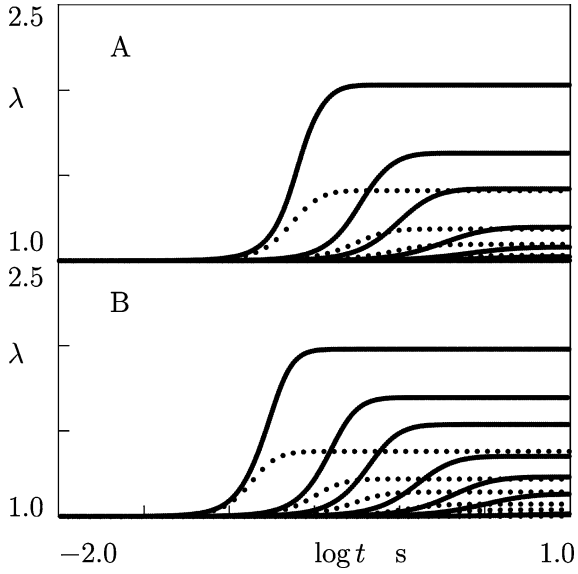

Fig. 2 The dimensionless parameter λ versus time t at uniaxial extension of type-I fluid **A** and type-II fluid **B** with the strain rates $\dot{}$ = 0.1, 0.5, 1.0, 2.0, 5.0, 10.0 and 30.0 s^{-1}, from bottom to top, respectively. *Solid lines*: = 1.0. *Dotted lines*: = 10.0

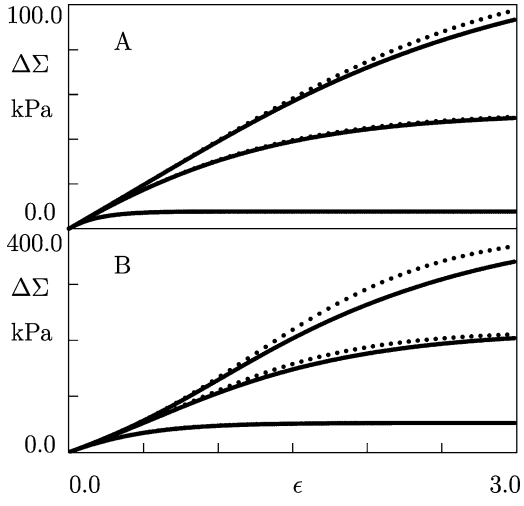

Fig. 3 The stress difference versus the Hencky strain at uniaxial extension of type-I fluid **A** and type-II fluid **B** with the strain rates $\dot{}$ = 0.1, 0.5 and 1.0 s^{-1}, from bottom to top, respectively. *Solid lines*: = 1.0. *Dotted lines*: = 10.0

The dimensionless ratio λ is plotted versus time in Fig. 2. At all strain rates under consideration, λ monotonically increases with t and reaches its steady-state value within the experimental time-scale. The steady values of λ strongly increase with strain rate $\dot{}$ and noticeably decrease with .

The stress difference is plotted versus the Hencky strain in Fig. 3. The quantity monotonically increases with strain . The growth is relatively weak at small strain rates and it becomes stronger with an increase in $\dot{}$. An increase in results in the growth of the stress difference (insignificant at small $\dot{}$, but substantial at large strain rates).

The following conclusions may be drawn from the results depicted in Figs. 1 to 3:

1. The ratio of elastic moduli affects the elongational viscosity rather weakly, but its influence on the average elongation ratio of chains is significant.
2. The stress difference increases with strain for both types of fluids, but the growth is more pronounced for type-II polymer fluid.
3. The shapes of the curves depicted in Figs. 1 and 3 coincide qualitatively with appropriate experimental dependencies for polymer melts [33].

5.2 Stress relaxation

Our aim now is to study the evolution of stresses in a standard relaxation test with

$$k(t) = \begin{cases} 1, & t \quad 0, \\ k_0, & t \geq 0, \end{cases} \tag{68}$$

where $k_0 \quad 0$ is a given elongation ratio. It follows from Eqs. (57) and (68) that the function (t) satisfies the equation

$$\frac{d}{dt} = \frac{\mu}{3\ \frac{0}{n}} \frac{k_0^3 - \ ^3}{k_0} \ ^2. \tag{69}$$

To develop an initial condition for this equation, we integrate Eq. (57) along a small interval of time within which the function $k(t)$ changes from 1 to k_0. In this interval, the second term on the right-hand side of Eq. (57) may be neglected, which implies that

$$\frac{d}{dk} = \quad \overline{k}.$$

Integration of this equation with the condition $(k)|_{k=1} = 1$ results in

$$(0) = k_0 . \tag{70}$$

Introducing the notation $(t) = k_0 z(t)$, we present Eqs. (69) and (70) in the form

$$\frac{dz}{dt} = \frac{\mu}{3\ \frac{0}{n}} \frac{1 - z^3}{z} \ ^2, \quad z(0) = k_0^{-(1-\ )}. \tag{71}$$

According to Eq. (54), the function (t) obeys the equation

$$\frac{d}{dt} = -\frac{\mu}{s} \left[\left(\frac{1}{3} \ ^2 \left(\frac{1}{z^2} + 2z \right) - 1 \right) + \quad (1 - \ ^{-6} \ ^{-3}) \right] , \qquad (0) = 1. \tag{72}$$

It follows from Eq. (52) that the stress difference is given by

$$= \mu(1 - \ ) \ ^2 \frac{1 - z^3}{z^2}. \tag{73}$$

To assess the relaxation kinetics, we solve Eqs. (71) and (72) numerically and calculate from Eq. (73). Integration is performed by the Runge–Kutta method with the time step $t = 1.0 \cdot 10^{-4}$ s and the elongation ratios $k_0 = 2.0$, 3.0, 4.0 and 5.0. We use the same material parameters as those employed in the analysis of transient elongational viscosity for type-I fluid (Table 1). Numerical simulation is carried out for two values of the zero strain rate viscosity $\frac{0}{n} = 10.0$ and $\frac{0}{n} = 40.0$ kPa·s.

The stress difference is plotted versus time in Fig. 4A. This figure reveals the following features of the relaxation process: (i) the stress monotonically decreases with time, and the reduction in stress is strongly non-exponential, (ii) the influence of the elongation ratio k_0 on the stress difference is observed at the initial interval of relaxation only, and (iii) an increase in viscosity $\frac{0}{n}$ results in the shift of the relaxation curves to larger times.

To evaluate the average elongation of strands, we calculate λ from Eq. (40) and plot the function $\lambda(t)$ in Fig. 4B. This figure shows that changes in the ratio λ are quite small (less than 0.02) for all elongations k_0 under investigation. The function $\lambda(t)$ increases at small times, reaches its ultimate value at the end of the initial period of relaxation, and decreases to its equilibrium value $\lambda = 1$ within the experimental time-scale.

According to Fig. 4, changes in the coefficient with time may be disregarded, which implies that Eqs. (71) and (73) are simplified

$$\begin{aligned} \frac{dz}{dt} &= \frac{\mu}{3\ \frac{0}{n}} \frac{1 - z^3}{z}, \quad z(0) = k_0^{-(1-\ )}, \\ &= \mu(1 - \ ) \frac{1 - z^3}{z^2}. \end{aligned} \tag{74}$$

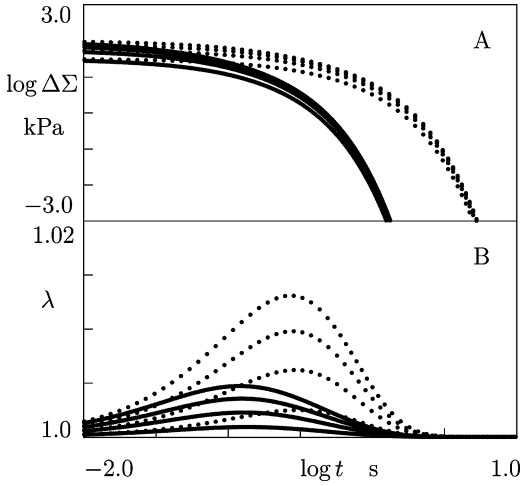

Fig. 4 The stress difference **A** and the dimensionless ratio λ **B** versus time t in relaxation tests on type-I fluid with the elongation ratios $k = 2.0, 3.0, 4.0$ and 5.0, from bottom to top, respectively. *Solid lines*: $\overset{0}{n} = 10.0$. *Dotted lines*: $\overset{0}{n} = 40.0$ kPas·

Differential Eq. (74) is integrated explicitly,

$$\frac{1}{2}\ln\frac{1-z^3}{(1-z)^3} - \sqrt{3}\arctan\frac{1+2z}{\sqrt{3}} = \frac{1}{2}\ln\frac{1-k_0^{-3(1-\ )}}{\left(1-k_0^{-(1-\ )}\right)^3} - \sqrt{3}\arctan\frac{1+2k_0^{-(1-\ )}}{\sqrt{3}} + \frac{\mu}{\overset{0}{n}}t.$$

After determining the function $z(t)$, the stress difference (t) is calculated from the second equality in Eq. (74). This analytical solution may be convenient for the study of scaling behavior of relaxation curves at various intervals of time.

6 Simple shear

We proceed with the analysis of shear flow of polymer fluids. Simple shear of an infinite layer is described by the equations

$$x_1 = X_1, \quad x_2 = X_2 + k(t)X_1, \quad x_3 = X_3, \tag{75}$$

where $\{X_i\}$ are Cartesian coordinates in the initial (stress-free) state, $\{x_i\}$ are Cartesian coordinates in the deformed state, and $k(t)$ is shear. Sliding of junctions with respect to their reference positions is treated as a superposition of simple shear and three-dimensional extension

$$_1 = \ _1(t)X_1, \quad _2 = \ _2(t)X_2 + \ (t)X_1, \quad _3 = \ _3(t)X_3, \tag{76}$$

where $\{\ _i\}$ are Cartesian coordinates in the intermediate state that describes the sliding process, and (t) and $_i(t)$ are functions to be found.

According to Eqs. (75) and (76), the deformation gradients $\mathbf{F}$ and $\mathbf{F}_n$ read

$$\mathbf{F} = \mathbf{I} + k\mathbf{e}_1\mathbf{e}_2, \quad \mathbf{F}_n = \ _1\mathbf{e}_1\mathbf{e}_1 + \ _2\mathbf{e}_2\mathbf{e}_2 + \ _3\mathbf{e}_3\mathbf{e}_3 + \ \mathbf{e}_1\mathbf{e}_2, \tag{77}$$

where $\mathbf{e}_i$ are base vectors of the coordinate frame $\{X_i\}$. Substitution of expressions (77) into Eq. (4) results in

$$\mathbf{F}_e = \frac{1}{\lambda}(p_1\mathbf{e}_1\mathbf{e}_1 + p_2\mathbf{e}_2\mathbf{e}_2 + p_3\mathbf{e}_3\mathbf{e}_3 + \ \mathbf{e}_1\mathbf{e}_2), \tag{78}$$

where

$$p_1 = \ _2\ _3, \quad p_2 = \ _1\ _3, \quad p_3 = \ _1\ _2, \quad \ = \ _3(\ _1k - \ ).$$

Combining Eqs. (8), (38) and (78), we find that

$$\mathbf{b}_e = \big(p_1^2 + \ \ ^2\big)\mathbf{e}_1\mathbf{e}_1 + p_2 \ \ (\mathbf{e}_1\mathbf{e}_2 + \mathbf{e}_2\mathbf{e}_1) + p_2^2\mathbf{e}_2\mathbf{e}_2 + p_3^2\mathbf{e}_3\mathbf{e}_3. \tag{79}$$

The first invariant of the tensor $\mathbf{b}_e$ is calculated as

$$j_{e1} = p_1^2 + p_2^2 + p_3^2 + \ \ ^2.$$

According to Eq. (75) the velocity gradient $\mathbf{L}$ and the rate-of-strain tensor $\mathbf{D}$ are given by

$$\mathbf{L} = \dot{k}\mathbf{e}_1\mathbf{e}_2, \quad \mathbf{D} = \frac{\dot{k}}{2}(\mathbf{e}_1\mathbf{e}_2 + \mathbf{e}_2\mathbf{e}_1), \tag{80}$$

where $\dot{k} = dk/dt$. It follows from Eqs. (44) and (80) that the strain-rate intensity reads

$$D_i = |\dot{k}|. \tag{81}$$

Substitution of expressions (79) and (80) into Eq. (39) results in the differential equations

$$\begin{aligned}
\frac{dp_1}{dt} &= -\frac{\mu}{6\ _n}p_1\ \ ^2\big(2p_1^2 - p_2^2 - p_3^2 - \ \ ^2\big),\\
\frac{dp_2}{dt} &= -\frac{\mu}{6\ _n}p_2\ \ ^2\big(-p_1^2 + 2p_2^2 - p_3^2 + 2\ \ ^2\big),\\
\frac{dp_3}{dt} &= -\frac{\mu}{6\ _n}p_3\ \ ^2\big(-p_1^2 - p_2^2 + 2p_3^2 - \ \ ^2\big),\\
\frac{d}{dt} &= (1 - \ \ )p_2\frac{dk}{dt} - \frac{\mu}{6\ _n}\ \ ^2\big(5p_1^2 + 2p_2^2 - p_3^2 + 2\ \ ^2\big).
\end{aligned} \tag{82}$$

Combining Eqs. (42) and (79), we find that

$$\frac{d}{dt} = -\frac{\mu}{\ _s}\left[\left(\frac{^2}{3}\big(p_1^2 + p_2^2 + p_3^2 + \ \ ^2\big) - 1\right) + \ \ (1 - \ \ ^{-6}\ ^{-3})\right] \ . \tag{83}$$

Substitution of expression (79) into Eq. (43) implies that

$$= \ \ _{11}\mathbf{e}_1\mathbf{e}_1 + \ \ _{22}\mathbf{e}_2\mathbf{e}_2 + \ \ _{33}\mathbf{e}_3\mathbf{e}_3 + \ \ _{12}(\mathbf{e}_1\mathbf{e}_2 + \mathbf{e}_2\mathbf{e}_1),$$

where

$$\begin{aligned}
_{11} &= -P + \mu(1 - \ \ )\big(p_1^2 + \ \ ^2\big)\ \ ^2,\\
_{22} &= -P + \mu(1 - \ \ )p_2^2\ \ ^2,\\
_{33} &= -P + \mu(1 - \ \ )p_3^2\ \ ^2,\\
_{12} &= \mu(1 - \ \ )p_2\ \ \ ^2.
\end{aligned} \tag{84}$$

It follows from these formulas that the first normal stress difference $N_1 = \ \ _{11} - \ \ _{22}$ and the second normal stress difference $N_2 = \ \ _{22} - \ \ _{33}$ read

$$N_1 = \mu(1 - \ \ )\big(p_1^2 - p_2^2 + \ \ ^2\big)\ \ ^2, \quad N_2 = \mu(1 - \ \ )\big(p_2^2 - p_3^2\big)\ \ ^2. \tag{85}$$

Equations (82) to (85) determine the shear stress $\ \ = \ \ _{12}$ and the normal stress differences N_1 and N_2 for an arbitrary shear program $k(t)$. Our aim now is to analyze in detail (i) shearing with a constant strain rate $\dot{k}$, and (ii) shear oscillations with small and large amplitudes.

6.1 Deformation with a constant strain rate

We begin with the analysis of shear flow with a constant strain rate $\dot{k}$ and determine the steady shear viscosity $_s$ as a function of shear rate. For this purpose, we assume that the functions $p_m(t)$ $(m = 1, 2, 3)$, (t) and (t) tend to their limiting values p_{m0}, $_0$ and $_0$ as $t \to \infty$. Equations (82) and (83) imply that the quantities p_{m0}, $_0$ and $_0$ satisfy the equations

$$\begin{gathered}
2p_{10}^2 - p_{20}^2 - p_{30}^2 - \ {}^2_0 = 0, \\
-p_{10}^2 + 2p_{20}^2 - p_{30}^2 + 2\ {}^2_0 = 0, \\
-p_{10}^2 - p_{20}^2 + 2p_{30}^2 - \ {}^2_0 = 0, \\
\left(5p_{10}^2 + 2p_{20}^2 - p_{30}^2 + 2\ {}^2_0\right)\ {}_0\ {}^2_0 = \frac{6\ {}_n}{\mu}(1 - \ )p_{20}\dot{k}, \\
\frac{{}^2_0}{3}\left(p_{10}^2 + p_{20}^2 + p_{30}^2 + \ {}^2_0\right) = 1 - \ \left(1 - \ {}_0^{-6\ -3}\right).
\end{gathered} \tag{86}$$

Subtracting the third equality in Eq. (86) from the first one, we obtain

$$p_{30}^2 = p_{10}^2. \tag{87}$$

Substitution of expression (87) into the second equality in Eq. (86) results in

$$p_{10}^2 = p_{20}^2 + \ {}^2_0. \tag{88}$$

It follows from Eq. (82) that

$$p_{10}^2 p_{20}^2 p_{30}^2 = 1.$$

Combining this equality with expressions (87) and (88), we obtain

$$p_{20}^2 + \ {}^2_0 = \frac{1}{p_{20}}. \tag{89}$$

Substituting Eqs. (87) and (88) into the fourth and fifth equations in Eq. (86) and using Eq. (89), we find that

$${}_0\ {}^2_0 = \frac{{}_n}{\mu}(1 - \ )p_{20}^2\dot{k}, \quad \frac{{}^2_0}{1 - \ \left(1 - \ {}_0^{-6\ -3}\right)} = p_{20}. \tag{90}$$

It follows from Eq. (84) that the steady shear viscosity $_s = \ /\dot{k}$ is given by

$${}_s = \frac{\mu}{\dot{k}}(1 - \ )p_{20}\ {}_0\ {}^2_0. \tag{91}$$

For an arbitrary parameter , the steady shear viscosity is determined from Eqs. (89) to (91).

These equations are studied analytically at small $\ll 1$. It follows from the second equality in Eq. (90) that

$${}^2_0 = p_{20}. \tag{92}$$

Combining this formula with the first equality in Eq. (90), we obtain

$${}_0 = \frac{{}_n}{\mu}(1 - \ )p_{20}\dot{k}. \tag{93}$$

It follows from Eqs. (89) and (91) to (93) that

$${}_s = \ {}_n(1 - \ )^2 p_{20}^3, \tag{94}$$

where p_{20} satisfies the algebraic equation

$$p_{20}^2 + \left[\frac{{}_n}{\mu}(1 - \ )\dot{k}\right]^2 p_{20}^2 = \frac{1}{p_{20}}.$$

The solution of this equation reads

$$p_{20} = \left\{1 + \left[\frac{n}{\mu}(1 - \quad)\dot{k}\right]^2\right\}^{-\frac{1}{3}}.$$

Combining this expression with Eq. (94), we arrive at the formula for the steady shear viscosity

$$_s = \ _n(1 - \quad)^2 \left\{1 + \left[\frac{n}{\mu}(1 - \quad)\dot{k}\right]^2\right\}^{-1}. \tag{95}$$

Comparison of Eqs. (65) and (95) implies that at small strain rates, when the terms in the square brackets in Eq. (95) may be disregarded, the Trouton ratio

$$\mathrm{Tr} = \frac{e}{s}$$

equals 3, in accord with numerous observations. Another conclusion that may be drawn from Eq. (95) is that at relatively large shear rates, the steady shear viscosity $_s$ decreases with $\dot{k}$ independently of whether $_n$ (and, as a result, the elongational viscosity $_e$) increases or decreases with strain rate.

To find the steady first and second normal stress differences, we substitute expressions (87) and (88) into Eq. (85) and obtain

$$N_1 = 2\mu(1 - \quad) \ \frac{2}{0} \ \frac{2}{0}, \quad N_2 = -\mu(1 - \quad) \ \frac{2}{0} \ \frac{2}{0}. \tag{96}$$

It follows from these equations that for arbitrary shear rate $\dot{k}$ and dimensionless ratio ,

$$\frac{N_2}{N_1} = -\frac{1}{2}. \tag{97}$$

Substitution of expressions (91) and (93) into the first equality in Eq. (96) implies that at $\ll 1$,

$$N_1 = \frac{2}{\mu} \ \frac{2}{n}(1 - \quad)^3\dot{k}^2 \left\{1 + \left[\frac{n}{\mu}(1 - \quad)\dot{k}\right]^2\right\}^{-1}. \tag{98}$$

The characteristic time for steady shear flow is given by $_n = N_1/(2 \ \dot{k})$. Combining this formula with Eqs. (95) and (98), we find that

$$_n = \frac{n}{\mu}(1 - \quad). \tag{99}$$

To evaluate the characteristic time at small strain rates $\frac{0}{n}$ (this quantity determines the Weissenberg number), the viscosity $_n$ in Eq. (99) should be replaced by $\frac{0}{n}$. For the material parameters of type-I fluid listed in Table 1, this procedure results in $\frac{0}{n} = 0.05$ s at $\frac{0}{n} = 10.0$ and $\frac{0}{n} = 0.2$ s at $\frac{0}{n} = 40.0$ kPa·s.

To assess transient stresses in shear flows with constant strain rates at an arbitrary , we integrate Eqs. (82) and (83) numerically with the initial conditions

$$p_1(0) = 1, \quad p_2(0) = 1, \quad p_3(0) = 1, \quad (0) = 0, \quad (0) = 1.$$

Integration is performed by the Runge–Kutta method with the time step $t = 1.0 \cdot 10^{-4}$ s at the shear rates $\dot{k} = 0.5$, 1.0, 2.0, 5.0 and 10.0 s^{-1}. We use the same material constants that were employed in the analysis of transient extensional flows of type-I and type-II polymer fluids (Table 1). The shear stress and the normal stress differences N_1 and N_2 are determined by Eqs. (84) and (85). The results of numerical simulation are presented in Figs. 5 and 6, which demonstrate that the same qualitative conclusions may be drawn for type-I and type-II polymers.

At small strain rates, the shear stress monotonically grows to its steady-state value. At relatively large strain rates, increases with time, reaches its maximum, and decreases afterwards approaching its steady-state value (stress overshoot). The intensity of stress overshoot increases with shear rate, whereas the instant when the shear stress reaches its ultimate value decreases with $\dot{k}$.

At relatively small shear rates, the first normal stress difference N_1 monotonically increases with time and approaches its steady-state value. At sufficiently large strain rates, N_1 demonstrates the stress overshoot similar to that for the shear stress. However, the strain rates $\dot{k}$, at which the overshoot of the first normal

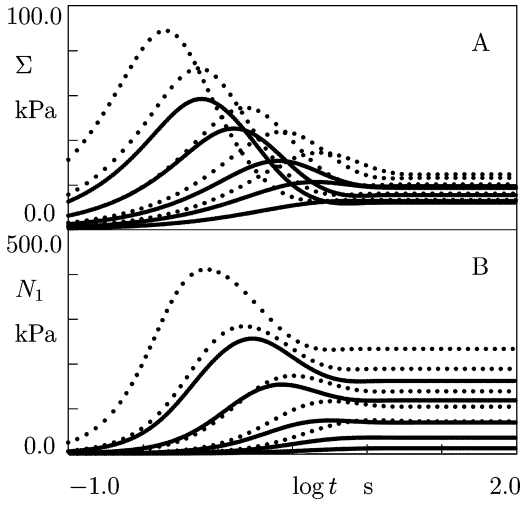

Fig. 5 The shear stress **A** and the first normal stress difference N_1 **B** versus time t in shear tests with the strain rates $\dot{k} = 0.5$, 1.0, 2.0, 5.0 and 10.0 s^{-1}, from bottom to top, respectively. *Solid lines*: type-I fluid. *Dotted lines*: type-II fluid

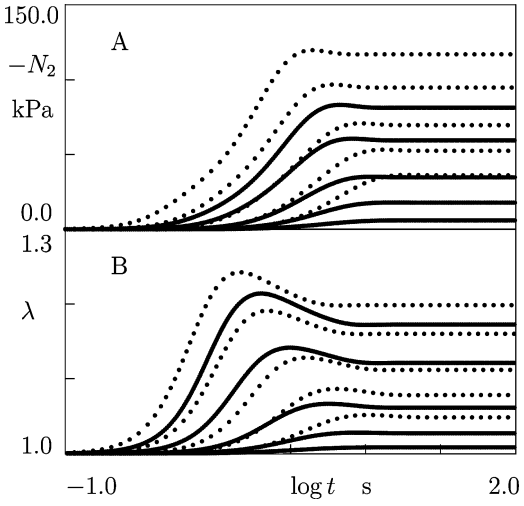

Fig. 6 The second normal stress difference N_2 **A** and the dimensionless ratio λ **B** versus time t in shear tests with the strain rates $\dot{k} = 0.5$, 1.0, 2.0, 5.0 and 10.0 s^{-1}, from bottom to top, respectively. *Solid lines*: type-I fluid. *Dotted lines*: type-II fluid

stress difference becomes substantial exceed those at which the overshoot of the shear stress is first observed. Another feature of the graphs depicted in Fig. 5 is that the overshoot of N_1 occurs at times that are noticeably higher than the instants when the shear stress reaches its maximum.

The curves depicted in Fig. 5 are qualitatively similar to experimental data on the transient shear stress and the first normal stress difference observed in numerous experiments on polymer melts and solutions. The dependence of the second normal stress difference on time (which cannot be measured directly in conventional tests) is plotted in Fig 6A. According to this figure, at relatively large shear rates, stress overshoot can be observed for N_2 as well. However, the intensity of overshoot for N_2 is substantially lower than that for N_1, and the time at which the overshoot occurs is noticeably larger than the instant when the first normal stress difference reaches its maximum. This conclusion distinguishes the present model from that developed in [10], where it was found that the stress overshoot for N_2 occurred earlier than that for N_1, and its intensity was comparable with the intensity of stress overshoot for shear stress.

The elongation ratio λ is plotted versus time in Fig. 6B. At small shear rates, λ monotonically increases and approaches its ultimate value. At relatively large strain rates, λ demonstrates an overshoot similar to the overshoot for the first normal stress difference. Comparison of Figs. 2 and 6B reveals that the growth of the elongation ratio λ at uniaxial extension is stronger than that at simple shear with the same strain rate. This

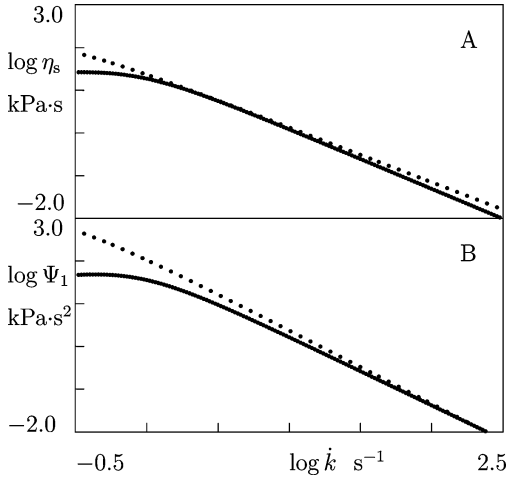

Fig. 7 The steady shear viscosity $_s$ **A** and the first normal stress coefficient $_1$ **B** versus shear rate $\dot{k}$. *Solid lines*: type-I fluid. *Dotted lines*: type-II fluid

conclusion is in agreement with the conventional standpoint that elongation of strands in extensional flows substantially exceeds that in shear flows.

Figures 5 and 6 demonstrate that stress overshoots in , N_1 and N_2 are more pronounced and occur at earlier times for type-II fluid than for type-I fluid. However, no qualitative difference may be observed between the results of numerical simulation with Eqs. (45) and (46).

Figure 5 does not reveal how the steady shear viscosity and the first normal stress difference change with strain rate. To analyze these dependencies, we present appropriate data in Fig. 7, where the steady shear viscosity $_e$ and the steady first normal stress coefficient $_1 = N_1/\dot{k}^2$ are depicted as functions of shear rate $\dot{k}$. Three conclusions may be drawn from the results depicted in Fig. 7: (i) at strain rates employed in conventional shear tests, the steady shear viscosity $_s$ and the steady first normal stress coefficient $_1$ decrease with $\dot{k}$ following the scaling laws $_s \sim \dot{k}^{-a}$ and $_1 \sim \dot{k}^{-a}$ with the exponents a = 1.2 to 1.3 and a = 1.6 to 1.7, which are rather close to the values a = 0.9 and a = 1.5 observed in rheological tests on entangled polymer solutions [34, 35], (ii) the same dependence $_n(D_i)$ in Eq. (45) implies the growth of the steady elongational viscosity with strain rate in uniaxial extensional flow and the reduction of the steady shear viscosity with strain rate in shear flow, and (iii) the decrease in steady shear viscosity and steady first normal stress coefficient with shear rate is practically independent of the effect of strain-rate intensity on viscosity $_n$ in Eqs. (45) and (46).

It is worth noting that the values of a located in the interval from 1.2 to 1.3 are obtained for hypothetical fluids with the parameters listed in Table 1. Approximations of observations on polymer melts result in slightly different values of material parameters, which ensure the stability of shear flows. As the purpose of the present study is to demonstrate the main features of the constitutive equations, not to fit concrete sets of experimental data, we do not dwell on this issue.

For the sake of brevity, we do not present results of simulation with various values of . Our numerical analysis shows that an increase in results in the growth of stresses. This growth is, however, relatively weak: when increases by an order of magnitude, the stresses grow by 10 to 15 per cent only.

An important conclusion that may be drawn from Figs. 1 and 5 is that observations in conventional extensional and shear tests do not allow us to distinguish between Eqs. (45) and (46) for the viscosity $_n$ of sliding of junctions. Strain thickening in extensional flow and stress overshoot in shear flow are revealed within the experimental time-scale for both phenomenological equations. To show which relation describes experimental data more adequately, we proceed with the study of shear oscillations with large amplitudes.

6.2 Oscillations with large amplitudes

The time-dependent response of a polymer fluid is analyzed numerically in shear oscillatory tests with the deformation program

$$k(t) = k_0 \sin(2\pi f t), \tag{100}$$

where k_0 is the amplitude, f is the frequency of oscillations, and k_0 is of order of unity.

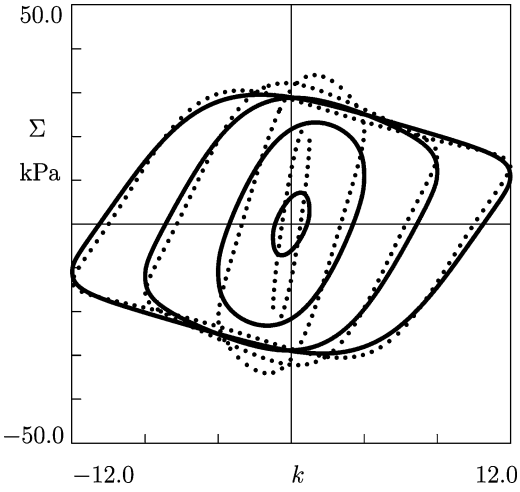

Fig. 8 The shear stress versus shear k in oscillatory tests with the frequency $f = 0.05$ Hz and the amplitudes $k_0 = 1.0$, 4.0, 8.0 and 12.0. *Solid lines*: type-I fluid. *Dotted lines*: type-II fluid

Experimental data in dynamic tests with large amplitudes are conventionally obtained after a steady regime of oscillations is established. They are presented in two forms: (i) the shear stress as a function of shear k (the Lissajou figures), and (ii) the shear stress as a function of shear rate $\dot{k}$. Experimental curves demonstrate the following features: (i) at relatively small amplitudes (when $k_0 \leq 1$), the curves (k) and $(\dot{k})$ are similar to ellipses, (ii) when k_0 exceeds unity, the ellipses are deformed, and two different regimes of oscillations are observed. The first regime corresponds to box-like dependencies (k), when the shape of the curve (k) becomes analogous to a square with smooth edges [36]. The other regime corresponds to S-shaped dependencies $(\dot{k})$, when the shape of the curve $(\dot{k})$ is similar to letter S with different curvatures of the upper (loading) and lower (unloading) parts and rather sharp edges [37].

Our aim now is to show that the box-like Lissajou figures may be observed in shear oscillations with large amplitudes for both types of polymer fluids, whereas the S-shaped dependence $(\dot{k})$ is revealed for type-II fluid only, i.e., for a polymer fluid whose viscosity $_n$ decreases with strain rate.

We begin with the analysis of Lissajou figures. For this purpose, we integrate Eqs. (82) and (83) numerically by the Runge–Kutta method with the time-step $t = 1.0 \cdot 10^{-4}$ s. We set $f = 0.05$ Hz and calculate the shear stress from Eq. (84) at $k_0 = 1.0$, 4.0, 8.0 and 12.0. Numerical simulation is carried out in the interval of time from zero to 1000 s. Within this interval, steady oscillations are established for all amplitudes k_0 under investigation. The dependencies (k) corresponding to the last cycle of oscillations are presented in Fig. 8. This figure shows that at $k_0 = 1.0$, the shape of the curves (k) is elliptic. With an increase in k_0, the ellipse is transformed into an oval ($k_0 = 4.0$), and it becomes similar to a square with smooth edges at $k_0 = 8.0$ and 12.0. It is interesting to note that at relatively small amplitudes of oscillations ($k_0 = 1.0$ and 4.0), the difference between the curves (k) for type-I and type-II polymers is quite pronounced: the stress amplitude for type-II fluid strongly exceeds that for type-I fluid. With an increase in amplitude of oscillations, the difference between appropriate curves is reduced and it practically disappears at $k_0 = 12.0$.

The dimensionless ratio λ is plotted versus shear k is Fig. 9. The curves $\lambda(k)$ have similar shapes and sizes for both types of fluids. It is worth noting that the period of oscillations of λ equals half of the period of shear oscillations. This phenomenon is not observed in networks where slippage of strands along entanglements is prevented, and it is associated with stretching of chains. The curves $\lambda(k)$ demonstrate a butterfly pattern for both types of polymer fluids. The average (over a period) value of chain stretching λ increases with amplitude k_0. The growth of the average ratio λ with k_0 is more pronounced for type-II fluid.

Another important conclusion of the numerical simulation is that the evolution of shapes of the Lissajou figures observed in Fig. 9 is mainly induced by slippage of chains with respect to entanglements. Although a rigorous proof of this statement is rather complicated due to the nonlinearity of governing equations, this result can be easily obtained from the comparison of the characteristic time $_s = {}_s/\mu$ for stretching of chains with the characteristic time for steady shear flow ^0_n given by Eq. (99). It follows from Table 1 that the parameter $_s$ equals 3.8 s and 6.0 s for type-I and type-II fluids, respectively, which implies that strong changes in the shape

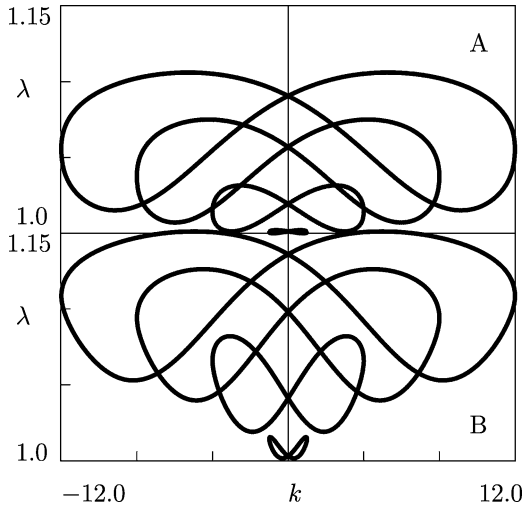

Fig. 9 The dimensionless ratio λ versus shear k in oscillatory tests with the frequency $f = 0.05$ Hz and the amplitudes $k_0 = 1.0$, 4.0, 8.0 and 12.0, from bottom to top, respectively. **A** type-I fluid; **B** type-II fluid

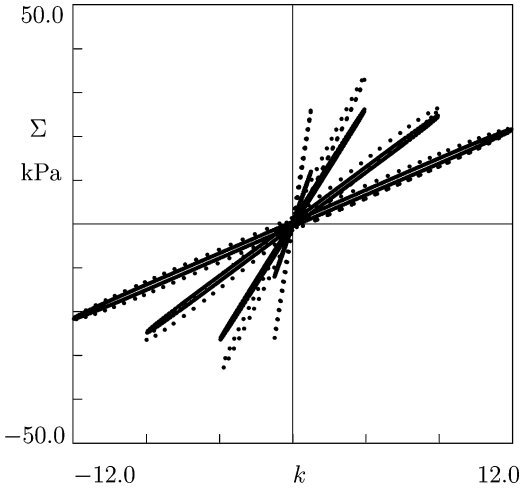

Fig. 10 The shear stress versus shear k in oscillatory tests with the frequency $f = 10.0$ Hz and the amplitudes $k_0 = 1.0$, 4.0, 8.0 and 12.0. *Solid lines*: type-I fluid. *Dotted lines*: type-II fluid

of the curves (k) induced by stretching of chains may be expected at the frequencies $f_s = 1/(2\pi\ _s)$ of order of 0.03 to 0.04 Hz (which are quite close to the frequency $f = 0.05$ Hz employed in the numerical analysis). On the other hand, for non-affine networks without slippage of chains, a noticeable dependence of the curves (k) on amplitude of oscillations should be expected at the frequency $f_n = 1/(2\pi\ {}^0_n)$. Equation (99) together with Table 1 implies that for type-I fluid, f_n is about 3 Hz. Figure 10 demonstrates that at this frequency of oscillations, the curves (k) remain elliptic at all amplitudes k_0, whereas an increase in k_0 causes mainly clock-wise rotation of the ellipses with respect to coordinate axes.

To reveal the difference between the response of type-I and type-II fluids in shear oscillatory tests, we perform numerical integration of Eqs. (82), (83) and (100) with the frequencies $f = 0.08$ Hz (type-I polymer) and $f = 0.003$ Hz (type-II polymer), calculate the shear stress from Eq. (84), and plot as a function of strain rate $\dot{k}$ in Figs. 11 and 12, respectively. Figure 11 demonstrates that for type-I fluid, the curve $(\dot{k})$ is elliptic when the amplitude k_0 equals unity. With an increase in k_0, the ellipse is transformed into an oval ($k_0 = 5.0$), and, at higher amplitudes $k_0 = 10.0$ and 15.0, it adopts a rhomboidal shape with relatively sharp edges directed up. The large axis of symmetry of the curves $(\dot{k})$ strongly rotates clock-wise with the growth of amplitude of oscillations. According to Fig. 12, for type-II fluid, the curve $(\dot{k})$ is elliptical at $k_0 = 1.0$. With the growth of k_0, this curve accepts the S-shaped form with very sharp edges, while the large axis of symmetry remains independent of amplitude.

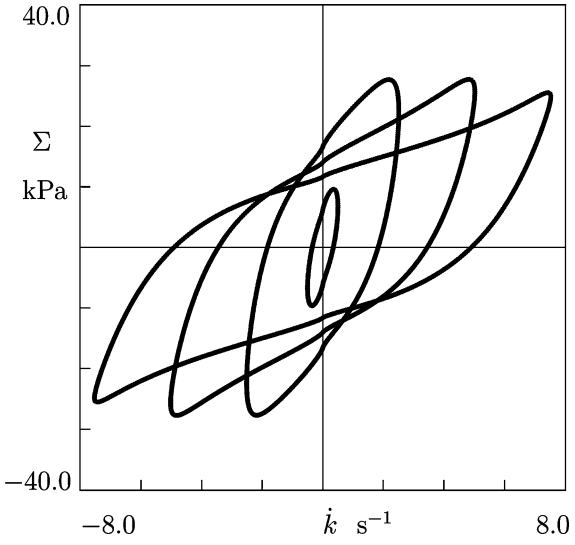

Fig. 11 The shear stress versus shear rate $\dot{k}$ in oscillatory tests on type-I fluid with the frequency $f = 0.08$ Hz and the amplitudes $k_0 = 1.0$, 5.0, 10.0 and 15.0, from the inner to the outer curve, respectively

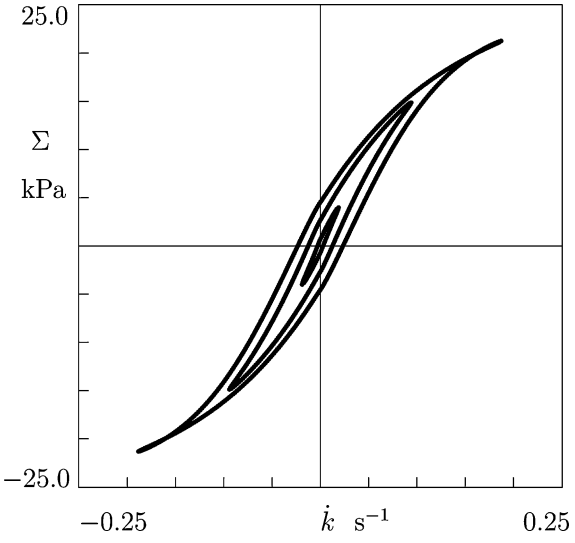

Fig. 12 The shear stress versus shear rate $\dot{k}$ in oscillatory tests on type-II fluid with the frequency $f = 0.003$ Hz and the amplitudes $k_0 = 1.0$, 5.0 and 10.0, from the inner to the outer curve, respectively

The ratio λ that characterizes slippage of chains with respect to entanglements is plotted versus shear rate $\dot{k}$ in Fig. 13. For type-I fluid, the curves $\lambda(\dot{k})$ demonstrate a butterfly-like shape. The average value of λ strongly grows with amplitude of oscillations. For type-II fluid, the curves $\lambda(\dot{k})$ show a rabbit-ears shape, where length of the "ears" increases with k_0. For both types of fluids, the period of oscillations for λ equals half of the period of shear oscillations.

6.3 Oscillations with small amplitudes

Our aim now is to analyze shear oscillations with small strains, when the governing equations may be linearized. For this purpose, we set

$$p_m = 1 + \quad p_m + \ldots, \qquad = \qquad + \ldots, \qquad = 1 + \qquad + \cdots \quad (m = 1, 2, 3), \tag{101}$$

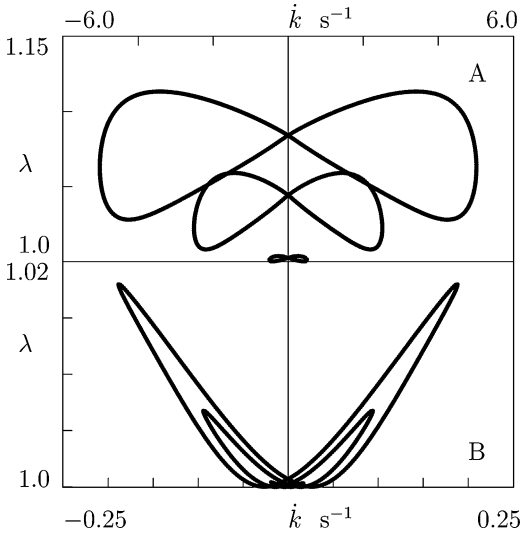

Fig. 13 The dimensionless ratio λ versus strain rate $\dot{k}$ in shear oscillatory tests with the amplitudes $k_0 = 1.0$, 5.0 and 10.0, from bottom to top, respectively. **A** type-I fluid, $f = 0.08$ Hz. **B** type-II fluid, $f = 0.003$ Hz

substitute expressions (101) into governing equations, and neglect terms of the second order of smallness compared to $|\ \ p_m|$, $|\ \ \ |$ and $|\ \ \ |$. It follows from Eqs. (82), (83) and (101) that

$$\frac{d\ \ p_1}{dt} = -\frac{\mu}{3\ \ _n^0}(2\ \ p_1 - \ \ p_2 - \ \ p_3),$$

$$\frac{d\ \ p_2}{dt} = -\frac{\mu}{3\ \ _n^0}(-\ \ p_1 + 2\ \ p_2 - \ \ p_3), \tag{102}$$

$$\frac{d\ \ p_3}{dt} = -\frac{\mu}{3\ \ _n^0}(-\ \ p_1 - \ \ p_2 + 2\ \ p_3),$$

$$\frac{d\ \ }{dt} = -\frac{\mu}{\ \ _s}\left[(2+3\ \ (2\ \ +1))\ \ \ \ + \frac{2}{3}(\ \ p_1 + \ \ p_2 + \ \ p_3)\right], \tag{103}$$

$$\frac{d\ \ }{dt} = (1 - \ \ )\frac{dk}{dt} - \frac{\mu}{\ \ _n^0}\ \ \ . \tag{104}$$

Summing Eq. (102), we find that

$$\frac{d}{dt}(\ \ p_1 + \ \ p_2 + \ \ p_3) = 0.$$

As the expression in parentheses equals zero at the initial instant $t = 0$, it vanishes at any $t \geq 0$. This conclusion together with Eq. (103) implies that

$$\frac{d\ \ }{dt} = -\frac{\mu}{\ \ _s}(2+3\ \ (2\ \ +1))\ \ \ \ .$$

It follows from this equation and the initial condition $\ \ (0) = 0$ that $\ \ (t) = 0$ at any $t \geq 0$. This means that stretching of strands in a non-affine network is a second-order effect, which is not observed at small strains.

Substitution of expressions (101) into Eq. (84) implies that with the required level of accuracy,

$$= \mu(1 - \ \ )\ \ \ \ . \tag{105}$$

Equations (104) and (105) result in the linear differential equation (the Maxwell model) for the shear stress

$$\frac{d\ \ }{dt} + \frac{\mu}{\ \ _n^0}\ \ = \mu(1 - \ \ )^2\frac{dk}{dt}. \tag{106}$$

To calculate the storage and loss moduli, we set $k(t) = k_0 \exp(\iota \ t)$, where k_0 is a small amplitude, is a radial frequency, and $\iota = \sqrt{-1}$. We search a solution of Eq. (106) in the form $(t) = G^*( )k_0 \exp(\iota \ t)$, where G^* is the complex modulus. Substitution of these expressions into Eq. (106) results in

$$G^*( ) = \mu(1 -)^2 \iota \left(\frac{\mu}{\frac{0}{n}} + \iota \right)^{-1}.$$

Bearing in mind that $G^* = G' + \iota G''$, where G' is the storage modulus, and G'' is the loss modulus, we find that

$$G'( ) = \mu(1 -)^2 \ ^2 \left[\left(\frac{\mu}{\frac{0}{n}} \right)^2 + \ ^2 \right]^{-1}, \quad G''( ) = \mu(1 -)^2 \frac{\mu}{\frac{0}{n}} \left[\left(\frac{\mu}{\frac{0}{n}} \right)^2 + \ ^2 \right]^{-1}. \tag{107}$$

It follows from Eq. (107) that at large frequencies, when $\to \infty$, the storage modulus tends to a constant, whereas the loss modulus vanishes,

$$G'(\infty) = \mu(1 -)^2, \quad G''(\infty) = 0. \tag{108}$$

Formulas (108) for the storage and loss moduli at high-frequency oscillations have been found at small strains. Our aim now is to modify Eq. (108) for high-frequency oscillations with a finite amplitude k_0.

6.4 High-frequency oscillations with large amplitudes

For this purpose, an averaging method is applied to Eqs. (82) and (83), which are presented in the form

$$\begin{aligned}
\frac{dp_1}{dt'} &= - \ p_1 \ ^2\big(2p_1^2 - p_2^2 - p_3^2 - (\ _1 + \ _2)^2\big), \\
\frac{dp_2}{dt'} &= - \ p_2 \ ^2\big(- p_1^2 + 2p_2^2 - p_3^2 + 2(\ _1 + \ _2)^2\big), \\
\frac{dp_3}{dt'} &= - \ p_3 \ ^2\big(- p_1^2 - p_2^2 + 2p_3^2 - (\ _1 + \ _2)^2\big), \\
\frac{d \ _2}{dt'} &= - \ (\ _1 + \ _2) \ ^2\big(5p_1^2 + 2p_2^2 - p_3^2 + 2(\ _1 + \ _2)^2\big).
\end{aligned} \tag{109}$$

$$\frac{d}{dt'} = -M \left[\left(\frac{2}{3}\big(p_1^2 + p_2^2 + p_3^2 + (\ _1 + \ _2)^2\big) - 1 \right) + \ (1 - \ ^{-6} \ ^{-3}) \right],$$

$$\frac{d \ _1}{dt'} = (1 - \ )p_2 k_0 \cos t'. \tag{110}$$

To deduce Eqs. (109) and (110), we employed Eq. (100) with $= 2\pi f$, set

$$= \ _1 + \ _2, \tag{111}$$

where $_1$ is a "fast" variable, and $_2$ is a "slow" variable, introduce the dimensionless time

$$t' = \ t,$$

and assume that

$$= \frac{\mu}{6 \ _n}$$

is a small parameter. To simplify the analysis, we replace the function $6 \ _n / \ _s$ by its average value M and suppose that the coefficient M is of order of unity. It should be noted that the assumption $\ll 1$ does not lead to unrealistic frequencies of oscillations. For the material parameters listed in Table 1, this condition is satisfied when ≥ 10 rad/s.

First, we find the solution of Eq. (110) for the fast variable $_1$ treating p_2 as a parameter. Taking into account the initial condition $_1(0) = 0$, we obtain

$$_1(t') = (1 - \ )k_0 p_2 \sin t'. \tag{112}$$

We now substitute expression (112) into Eq. (109) for slow variables and perform averaging of the right-hand sides over t', where the unknown p_m ($m = 1, 2, 3$), $\ _2$ and $\ $ are thought of as constants. Using the formulas

$$\frac{1}{2\pi}\int_0^{2\pi}[\ _1(t') + \ _2]dt' = \ _2, \quad \frac{1}{2\pi}\int_0^{2\pi}[\ _1(t') + \ _2]^2 dt' = \frac{1}{2}(1 - \ )^2 k_0^2 p_2^2 + \ _2^2,$$
$$\frac{1}{2\pi}\int_0^{2\pi}[\ _1(t') + \ _2]^3 dt' = \frac{3}{2}(1 - \ )^2 k_0^2 p_2^2\ _2 + \ _2^3,$$

we arrive at the differential equations

$$\begin{aligned}
\frac{dp_1}{dt'} &= -\ p_1\ ^2\left(2p_1^2 - p_2^2\left(1 + \frac{1}{2}(1 - \ )^2 k_0^2\right) - p_3^2 - \ _2^2\right),\\
\frac{dp_2}{dt'} &= -\ p_2\ ^2\left(-p_1^2 + 2p_2^2\left(1 + \frac{1}{2}(1 - \ )^2 k_0^2\right) - p_3^2 + 2\ _2^2\right),\\
\frac{dp_3}{dt'} &= -\ p_3\ ^2\left(-p_1^2 - p_2^2\left(1 + \frac{1}{2}(1 - \ )^2 k_0^2\right) + 2p_3^2 - \ _2^2\right),\\
\frac{d\ _2}{dt'} &= -\ \ ^2\left[\left(5p_1^2 + 2p_2^2 - p_3^2\right) + \left(3(1 - \ )^2 k_0^2 p_2^2 + 2\ _2^2\right)\right]\ _2,\\
\frac{d\ }{dt'} &= -M\ \left[\left(\frac{2}{3}\left(p_1^2 + p_2^2\left(1 + \frac{1}{2}(1 - \ )^2 k_0^2\right) + p_3^2 + \ _2^2\right) - 1\right) + \ (1 - \ ^{-6}\ ^{-3})\right].
\end{aligned} \tag{113}$$

To study steady oscillations, we suppose that the functions $p_m(t')$ ($m = 1, 2, 3$), $\ _2(t')$ and $\ (t')$ approach their limiting values p_{m0}, $\ _{20}$ and $\ _0$ as $t' \to \infty$. These quantities satisfy the equations

$$\begin{aligned}
2p_{10}^2 - p_{20}^2\left(1 + \frac{1}{2}(1 - \ )^2 k_0^2\right) - p_{30}^2 - \ _{20}^2 &= 0,\\
-p_{10}^2 + 2p_{20}^2\left(1 + \frac{1}{2}(1 - \ )^2 k_0^2\right) - p_{30}^2 + 2\ _{20}^2 &= 0,\\
-p_{10}^2 - p_{20}^2\left(1 + \frac{1}{2}(1 - \ )^2 k_0^2\right) + 2p_{30}^2 - \ _{20}^2 &= 0,\\
\left[\left(5p_{10}^2 + 2p_{20}^2 - p_{30}^2\right) + \left(3(1 - \ )^2 k_0^2 p_{20}^2 + 2\ _{20}^2\right)\right]\ _{20} &= 0,\\
\frac{2}{3_0}\left[p_{10}^2 + p_{20}^2\left(1 + \frac{1}{2}(1 - \ )^2 k_0^2\right) + p_{30}^2 + \ _{20}^2\right] &= 1 - \ \left(1 - \ _0^{-6}\ ^{-3}\right).
\end{aligned} \tag{114}$$

Subtracting the third equality in Eq. (114) from the first one, we obtain

$$p_{30}^2 = p_{10}^2. \tag{115}$$

Substitution of Eq. (115) into the fourth equation in Eq. (114) results in

$$\left[2\left(2p_{10}^2 + p_{20}^2\right) + \left(3(1 - \ )^2 k_0^2 p_{20}^2 + 2\ _{20}^2\right)\right]\ _{20} = 0.$$

This equation implies that

$$\ _{20} = 0. \tag{116}$$

Substitution of expressions (115) and (116) into the first equality in Eq. (114) results in

$$p_{10}^2 = p_{20}^2\left(1 + \frac{1}{2}(1 - \ )^2 k_0^2\right). \tag{117}$$

It follows from Eq. (113) that for any $t \geq 0$,

$$p_1(t')p_2(t')p_3(t') = 1.$$

Setting $t' \to \infty$ in this equality and using Eqs. (115) and (117), we find that

$$p_{20} = \left[1 + \frac{1}{2}(1 - \quad)^2 k_0^2\right]^{-\frac{1}{6}}. \tag{118}$$

The last equation in Eq. (114) together with Eqs. (115) to (118) implies that

$$\frac{2}{0}\left[1 + \frac{1}{2}(1 - \quad)^2 k_0^2\right]^{\frac{2}{3}} = 1 - \quad\left(1 - \frac{-6}{0}\quad{}^{-3}\right). \tag{119}$$

It follows from Eqs. (84), (111) and (116) that at steady shear oscillations with finite amplitudes and high frequencies

$$(t) = \mu(1 - \quad) p_{20}\ \frac{2}{0}\ {}_1(t).$$

Combining this equality with Eqs. (112) and (118) and introducing the storage shear modulus $g(k_0) = (t)/k(t)$, we find that

$$g(k_0) = G'(\infty)\ \frac{2}{0}\left[1 + \frac{1}{2}(1 - \quad)^2 k_0^2\right]^{-\frac{1}{3}}, \tag{120}$$

where $_0$ is given by Eq. (119). It is of interest to consider two limiting cases, when $\to 0$ and $\to \infty$. At $\ll 1$, the second term on the right-hand side of Eq. (119) may be neglected, which implies that

$$\frac{2}{0} = \left[1 + \frac{1}{2}(1 - \quad)^2 k_0^2\right]^{-\frac{2}{3}}$$

and

$$g(k_0) = G'(\infty)\left[1 + \frac{1}{2}(1 - \quad)^2 k_0^2\right]^{-1} \quad (\quad \ll 1). \tag{121}$$

At $\gg 1$, the solution of Eq. (119) reads $_0 = 1$, which means that

$$g(k_0) = G'(\infty)\left[1 + \frac{1}{2}(1 - \quad)^2 k_0^2\right]^{-\frac{1}{3}} \quad (\quad \gg 1). \tag{122}$$

To assess the decrease in the modulus g with amplitude k_0 for an arbitrary , we solve Eq. (119) numerically by the Newton method with 20 iterations and calculate the ratio

$$R(k_0) = \frac{g(k_0)}{G'(\infty)}$$

from Eq. (120). The function $R(k_0)$ is plotted in Fig. 14 for $= 10^{-3}$, 10^{-2}, 10^{-1}, 1, 10 and 100 (the dependencies $R(k_0)$ determined for $= 10^{-4}$ and $= 10^3$ coincide with the lower and upper curves in this figure). The results of numerical analysis show that (i) given a parameter , the modulus g monotonically decreases with amplitude of oscillations, and (ii) for a fixed amplitude k_0, it monotonically increases with the ratio of elastic moduli .

The reduction of the storage modulus with amplitude of oscillations has been observed experimentally in the 60s on carbon black-reinforced rubbers, and it is traditionally called the Payne effect, see [38] for a historical survey. To explain this phenomenon (observed in cross-linked as well as non-cross-linked polymer networks [39]), two mechanisms at the micro-level are introduced: (i) de-agglomeration of filler clusters, breakdown of a secondary network of filler, and stress-induced de-bonding of chains from filler particles [38], and (ii) nonlinear viscoelastic coupling between the flows of filler particles and the polymer matrix [39]. With reference to the later hypothesis, Eqs. (119) and (120) may be applied to assess the effect of the viscoelastic behavior of the host matrix on the evolution of the storage modulus with strain amplitude.

The conventional Kraus model [38] for the effect of amplitude of oscillations on the storage modulus of particle-reinforced polymer melts (where the plateau elastic modulus may be disregarded) provides the following estimate for the ratio R:

$$R(k_0) = \left[1 + \left(\frac{k_0}{k_*}\right)^{2m}\right]^{-1}, \tag{123}$$

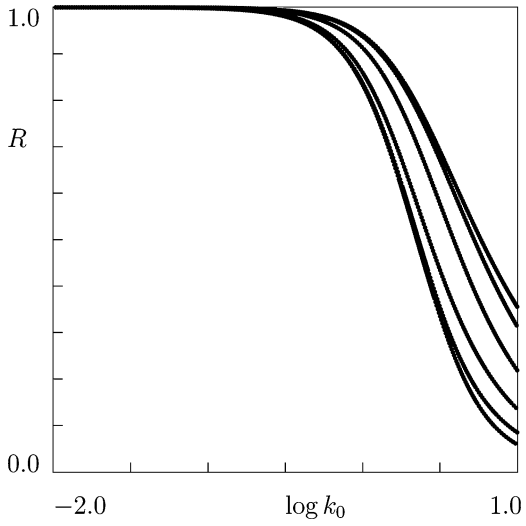

Fig. 14 The dimensionless ratio R versus amplitude k_0 of high-frequency shear oscillations for = 10^{-3}, 10^{-2}, 10^{-1}, 1, 10 and 100, from bottom to top, respectively

where k_* is some critical amplitude, and m 0 is an adjustable parameter. Approximation of numerous experimental data, as well as fractal models for breakdown of filler clusters result in the same value of the exponent $m \approx 0.6$, see [38]. It is worth to mention that at large amplitudes of oscillations, when $k_0 \gg 1$, Eq. (123) with $m \approx 0.6$ and our Eq. (122) imply the same scaling behavior $R \sim k_0^{-\frac{2}{3}}$. The latter confirms the importance of the account for the volumetric elastic energy (28) in the analysis of finite deformations of polymer fluids.

7 Concluding remarks

A novel constitutive model has been derived for polymer fluids. A polymer is treated as a network of chains linked by junctions (entanglements). Deformation of the network induces two processes at the micro-level: (i) sliding of junctions with respect to their reference positions in the bulk medium, and (ii) slippage of chains with respect to entanglements. The following kinematic hypotheses are introduced regarding these processes: (i) the vorticity tensor for sliding of junctions coincides with that for macro-deformation, and (ii) slippage of chains with respect to entanglements does not change the direction of end-to-end vectors of appropriate strands.

Constitutive equations for a non-affine polymer network are developed by using the laws of thermodynamics (which implies that the governing equations belong to the class of models with strain-dependent chain stretch according to the classification of [15]). It is presumed that the strain energy density of a network consists of two parts: (i) a conventional entropic strain energy associated with (a) a decrease in entropy of non-interacting Gaussian strands driven by their elongation and (b) an increase in entropy of the ensemble induced by its delation, and (ii) an elastic strain energy of interaction between strands described by the general Blatz–Ko formula. Internal dissipation of energy in the network is treated as the sum of conventional dissipative terms (quadratic with respect to appropriate rate-of-strain tensors) for sliding of junctions and elongation of strands. Governing equations for an arbitrary three-dimensional deformation with finite strains involve eight material parameters that have transparent physical meaning.

Two types of polymer fluids are analyzed. For type-I fluids, the viscosity of sliding of junctions increases with strain rate, whereas for type-II fluids, the growth of strain-rate intensity results in a decrease in the viscosity. The difference between these types of polymers may be observed in extensional flows, where the steady elongational viscosity increases with strain rate for type-I fluids and decreases for type-II fluids.

The constitutive equations are applied to the study of the time-dependent response of polymers in extensional and shear flows. For uniaxial extensional flows, explicit formulas are derived for steady elongational viscosity. Evolution of the transient viscosity in start-up tests and stress relaxation in relaxation tests are analyzed numerically. It is revealed that the account of slippage of chains with respect to entanglements

is important for modeling: in transient extensional tests, the elongation ratio of strands increases by several times. Other conclusions of the numerical simulation are that the model implies a strongly non-exponential response in relaxation tests, and that the time–strain correspondence principle is inapplicable to the constitutive equations.

For shear flows, analytical expressions are developed for the steady shear viscosity and the first and second normal stress differences. It is demonstrated that the steady shear viscosity decreases with shear rate both for type-I and type-II fluids. The steady stretch of strands increases with strain rate, but not so pronouncedly as in extensional flows. The transient response in shear tests is analyzed numerically. It is found that the shear stress and the normal stress differences grow monotonically with time to their ultimate values at relatively small shear rates. With an increase in strain rate, their behavior becomes non-monotonic: the shear stress and the normal stress differences demonstrate overshoots, whose intensities grow with shear rate. In accord with observations, it is shown that the maximum of the shear stress occurs earlier than the first normal stress difference reaches its maximum value.

Explicit expressions are developed for the storage and loss moduli as functions of frequency in dynamic tests with small amplitudes. It is demonstrated that slippage of chains with respect to entanglements is a second-order effect: this phenomenon does not affect the time-dependent response of a network at small strains. In the latter case, the constitutive equations are reduced to the conventional Maxwell model.

Shear oscillations with large amplitudes are studied analytically and numerically. It is shown that the steady periodic response of type-I and type-II fluids is qualitatively different. For type-I fluids, with an increase in amplitude of oscillations, the shape of the graph of shear stress versus shear rate changes from an ellipse to an oval and to a rhomboidal curve with relatively smooth edges. For type-II fluids, the growth of the amplitude of oscillations results in transformation of the graph of the shear stress as a function of shear rate from an ellipse to an S-shaped curve with sharp edges. These changes are mainly caused by slippage of chains with respect to entanglements. The dependence of elongation of strands on shear rate reveals a butterfly pattern for type-I fluids and a rabbit-ears pattern for type-II fluids. The frequency of oscillations in the ratio λ equals the double frequency of macro-deformation.

For high-frequency oscillations with large amplitudes, analytical expressions are derived for the storage modulus. These formulas are similar to the Kraus equation for the Payne effect in filled elastomers, but are grounded on a different physical model. It is demonstrated that the account of elastic interactions between strands is substantial: when these interactions are disregarded, the storage modulus decreases as k_0^{-2}, where k_0 is the amplitude of oscillations, whereas the presence of an elastic contribution into the strain energy density reduces the scaling exponent to $-\frac{2}{3}$, the value confirmed by numerous observations.

References

1. Johnson, M.W., Segalman, D.: A model for viscoelastic fluid behavior which allows non-affine deformation. J. Non-Newtonian Fluid Mech. **2**, 255–270 (1977)
2. Phan Thien, N., Tanner, R.I.: A new constitutive equation derived from network theory. J. Non-Newtonian Fluid Mech. **2**, 353–365 (1977)
3. Leonov, A.I.: Nonequilibrium thermodynamics and rheology of viscoelastic polymer media. Rheol. Acta **15**, 85–98 (1976)
4. Giesekus, H.: A simple constitutive equation for polymer fluids based on the concept of deformation-dependent tensorial mobility. J. Non-Newtonian Fluid Mech. **11**, 69–109 (1982)
5. Geurts, K.R., Wedgewood, L.E.: A finitely extensible network strand model with nonlinear backbone forces and entanglement kinetics. J. Chem. Phys. **106**, 339–346 (1997)
6. Green, M.S., Tobolsky, A.V.: A new approach to the theory of relaxing polymeric media. J. Chem. Phys. **14**, 80–92 (1946)
7. Tanaka, F., Edwards, S.F.: Viscoelastic properties of physically cross-linked networks. Transient network theory. Macromolecules **25**, 1516–1523 (1992)
8. Doi, M., Edwards, S.F.: The Theory of Polymer Dynamics. Clarendon Press Oxford (1986)
9. Lele, A.K., Mashelkar, L.A.: Energetically crosslinked transient network (ECTN) model: implications in transient shear and elongational flows. J. Non-Newtonian Fluid Mech. **75**, 99–115 (1998)
10. Archer, L.A., Mhetar, V.R.: Differential constitutive equation for entangled polymers with partial strand extension. Rheol. Acta **37**, 170–181 (1998)
11. Sun, N., Chan Man Fong, C.F., De Kee, D.: Network constitutive equation with internal viscosity: application to stress jump prediction. J. Non-Newtonian Fluid Mech. **95**, 135–146 (2000)
12. Sun, N., Chan Man Fong, C.F., De Kee, D.: A non-affine transient network model. Rheol. Acta **39**, 174–179 (2000)
13. Likhtman, A.E., Graham, R.S.: Simple constitutive equation for linear polymer melts derived from molecular theory: Rolie–Poly equation. J. Non-Newtonian Fluid Mech. **114**, 1–12 (2003)
14. Hua, C.C., Schieber, J.D., Venerus, D.C.: Segment connectivity, chain-length breathing, segmental stretch, and constraint release in reptation models. 3. Shear flows. J. Rheol. **43**, 701–717 (1999)

15. Wagner, M.H., Rubio, P., Bastian, H.: The molecular stress function for polydisperse polymer melts with dissipative convective constraint release. J. Rheol. **45**, 1387–1412 (2001)
16. McLeish, T.C.B., Larson, R.G.: Molecular constitutive equations for a class of branched polymers: the pom–pom model. J. Rheol. **42**, 81–110 (1998)
17. Inkson, N.J., McLeish, T.C.B., Harlen, O.G., Groves, D.J.: Predicting low density polyethylene melt rheology in elongational and shear flows with "pom–pom" constitutive equations. J. Rheol. **43**, 873–896 (1999)
18. Blackwell, R.J., McLeish, T.C.B., Harlen, O.G.: Molecular drag–strain coupling in branched polymer melts. J. Rheol. **44**, 121–136 (2000)
19. Rubio, P., Wagner, M.H.: LDPE melt rheology and the pom-pom model. J. Non-Newtonian Fluid Mech. **92**, 245–259 (2000)
20. Ianniruberto, G., Marrucci, G.: A simple constitutive equation for entangled polymers with chain stretch. J. Rheol. **45**, 1305–1318 (2001)
21. Verbeeten, W.M.H., Peters, G.W.M., Baaijens, F.P.T.: Viscoelastic analysis of complex polymer melt flows using the eXtended Pom-Pom model. J. Non-Newtonian Fluid Mech. **108**, 301–326 (2002)
22. Rallison, J.M., Hinch, E.J.: Do we understand the physics of the constitutive equations? J. Non-Newtonian Fluid Mech. **29**, 37–55 (1988)
23. Graham, R.S., Likhtman, A.E., McLeish, T.C.B., Milner, S.T.: Microscopic theory of linear, entangled polymer chains under rapid deformation including chain stretch and convective constraint release. J. Rheol. **47**, 1171–1200 (2003)
24. Read, D.J.: Convective constraint release with chain stretch: Solution of the Rouse-tube model in the limit of infinite tubes. J. Rheol. **48**, 349–377 (2004)
25. Beris, A.N., Edwards, B.J.: Thermodynamics of Flowing Systems. Oxford University Press, New York (1994)
26. Dressler, M., Edwards, B.J., Öttinger, H.C.: Macroscopic thermodynamics of flowing polymeric liquids. Rheol. Acta **38**, 117–136 (1999)
27. Bischoff, J.E., Arruda, E.M., Grosh, K.: A new constitutive model for the compressibility of elastomers at finite deformations. Rubber Chem. Technol. **74**, 541–559 (2000)
28. Ehlers, W., Eipper, G.: The simple tension problem at large volumetric strains computed from finite hyperelastic material laws. Acta Mech. **130**, 17–27 (1998)
29. Burgess, I.W., Levinson, M.: The instability of slightly compressible rectangular rubberlike solids under biaxial loading. Int. J. Solids Struct. **8**, 133–148 (1972)
30. Brink, U., Stein, E.: On some mixed finite element methods for incompressible and nearly incompressible finite elasticity. Comput. Mech. **19**, 105–119 (1996)
31. Rüter, M., Stein, E.: Analysis, finite element computation and error estimation in transversely isotropic nearly incompressible finite elasticity. Comput. Methods Appl. Mech. Engng. **190**, 519–541 (2000)
32. Murphy, J.G.: Strain energy functions for a Poisson power law function in simple tension of compressible hyperelastic materials. J. Elasticity **60**, 151–164 (2000)
33. Bin Wadud, S.E., Baird, D.G.: Shear and extensional rheology of sparsely branched metallocene-catalyzed polyethylenes. J. Rheol. **44**, 1151–1167 (2000)
34. Menezes, E.V., Graessley, W.W.: Study of nonlinear response of a polymer solution to various uniaxial shear flow histories. Rheol. Acta **19**, 38–50 (1980)
35. Takahashi, M., Masuda, T., Bessho, N., Osaki, K.: Stress measurements at the start of shear flow: comparison of data from a modified Weissenberg rheogoniometer and from flow birefringence. J. Rheol. **24**, 517–520 (1980)
36. Mason, T.G., Rai, P.K.: Shear-induced elastification of concentrated emulsions probed by sinusoidal amplitude variation rheometry. J. Rheol. **47**, 513–533 (2003)
37. Giacomin, A.J., Jeyaseelan, R.S., Samurkas, T., Dealy, J.M.: Validity of separable BKZ model for large amplitude oscillatory shear. J. Rheol. **37**, 811–826 (1993)
38. Heinrich, G., Klüppel, M.: Recent advances in the theory of filler networking in elastomers. Adv. Polym. Sci. **160**, 1–44 (2002)
39. Sternstein, S.S., Zhu, A.-J.: Reinforcement mechanism of nanofilled polymer melts as elucidated by nonlinear viscoelastic behavior. Macromolecules **35**, 7262–7273 (2002)

EUROPHYSICS LETTERS 1 November 2002

Europhys. Lett., **60** (3), pp. 390–396 (2002)

Crystallization of PDMS: The effect of physical and chemical crosslinks

T. Dollase[1,2,3](*), H. W. Spiess[1,2], M. Gottlieb[1,3] and R. Yerushalmi-Rozen[1,3](**)

[1] *The Reimund Stadler Minerva Center for Mesoscale Macromolecular Engineering*
[2] *Max-Planck-Institut fur Polymerforschung - Ackermannweg 10 55128 Mainz, Germany*
[3] *Department of Chemical Engineering, Ben-Gurion-University of the Negev Beer-Sheva, 84105, Israel*

(received 22 April 2002; accepted 19 August 2002)

PACS. 61.25.Hq – Macromolecular and polymer solutions; polymer melts; swelling.
PACS. 68.35.Md – Surface thermodynamics, surface energies.

Abstract. – Calorimetric studies of the crystallization behavior of physically and chemically crosslinked semicrystalline polymer, polydimethylsiloxane (PDMS) are presented. Physical crosslinks are introduced either via entanglements in high-molecular-weight PDMS, or by anchoring chain ends to rigid polyethylene oxide (PEO) endblocks in a PEO-*b*-PDMS-*b*-PEO triblock copolymer. Chemical end-linking of di-vinyl PDMS chains results in the formation of a crosslinked network. Comparison of the thermograms obtained for each of these systems at constant cooling/heating rates with their noncrosslinked analogues indicates that, contrary to conventional wisdom, the different types of crosslinks result in an increased crystallization tendency. We suggest that this effect is a manifestation of the enhancement of local ordering together with reduced dynamics as compared to the non-crosslinked melt.

The effect of topological and geometrical constraints such as transient entanglements, chemical and physical crosslinks on the crystallization of polymers from the melt is practically important and scientifically interesting. It is well known that polymer crystallization upon cooling of a melt is controlled by kinetic considerations [1,2]. In the framework of the classical crystallographic models, the presence of constraints that reduce the mobility of the chains should lead to a reduction in the crystallization rate and result in a lower degree of crystallinity at a given cooling rate. Yet, experimental findings suggest that in several cases crystallization from the entangled melt is more efficient than that from the non-entangled analogue [3].

Recently, a conceptually different mechanism of "spinodal-like" crystallization was suggested [4–7]. In the framework of this model, crystallization is expected to occur via the evolution of correlated density and structural fluctuations. The process is cooperative, and crystallization proceeds via a preordered granular crystalline mesophase. These ideas have

(*) Present address: Tesa AG - Quickbornstraße 24, 20253 Hamburg, Germany.
(**) E-mail: rachely@bgumail.bgu.ac.il

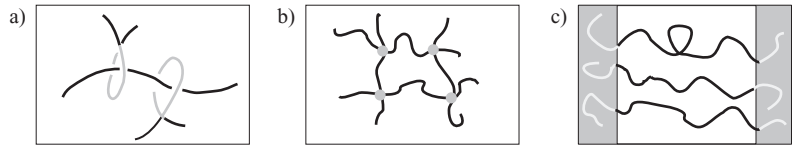

Fig. 1 – A schematic representation of a) entangled melt of polymers; b) a chemically crosslinked network of polymers; c) a triblock copolymer a-b-a where the two edge blocks are glassy at room temperature.

been supported by experimental observations [6, 7]. According to these concepts, regions that exhibit local ordering may facilitate the crystallization.

While geometrical and topological constraints are known to affect the dynamics of a melt [8, 9], it was suggested more recently that constraints can also lead to local ordering in globally amorphous polymer melts [10–13]. Rheological [9, 14], neutron scattering [15] and nuclear magnetic resonance (NMR) spectroscopy [16–18] approaches have been used to investigate these effects experimentally.

In this study we investigate the effect of topological and geometrical constraints on the crystallization of a simple semicrystalline polymer, polydimethylsiloxane, PDMS. Three types of crosslinks are examined: entanglements in PDMS homopolymers, endblocks which confine the central PDMS block in polyethyleneoxide-*b*-PDMS-*b*-polyethyleneoxide (PEO-*b*-PDMS-*b*-PEO) and chemical crosslinking of PDMS (fig. 1).

Differential-scanning calorimetry (DSC), which records heat flux changes as a function of time [19, 20], was used to follow the thermal behavior and in particular the crystallization kinetics of the different systems. Unless otherwise noted, experiments were carried at fixed cooling/heating rates of $\beta = \pm 5\,\mathrm{K\,min^{-1}}$. All data are normalized with respect to the weight fraction of the corresponding type of polymer (PDMS or PEO).

PDMS samples: $5000\,\mathrm{g\,mol^{-1}}$ (United Chemical Technologies, denoted PDMS 5k), PDMS $16000\,\mathrm{g\,mol^{-1}}$ (PDMS 16k), PDMS $100000\,\mathrm{g\,mol^{-1}}$ (PDMS 100k) were prepared by living anionic polymerization. PDMS 5k was end-linked, following Adam *et al.* [21], and is denoted x-PDMS 5k. The symmetric PEO-*b*-PDMS-*b*-PEO triblock copolymer was synthesized by Zhang [22]. The molecular weight of the PDMS center block is $12000\,\mathrm{g\,mol^{-1}}$, the PEO fraction is 25% corresponding to a molecular weight of $2000\,\mathrm{g\,mol^{-1}}$ per PEO block. PEO/PDMS blends were prepared by mixing PDMS 12k (UTC) and PEO 2k (Clariant AG) at 100 °C. The weight fraction of PEO in the blend is similar to that in the triblock copolymer (at room temperature the blend is in the two-phase regime).

A thermogram of PDMS 16k is presented in fig. 2 [8]. We regard PDMS 16k as effectively unentangled [8]. In agreement with other studies (for example, [23]) we find that following a cooling rate of $\beta = -5\,\mathrm{K\,min^{-1}}$ the DSC thermograms of linear PDMS 16k exhibit upon heating a glass transition, T_g, and a complex melting pattern, particularly typical double melting peaks [24].

In this study we used three features as (dependent) markers for probing the crystallization behavior of PDMS: the presence (or absence) of the exothermal peak appearing during the cooling cycle, T_g, and the value of ΔH_c, the phase transition enthalpy related to the cold crystallization process.

We observed that linear non-entangled PDMS does not crystallize during the cooling sequence at cooling rates as low as $\beta = -1\,\mathrm{K\,min^{-1}}$ [25]. Upon heating, the polymer crystallizes at T_c due to the reduction of melt viscosity. The latter enables chain rearrangements and leads to crystallization from the amorphous phase [2].

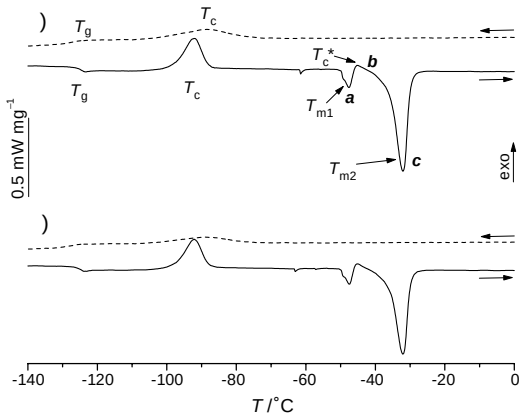

Fig. 2 – DSC thermograms of pure PDMS 16k, measured at a cooling/heating rate of $\beta = \pm 5\,\mathrm{K\,min^{-1}}$. The dashed line is a cooling curve, the solid line a heating curve: a) first run; b) subsequent run. In the cooling curve we observe an exothermal peak T_c and a glass transition at T_g ($T_g = -127.9\,^\circ\mathrm{C}$, $\Delta c_p = 0.19\,\mathrm{J\,g^{-1}\,K^{-1}}$). In the heating curve we observe a glass transition, T_g, an exothermic peak, the so-called cold crystallization, T_c ($T_c = -98.5\,^\circ\mathrm{C}$, $\Delta H_c = +22.5\,\mathrm{J\,g^{-1}}$), two melting peaks, T_{m1} (***a***) ($T_{m1} = 50.5\,^\circ\mathrm{C}$, $\Delta H_{m1} = -4.1\,\mathrm{J\,g^{-1}}$) and T_{m2} (***c***) ($T_{m2} = 34.0\,^\circ\mathrm{C}$, $\Delta H_{m2} = -31.0\,\mathrm{J\,g^{-1}}$), and a recrystallization exotherm, T_c^* (***b***) ($T_c^* = -47.4\,^\circ\mathrm{C}$, $\Delta H_{T_c^*} = +2.2\,\mathrm{J\,g^{-1}}$).

At a cooling rate $\beta = -5\,\mathrm{K\,min^{-1}}$, PDMS 100k and x-PDMS 5k exhibit a sharp crystallization peak during the cooling scan (figs. 3a and b, respectively) while the non-entangled PDMS 5k (fig. 3c and table I) and PDMS 16k (fig. 2) do not. The heating curve of PDMS 5k is very similar to that of PDMS 16k (fig. 2). For both PDMS 100k and x-PDMS 5k, substantial crystallization takes place during cooling, suggesting a higher crystallization rate than that of PDMS 5k. Note that for PDMS 100k the presence of a shallow peak in the heating curve indicates that crystallization is not completed during cooling. The melting sequence of the crosslinked PDMS displays only a single melting peak: We suggest that due to the inability of crosslinks to crystallize, the distance between adjacent crosslinks determines the thickness of the crystalline lamellae and prevents rearrangements and crystallite thickening.

The thermal behavior of PDMS segments was also examined in three symmetric PEO-*b*-PDMS-*b*-PEO systems with $12000\,\mathrm{g\,mol^{-1}}$ PDMS center blocks and terminal PEO blocks

TABLE I – *Numerical values of thermal transitions obtained by DSC for the PEO block as (temperatures in celsius) endblock in PEO-b-PDMS-b-PEO triblock copolymers (top); in PDMS/PEO polymer blends (bottom).*

PEO blocks in triblocks	cooling curve	$T_c = -28.8$ $\Delta H_{T_c} = +8.5\,\mathrm{J\,g^{-1}}$	
	heating curve	T_c non ΔH_{T_c} non	$T_{m1} = +48.3$ $\Delta H_{Tm1} = -13.4\,\mathrm{J\,g^{-1}}$
PEO in blend	cooling curve	$T_c = +37.8$ $\Delta H_{T_c} = +10.1\,\mathrm{J\,g^{-1}}$	
	heating curve	T_c n.o. ΔH_{T_c} n.o.	$T_{m1} = +52.6$ $H_{Tm1} = -13.4\,\mathrm{J\,g^{-1}}$

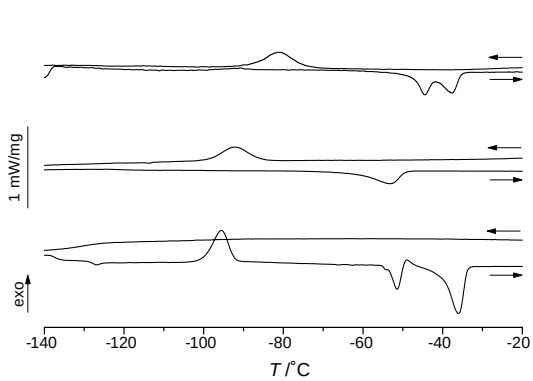

Fig. 3

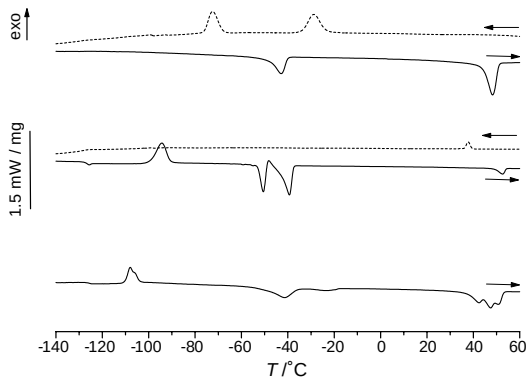

Fig. 4

Fig. 3 – DSC thermograms of PDMS measured at a cooling/heating rate of $\beta = \pm 5\,\mathrm{K\,min^{-1}}$. a) PDMS 100k. b) Crosslinked polymer, x-PDMS 5k. c) The non-crosslinked precursor, PDMS 5k.

Fig. 4 – DSC thermograms measured at a cooling/heating rate of $\beta = \pm 5\ \mathrm{K\,min^{-1}}$. a) 2k-12k-2k triblock copolymer (see numerical data in table II). b) A blend of PDMS 12k/PEO 2k with 28% weight fraction of PEO (table III). c) DSC thermogram of the 2k-12k-2k triblock copolymer measured at a heating rate of $\beta = +5\,\mathrm{K\,min^{-1}}$ following quench cooling in liquid nitrogen.

of different chain length ($550\,\mathrm{g\,mol^{-1}}$, $2000\,\mathrm{g\,mol^{-1}}$, $5000\,\mathrm{g\,mol^{-1}}$). While the thermograms differed with regard to the PEO behavior, the thermal features of the PDMS block were similar. Here we focus on the 2k-12k-2k triblock copolymer. Numerical data are summarized in tables II and III. Figure 4a shows that the PDMS blocks crystallize readily under the applied cooling conditions. A blend of PDMS 12k/PEO 2k with a weight fraction of PEO equal to the one present in the triblock copolymer (28%) was used as a reference, fig. 4b.

The thermogram of the PDMS/PEO blend is a simple superposition of the DSC curves of the respective pure homopolymers indicating the absence of significant interactions between PEO and PDMS. In particular, PDMS does not crystallize during the cooling scan at a cooling

Table II – *Numerical values of thermal transitions obtained by DSC for the PDMS block as (temperatures in celsius) center block in PEO-b-PDMS-b-PEO triblock copolymer (top); in PDMS/PEO polymer blends (bottom).*

PDMS blocks in triblocks	cooling	T_g n.o.	$T_\mathrm{c} = -72.5$			
	curve	Δc_p n.o.	$\Delta H_{T_\mathrm{c}} = +25.5\,\mathrm{J\,g^{-1}}$			
	heating	T_g n.o.	T_c n.o.	$T_\mathrm{m1} = -42.9$	$T_\mathrm{c}{}^*$ n.o.	T_m2 n.o.
	curve	Δc_p n.o.	ΔH_{T_c} n.o.	$\Delta H_{T\mathrm{m1}} = -27.7\,\mathrm{J\,g^{-1}}$	$\Delta H_{T_\mathrm{c}^*}$ n.o.	$\Delta H_{T\mathrm{m2}}$ n.o.
PDMS in blend	cooling	$T_\mathrm{g} = -126.0$				
	curve	Δc_p n.o.				
	heating	$T_\mathrm{g} = -128.0$	$T_\mathrm{c} = -94.3$	$T_\mathrm{m1} = -50.6$	$T_\mathrm{c}{}^* = -48.2$	$T_\mathrm{m2} = -39.4$
	curve	$\Delta c_\mathrm{p} = 0.33\,\mathrm{J\,g^{-1}\,K^{-1}}$	$\Delta H_{T_\mathrm{c}} = +25.2\,\mathrm{J\,g^{-1}}$	$\Delta H_{T\mathrm{m1}} = -14.1\,\mathrm{J\,g^{-1}}$	$\Delta H_{T_\mathrm{c}{}^*} = +1.8\,\mathrm{J\,g^{-1}}$	$\Delta H_{T\mathrm{m2}} = -26.4\,\mathrm{J\,g^{-1}}$

TABLE III – *Numerical values of thermal transitions obtained by DSC for the PEO block as (temperatures in celcius) endblock in PEO-b-PDMS-b-PEO triblock copolymers (top); in PDMS/PEO polymer blends (bottom).*

PEO blocks in triblocks	cooling curve	$T_c = -28.8$ $\Delta H_{T_c} = +8.5\,\mathrm{J\,g^{-1}}$	
	heating curve	T_c n.o. ΔH_{T_c} n.o.	$T_{m1} = +48.3$ $\Delta H_{Tm1} = -13.4\,\mathrm{J\,g^{-1}}$
PEO in blend	cooling curve	$T_c = +37.8$ $\Delta H_{T_c} = +10.1\,\mathrm{J\,g^{-1}}$	
	heating curve	T_c n.o. ΔH_{T_c} n.o.	$T_{m1} = +52.6$ $H_{Tm1} = -13.4\,\mathrm{J\,g^{-1}}$

rate of $\beta = -5\,\mathrm{K\,min^{-1}}$. Unlike the blend, PEO-*b*-PDMS-*b*-PEO exhibits two fairly sharp DSC features in the cooling scan, the crystallization exotherms of PEO and PDMS. In the heating scan neither a glass transition nor cold crystallization could be determined, but one melting peak for PDMS and one melting peak for PEO were observed.

Comparison of the corresponding thermograms suggests that while linear PDMS does not crystallize during the cooling scan down to a rate of $\beta = -1\,\mathrm{K\,min^{-1}}$, PEO-*b*-PDMS-*b*-PEO crystallizes readily at a cooling rate of $\beta = -5\,\mathrm{K\,min^{-1}}$. The heating run after quench cooling (in liquid nitrogen), fig. 4c, shows that the crystallization process of the PDMS block in the block-copolymer, can be suppressed under these conditions leading to vitrification of PDMS. Note that the crystallization of the PEO block in the triblock-copolymer is affected as well: During the cooling cycle the PEO block crystallizes at a lower temperature than in the blend. Yet, the degree of crystallization is greatly enhanced in the block copolymer as manifested by the magnitude of the crystallization and melting peaks (fig. 4, tables II, III).

The observation that topological and geometrical constraints enhance the crystallization rate of PDMS melts, may seem surprising at first sight, as constraints are believed to interfere with the crystallization process. However, polymer crystallization may be viewed as an ordering transition in which a small set of conformations becomes energetically favored, due to enthalpic considerations, leading to a severe reduction in conformational entropy. When crystallization is induced by rapid cooling the flexibility of the chains seriously diminishes, and the chains can only attain a limited ensemble of conformations separated by low activation energy barriers, rather than those of the lowest free energy. Thus, vitrification often dominates over crystallization. When the polymer melt is cooled at a slow enough rate, the probability of adopting the lowest-energy conformational state is increased, and some of the material can crystallize. If locally ordered regions are present in the melt, at elevated temperatures, the conformational space available to the melt chains is already reduced. While the specific type of order may not be that of the crystalline structure, the reduction in the total number of available conformations increases the probability of occupying the subset of conformations relevant to crystallizations. As long as the sub-set of conformations which lead to crystallization is not excluded, local ordering is expected to enhance crystallization. The elevated temperatures allow the system to span the reduced conformational space, and adopt the favored configurations over a shorter time period. In the case of PDMS, it may even be that the local organization of chains is lamellae-like resulting in a more specific enhancement of crystallization. This statement agrees with the key idea of the spinodal-like approach to polymer crystallization [4, 5].

In the following we discuss in detail the nature of the different constraints investigated

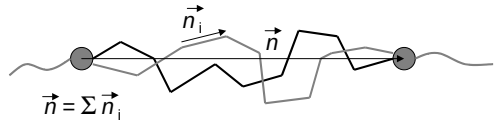

Fig. 5 – A schematic description of chain segments between two adjacent crosslinks.

in this study. Entanglements are topological constraints to chain dynamics that originate from intermolecular excluded-volume interactions [8, 9]. Entanglements affect the mechanical properties [8, 14] as well as the microscopic structure of amorphous polymers in the melt [16–18]. The reduction of the number of accessible conformations in entangled polymer melts and in chemically crosslinked networks leads to the loss of isotropic translational motion, as presented schematically in fig. 5. Indeed, the degree of local ordering can be quantified on different time scales by various NMR techniques, using the concept of local dynamic order parameter [16, 26, 27], defined as $S_i(t) = \frac{1}{2}\langle 3\cos^2\theta(t) - 1\rangle$, where $\theta(t)$ describes the angle between a local chain axis and the director.

Rigid endblocks in heterogeneous triblock copolymers are another type of physical crosslinks. They result from the formation of nanodomains with different solidification temperatures [28]. In PEO-*b*-PDMS-*b*-PEO both chain ends of the flexible PDMS block are anchored to rigid, glassy PEO blocks. Similar triblock copolymers were studied before by calorimetric techniques, yet not with respect to local ordering [29]. It was observed experimentally by Frederickson *et al.* [30] and later on by simulations [10, 11] that in such systems elongated chain conformations are favored. Indeed, recent NMR investigations on amorphous PS-*b*-PB-*b*-PS triblock copolymers revealed that local order in heterogeneous block copolymers is considerably larger and longer-lived than what is found in entangled homopolymer melts. Order parameters are increased by 150% for diblock copolymers and even 200% for triblock copolymers [26]. These findings were taken as evidence for considerable stabilization of the nanoscopic order.

In this study we show that the PDMS moiety in triblock copolymers crystallizes much more easily than in the blend. We suggest that this may be related to preordering of the triblock copolymer chains while still in the molten state, according to the scenario described above, in agreement with recent findings [31, 32]. Similarly, Hsu *et al.* [33] described the facilitation of structural evolution during crystallization by strongly interacting chains.

To conclude, we observed that crystallization is significantly enhanced by the presence of different types of crosslinks. We attribute the findings to substantial local chain ordering in the melt that facilitates conformational rearrangements necessary for crystallization. Although the origin of chain ordering for each of the different types of crosslinks might differ in detail, the outcome is similar.

* * *

We thank Z.-R. Zhang, T. Wagner and Y. Yagen for their help. The PEO 2k was kindly provided by Clariant AG. TD acknowledges the MINERVA foundation, and thanks M. Wilhelm for his support. RY-R and MG gratefully acknowledge the BSF Foundation grant no. 2000124.

REFERENCES

[1] Armistead K. and Goldbeck-Wood G., *Adv. Polym. Sci.*, **100** (1992) 219.
[2] Mandelkern L., in *Crystallization of Polymers* (McGraw Hill, New York) 1994.
[3] Ebengou R. H. and Cohen-Addad J. P., *Polymer*, **35** (1994) 2962.
[4] Heck B., Hugel T., Iijima M. and Strobl G., *Polymer*, **41** (2000) 8839.
[5] Strobl G., *Eur. Phys. J. E*, **3** (2000) 165.
[6] Terrill N. J., Fairclough P. A., Towns-Andrews E., Komanschek B. U., Young R. J. and Ryan A. J., *Polymer*, **39** (1998) 2381.
[7] Olmsted P. D., Poon W. C. K., McLeish T. C. B., Terrill N. J. and Ryan A. J., *Phys. Rev. Lett.*, **81** (1998) 373.
[8] Ferry J. D., *Viscoelastic Properties of Polymers*, 3rd edition (Wiley, New York) 1980.
[9] Graessley W. W., *Adv. Polym. Sci.*, **47** (1982) 67.
[10] Binder K. and Fried H., *Macromolecules*, **26** (1993) 6878.
[11] Murat M., Grest G. S. and Kremer K., *Macromolecules*, **32** (1999) 595.
[12] Baschnagel J. and Binder K., *Macromolecules*, **28** (1995) 6808.
[13] Starr F. W., Schroder T. B. and Glotzer S. C., *Phys. Rev. E.*, **64** (2001) 051503-1.
[14] Fetters L. J., Loshe D. J. and Graessley W. W., *J. Polym. Sci. Part B. Polym. Phys.*, **37** (1999) 1023.
[15] Rathgeber S., Willner L., Richter D., Brulet A., Farago B., Appel M. and Fleischer G., *J. Chem. Phys.*, **110** (1999) 10171.
[16] Cohen-Addad J. P., *J. Chem. Phys.*, **63** (1975) 4880.
[17] English A. D., Inglefield P. T., Jones A. A. and Zhu Y., *Polymer*, **39** (1998) 309.
[18] Graf R., Rheuer A. and Spiess H. W., *Phys. Rev. Lett.*, **80** (1998) 5738.
[19] Mathod V. F. (Editor), *Calorimetry and Thermal Analysis of Polymers* (C. Hanser, Munich) 1994.
[20] We used a Mettler Toledo Thermal Analysis System TA8000.
[21] Adam M., Lairez D., Karpasas M. and Gottlieb M., *Macromolecules*, **30** (1997) 5920.
[22] Zhang Z.-R. and Gottlieb M., to be published.
[23] Aranguren M. I., *Polymer*, **39** (1998) 4879.
[24] Liu S. L., Chung T. S., Oikawa H. and Yamaguchi A., *J. Polym. Sci., Part B. Polym. Phys.*, **38** (2000) 3018.
[25] The effect of the cooling rate on the crystallization of PDMS was investigated in a different study (Dollase T. *et al.*, *Effect of interfaces on the crystallization behavior of PDMS*, to be published in *Interface Science*). We found that under isothermal conditions crystallization is observed at $T \leq -60\,^{\circ}\mathrm{C}$.
[26] Dollase T., Graf R., Heuer A. and Spiess H. W., *Macromolecules*, **34** (2001) 298.
[27] Demco D. E., Hafner S., Fulber C., Graf R. and Spiess H. W., *J. Chem. Phys.*, **105** (1996) 11285.
[28] Bates F. S., *Science*, **251** (1991) 898.
[29] Shin H.-Y., Kuo W. F., Pearce E. M. and Kwei T. K., *Polym. Adv. Tech.*, **6** (1995) 413.
[30] Almdal K., Rosedake J. H., Bates F. S., Wignall G. D. and Frederickson G. H., *Phys. Rev. Lett.*, **65** (1990) 1112.
[31] Zhu L. *et al.*, *Macromolecules*, **34** (2001) 1244.
[32] Chen H.-L., Hsiao S.-C., Lin T.-L., Yamauchi K., Hasegawa H. and Hashimoto T., *Macromolecules*, **34** (2001) 671.
[33] Heintz A. M., to be published in *Macromolecules*, **35** (2002).

The Importance of Liquid Compressibility in Calculations of Fluid Dynamics Inside a DOD Piezoelectric Ink Jet Nozzle

E. Magen and M. Gottlieb*

Chemical Engineering Department, Ben Gurion University of the Negev, Beer Sheva, Israel

This study is aimed at determining the effect of the minute liquid compressibility on the flow of ink in a piezo-diaphragm driven Drop-On-Demand (DOD) ink jet nozzle. This goal is achieved by a comparison between the results obtained numerically for compressible and incompressible flows by means of Computational Fluid Dynamics calculations. In these calculations the exact geometry of the entire flow channel is modeled. Significant differences between the two flow models are observed in many aspects of the flow and drop evolution characteristics. Also, in some cases, seemingly similar features have been found to result from different physical driving forces. Despite the low Mach number and low condensation values involved, the very slightly compressible flow and the incompressible flow are very different. It is concluded that acoustic effects cannot be ignored and the incorporation of ink compressibility in the physical analysis of this flow system is essential.

Journal of Imaging Science and Technology 48: 335–341 (2004)

Introduction

It is common practice in fluid dynamics modeling and calculations to assume that unless exposed to extremely high pressures, liquids are practically incompressible. The incompressibility assumption results in substantial simplification of the governing equations allowing solution of otherwise intractable problems. Published investigations of the fluid dynamics in drop-on-demand (DOD) piezoelectric ink jet devices differ in their attitude towards the importance of ink compressibility in defining the physical behavior of the liquid inside the nozzle. Some researchers follow common practice and completely ignore liquid compressibility in their flow models[1] or simulations.[2] Others[3–6] assign a great deal of importance to the ink's minute compressibility and consequential acoustic effects. Dimensional analysis, which is often useful in identifying the important physical features in a given system, yields inconclusive results in this case, as will be demonstrated below. Thus, it is impossible to reach a conclusion regarding the importance of ink compressibility in the operation of DOD piezoelectric ink jet nozzles without undertaking a comprehensive study of this issue.

Experimental studies of the flow in piezoelectric ink jet nozzles are extremely difficult due to the highly transient nature of the flow as well as to the miniature and complex geometry of the flow channel. The high speed, transient flow and the complex boundary conditions limit the possibility for analytical solutions for the flow field. Thus, a numerical approach to the modeling of the system is the only viable alternative to obtain pressure and velocity distribution data not readily available from experiments. Yet, a numerical solution depends on the physical model prescribed to the system and once again one is faced with the question whether compressibility effects should be taken into account. Incorporation of liquid compressibility into the model imposes a major burden on the numerical scheme and requires extensive computational resources. Hence, resolution of this issue should provide a great service for future research.

The objective of this study is to present a detailed study of the effect of the minute compressibility of ink on the fluid behavior in DOD devices. This is achieved by comparing the behavior of compressible and incompressible liquids in the course of drop formation in a commercial piezo-diaphragm ink jet nozzle. More specifically, we compare the instantaneous internal pressure distribution and meniscus perturbations during short time intervals calculated numerically for these two types of liquids. To carry out these calculations use was made of a Computational Fluid Dynamics (CFD) software package based on the Finite Element Method.[7] This investigation also allows us to fully appreciate the importance of acoustics in these systems.

Nozzle Description and Theoretical Framework

A cross-section of a single commercial piezo-diaphragm nozzle, designed and manufactured by Aprion (Aprion Digital Ltd, Netanya 42505, Israel) is shown in Fig. 1. The nozzle consists of two cylindrical hollow tubes removed from a porous metal, which wraps the ink

Original manuscript received September 24, 2003

* Moshe@inca.bgu.ac.il; fax: +972.8.647.2916

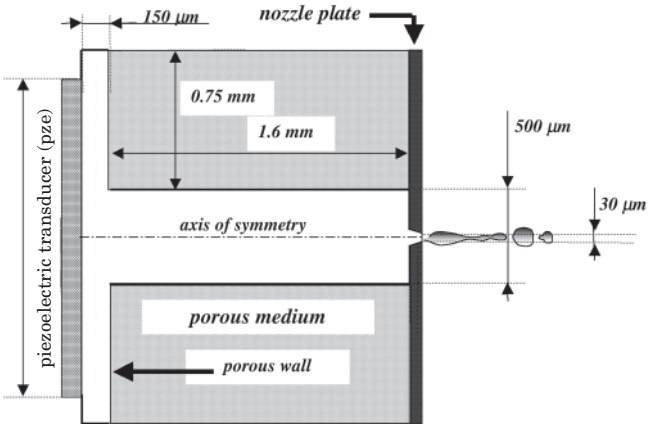

Figure 1. Details of the Aprion DOD ink jet nozzle.

chamber and enables flow of ink into or out of the ink reservoir. The circular piezoelectric transducer (pze) is located opposite to the nozzle exit at the back-end of the flow channel. A detailed description of the nozzle geometry is given elsewhere.[8,9]

The voltage applied to the pze triggers its deformation. Upon deformation, the pze arches into or out of the ink cavity, and subsequently ejects a drop of ink with a typical velocity of ~10 m/s. The applied voltage is a rectangular pulse with a typical duration of T_2 = 2–5 μs, and a drop ejection cycle T_1 > 10 μs (or single nozzle jetting frequency <100 kHz). Measurements carried out in Aprion laboratories revealed that the deformation rise time of the pze is approximately 1 μs.[10] The following values have been selected to represent the water based ink: $\rho_0 = 10^3$ Kg/m^3 for the equilibrium density, $\sigma = 0.03$ N/m for the surface tension, and $\mu = 10^{-2}$ Pa•s for ink viscosity.

Based on a dimensional analysis in which nozzle diameter and drop velocity were used for characteristic length and velocity, respectively, it was concluded that the flow is laminar, surface tension forces are probably of importance, and gravitational forces are negligible. Despite the low Reynolds number, inertial forces are not ignored in view of the large acceleration of the meniscus during drop formation.[8,9]

As already mentioned, we will attempt to estimate the importance of liquid compressibility by dimensional analysis. Although volume changes in liquids are generally negligibly small, the very fast pze deformation (Δt~1μs) inside the small ink chamber may result in non-negligible acoustic effects.

For small density fluctuations in liquids, a linear relationship may be written between the acoustic pressure p, i.e., the gauge pressure which is the excess pressure above the reference equilibrium pressure, and the local change in density[11]:

$$p = (\rho - \rho_0)C^2 = s\rho_0 C^2 \tag{1}$$

Here ρ_0 is the equilibrium density, ρ is the instantaneous density, C is the speed of sound in the medium, and s is the condensation (defined as the relative change in density $s = (\rho - \rho_0)/\rho_0 = \Delta\rho/\rho_0$).

In general, we consider "incompressibility" a good approximation for a given flow when the condensation is much smaller than unity. In steady flows, the maximum change in pressure can be estimated from the stagnation pressure:

$$p = \rho_0 u^2 \tag{2}$$

where u is the fluid velocity.

Insertion into Eq. (1) results in the following expression for the condensation:

$$s = (u/C)^2 = Ma^2 \tag{3}$$

Hence, in a steady flow the incompressibility assumption is valid if the liquid velocity is much smaller than the speed of sound in the liquid:

$$Ma = u/\mathrm{C} << 1 \tag{4}$$

Here Ma is the Mach number. The Mach number delineates three flow regimes: For $Ma \geq 1$ the ultrasonic flow system is subjected to shock waves and for $Ma << 1$ the flow is considered incompressible. The intermediate regime in which $Ma < 1$ but is not much smaller than unity is the compressible flow regime. Obviously, the determination of the border line between "smaller" and "much smaller" than unity is somewhat arbitrary and depends on the specifics of the flow system.

For the estimation of the maximum change in pressure in a transient flow, let us consider the following case: A piston with a cross sectional area A, accelerates from rest to a velocity u within a time interval of Δt in a pipe of length L filled with an inviscid fluid. Using Newton's second law we may write an expression for the pressure:

$$p = \frac{\Sigma F}{A} = \rho_0 L \frac{u}{\Delta t} \tag{5}$$

By equating Eqs. (5) and (1), we obtain the following expression for the condensation:

$$s = \frac{L}{C^2}\frac{u}{\Delta t} = (\frac{L}{C\Delta t})Ma \tag{6}$$

Thus, in the case of unsteady flow, the incompressibility assumption is valid if two conditions are satisfied: (i) $Ma << 1$ as stated by Eq. (4); (ii) The distance traveled by the sound wave during the characteristic time interval Δt, should be much larger than the dimensions of the flow system, L:

$$\frac{L}{C\Delta t} << 1 \tag{7}$$

Unless the latter condition is met the propagation of pressure changes along the flow system may not be considered instantaneous relative to the time interval Δt. As result, acoustic effects cannot be ignored and liquid compressibility should be considered.[14]

In order to assume ink compressibility for the transient flow inside a DOD nozzle, the conditions specified by Eqs. (4) and (7) or by Eq. (6), should be satisfied. Using the drop velocity as the characteristic velocity of the ink and taking C = 1500 m/s (close to the speed of sound in water at 20°C and atmospheric pressure[11]) we may obtain an estimate for the Mach number, Ma ~

0.007 << 1. To evaluate the second condition we use the pze characteristic time of deformation (~ 1 μs) as the representative time interval over which the flow changes significantly. It results in: $L/(C\Delta t) \sim 1.2$, which implies that the distance traveled by a sound wave during the time required for pze deformation is of the order of the ink chamber length. Hence, pressure propagation in the ink chamber as result of the pze deformation cannot be considered instantaneous. Yet, if we use these values in Eq. (6) we find that the condensation s << 1, which should justify the use of the incompressibility assumption. Thus, we are unable to either support or refute the incompressibility assumption due to the ambiguous results obtained from the dimensional analysis.

The behavior of this laminar Newtonian ink jet ejection system is governed by the equation of motion and the equation of continuity.[12] As may be appreciated from Fig. 1, the symmetry axis of the cylindrical flow channel can be used to reduce the problem into a 2-dimensional (2D) axisymmetric problem. Thus, in this work we solve the 2D axisymmetric laminar flow of a (1) slightly compressible and (2) incompressible, Newtonian liquid taking into account inertial and surface tension effects.

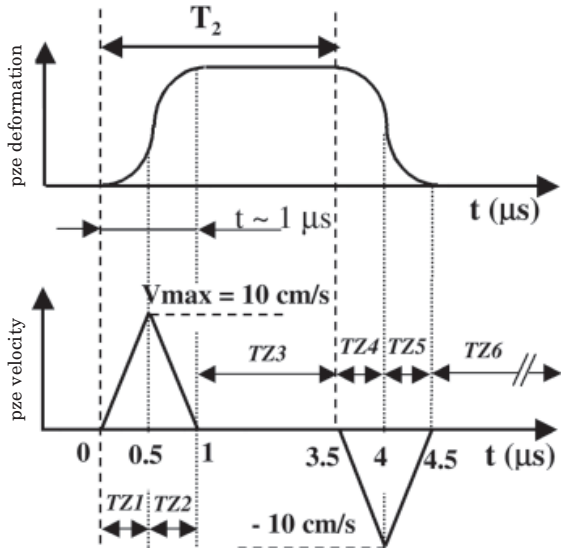

Figure 2. Deformation and velocity of the piezoelectric transducer wall in the axial direction and the definition of time zones (TZ).

The Computational Set-up

The fluid dynamics computations, were performed by means of a CFD commercial package POLYFLOW 3.6.0 (Polyflow S.A., Louvain-La-Neuve, Belgium), which employs the finite element method.[7] The details of the computational scheme and its implementation in this problem are described in great detail elsewhere.[8,9] Here we only give a brief outline of its salient features.

The computer representation of the system geometry is based on a cylindrical coordinate system with its origin positioned on the symmetry axis at the nozzle exit plane. Negative z values refer to distances upstream from the nozzle exit. The following boundary conditions (BC) have been used to describe the system:

1. *Solid walls*. "No slip" BC at solid walls: tangential velocity $V_s = 0$ and normal velocity $V_n = 0$.
2. *Axis of symmetry*. Symmetry BC: shear stress $\tau_s = 0$ and $V_n = 0$.
3. *The porous wall*. The porous medium, which wraps the ink chamber, is not included in the modeled geometry and is replaced by a "thin" (1D) porous wall boundary, which allows flow in and out of the ink chamber. The numerical implementation of this boundary condition comprises of a zero tangential velocity component ($V_s = 0$) along with a Darcy-like linear relationship between the normal stress (τ_n) and the normal velocity at the boundary:[13]

$$\tau_n = (\mu L_p/k_p)V_n \quad (8)$$

   where μ is the viscosity of the fluid, L_p (= 2 mm) and k_p (= 2×10^{-12} m^2) are the thickness and permeability of the porous wall, respectively.
4. *Free surface*. The interfacial normal stress (τ_n) is equated to the sum of the outer pressure, P_0, and the capillary pressure.

$$\tau_n = P_0 + 2R/\sigma \quad (9)$$

Here R is the Gaussian curvature of the surface and is a part of the flow solution. The outer pressure is set to zero, turning the calculated pressure into acoustic (gauge) pressure. The kinematic condition for the moving free-surface states that it must follow material points in the normal direction at all times, i.e., no mass flux across it.[13]

5. *The pze wall*. The response of the pze to a rectangular voltage pulse with a duration of T_2 = 3.5 μs, is represented by a symmetric sigmoidal deformation function with rise and decay times of 1 μs each, as depicted in Fig. 2. The pze wall BC is defined by means of the velocity function obtained from the time derivative of the deformation function rather than by the deformation function itself. *Vmax*, the maximum pze wall velocity, is assigned the value 10 cm/s required to reproduce the experimentally observed average meniscus velocity of 10 m/s.

For the sake of convenience in subsequent discussion, the pze wall velocity function was divided into six "time zones" (*TZ*). *TZ1* and *TZ2* correspond to the forward stroke of the pze wall. The time interval between the forward and backward strokes of the pze wall (zero velocity and maximum deformation) is labeled *TZ3*. The backward stroke of the pze wall into its original position occurs during *TZ4* and *TZ5*. Once returned to its original position, the pze wall is at rest (zero velocity and zero deformation) during *TZ6* until the next pulse is applied. The initial time $t = 0$, corresponds to the initial rise of the pze wall and is the reference time for all the results discussed here. It should be noted that the pze wall may experience additional deformation as result of the pressure reflection from the nozzle exit onto it. Due to the extremely small volume change even at its largest applied voltage, changes due to back pressure will not affect significantly the velocity pattern of the pze wall itself as shown in Fig. 2. Yet, deformation of the pze wall under the reflected pressure may alter subsequent pressure reflections at longer times and the resulting flow field near the back wall of the ink chamber. These effects have not been studied here and may merit further examination in the future.

To prevent divergence of the numerical scheme the maximum time step used in the numerical solution in view of the dimensions of the elements and the speed of sound, is set to 0.01 μs. For the compressible ink model

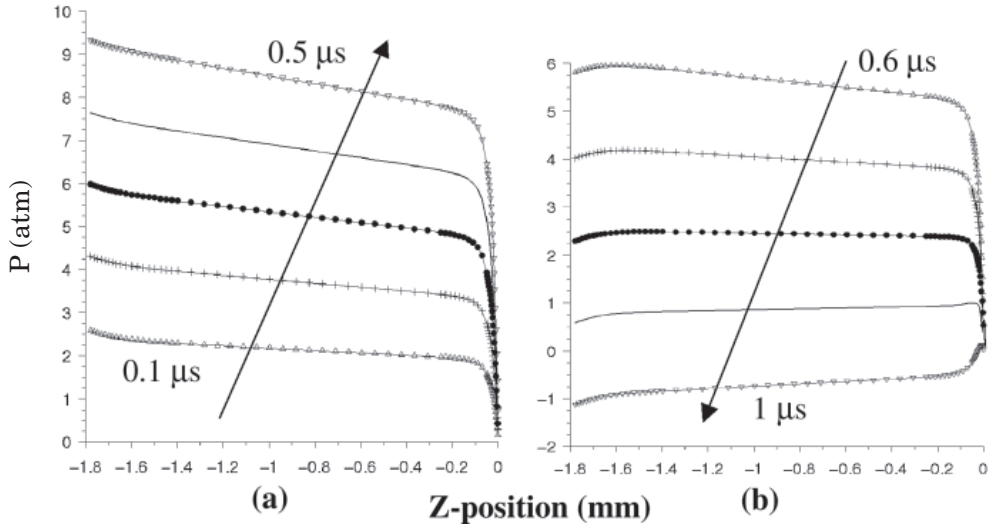

Figure 3. Incompressible flow. Pressure along the symmetry axis for times between (a) t = 0.1 – 0.5 μs (*TZ1*), and (b) 0.6 – 1 μs (*TZ2*), Δt = 0.1 μs. Time increases in the direction of the arrow.

the instantaneous ink density, ρ, is related to the pressure field p, by Eq. (1), whereas for the incompressible ink model the density is maintained at a constant value equal to the equilibrium density, ρ_0.

Numerical Results

In what follows we compare the results obtained for compressible and incompressible flows. Initially we compare the evolution of pressure inside the flow chamber during the pze forward stroke. Yet, since the objective of a DOD ink jet nozzle is to generate drops, most of the comparison is dedicated to the differences in the evolution of drop formation. To capture the features in this highly transient flow, the results are presented at time intervals of 0.1 μs. These time intervals should not be confused with the computation time-steps which are always smaller than 0.01 μs.

Figure 3 depicts the pressure values in an incompressible liquid along the symmetry axis at different times from 0.1 to 1.0 μs with a 0.1 μs interval, throughout the forward stroke of the pze (time zones *TZ1* and *TZ2*). In this and in subsequent figures the pze wall is positioned at the extreme left (z = –1.8 mm), and the nozzle exit at the extreme right (z = 0). We have shown elsewhere[8,9] that with few exceptions, symmetry axis pressure values provide good representation of the pressure in the flow channel. The increase in velocity (during *TZ1*) is accompanied by pressure increase (Fig. 3(a)), whereas the decrease in velocity (during *TZ2*) is accompanied by pressure decrease (Fig 3(b)). In both cases the pressure drop along the ink chamber (axial direction) is very moderate and most of the time it is limited to less than 1 atm. A notable exception is observed at close proximity to the nozzle exit section, in which the pressure drops to zero as imposed by the free surface boundary condition leading to large pressure gradients at the nozzle exit. At t = 0.1 μs the maximum pressure, located on the pze wall, already attained a value of 2.7 atm. Subsequently, the pressure increases at a constant rate of ~ 20 atm/μs reaching its maximum value of 9.5 atm still at the pze wall. This maximum is achieved at t = 0.5 μs which corresponds to the end of *TZ1* the time at which the pze wall reaches its maximum velocity *Vmax*. At the onset of wall deceleration at times corresponding to *TZ2*, pressure values (depicted in Fig. 3(b)) drop dramatically reaching a minimum value of –1.1 atm (gauge) on the pze wall at t = 1 μs. Also, the maximum value in the pressure is no longer at the pze wall shifting to the right with time.

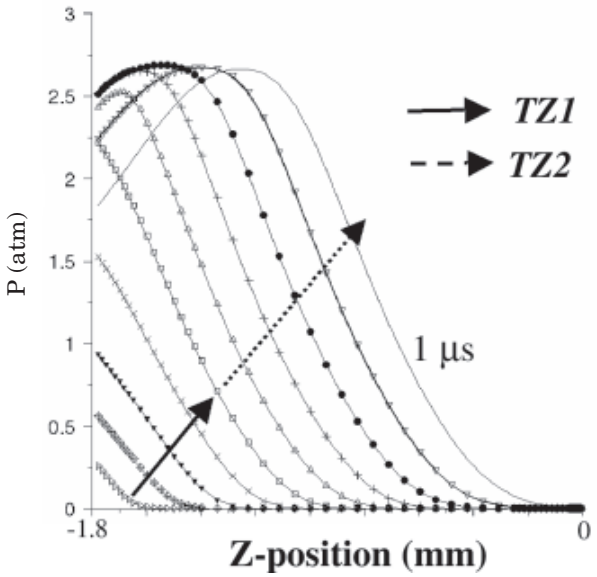

Figure 4. Compressible flow. Pressure along the symmetry axis for times between t = 0.1 – 1 μs (*TZ1* and *TZ2*, Δt = 0.1 μs). Time increases in the direction of the arrow.

Figure 4 depicts the pressure profile along the symmetry axis for a compressible flow. The time here varies between 0.1 – 1 μs as well, corresponding to time zones *TZ1* and *TZ2* (forward stroke) with intervals of 0.1 μs. It can be seen that the pressure builds up gradually next to the transducer, and propagates towards the nozzle exit with a fairly steep axial pressure gradient throughout the flow channel. The pressure on the pze wall increases with time until t ~ 0.5 μs (end of *TZ1*), paralleling the linear increase in the velocity at *TZ1*. The pressure peaks at 2.7 atm almost at the same time *Vmax* is reached. This is followed by a moderate decrease in pressure on the pze wall down to a value of 1.75 atm, reached at t = 1 μs. As the pressure wave propagates towards the nozzle exit, it maintains its peak value.

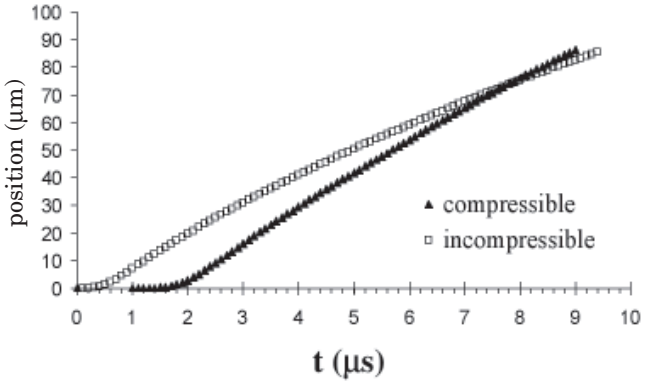

Figure 5. The protrusion of the meniscus tip versus time. Comparison between compressible and incompressible flows.

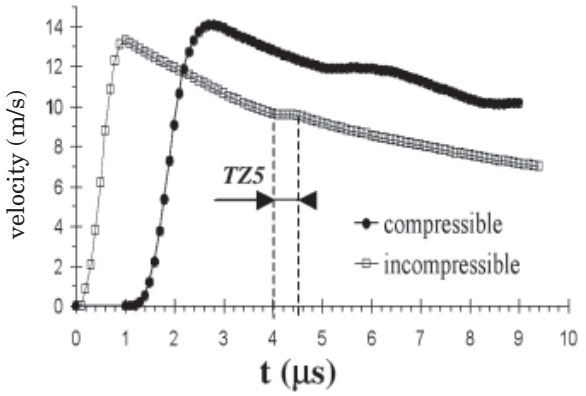

Figure 6. Time evolution of the meniscus-tip velocity for compressible and incompressible flows.

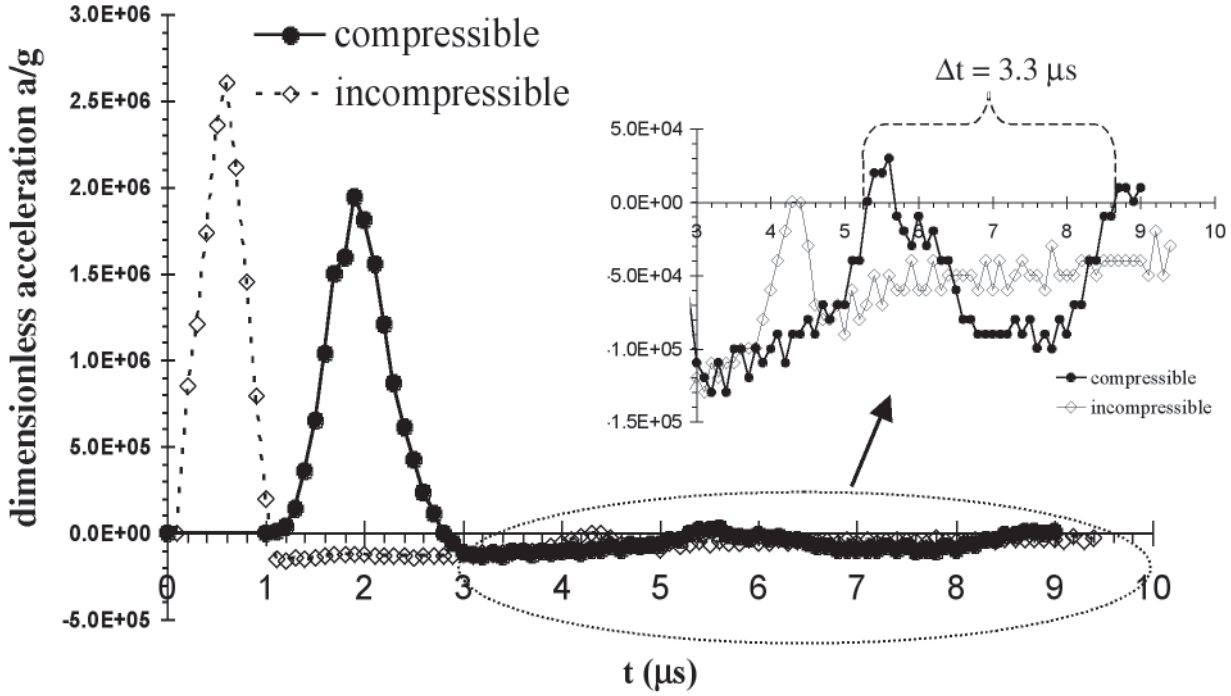

Figure 7. Acceleration of the meniscus tip vs. time for compressible and incompressible flows.

In Fig. 5 the calculated extent of protrusion of the meniscus tip as a function of time is shown for compressible and incompressible flows. For the compressible flow, there is a lag of 1.7 μs between the onset of motion of the pze wall and a discernable motion at the meniscus tip. For the incompressible flow, the motion of the meniscus tip is nearly instantaneous (0.4 μs). In both cases, the meniscus reaches a distance of three nozzle diameters (85 μm) from the nozzle exit after approximately 9 μs. The calculations were not pursued beyond this time (~ 9 μs), due to significant distortion of the mesh elements at the nozzle exit region.

By taking the time derivative of the meniscus tip position we have obtained the meniscus tip velocity shown in Fig. 6. Tip velocity provides a more sensitive discrimination between the features of compressible and incompressible flows. In the case of compressible flow, the velocity of the meniscus tip is zero for times shorter than 1.2 μs. For times longer than 1.2 μs, the meniscus tip accelerates until it reaches its maximum velocity (14 m/s) within 1.5 μs from the onset of its motion or 2.7 μs from the onset of the pze pulse. At this point, the velocity starts to decelerate moderately to a value of 10 m/s as $t \rightarrow 9$ μs. Still, the decrease in velocity is not completely monotonous and shows some waviness. For the incompressible flow, the meniscus reaches a slightly lower maximum velocity value of 13 m/s within 1 μs from the onset of the pze pulse. It then decreases moderately to a value of 7 m/s as $t \rightarrow 9$ μs with a single prominent interruption during *TZ5*.

From the time derivative of the velocity of the meniscus tip we have obtained its acceleration (Fig. 7). Considerable amount of "noise" is discernible in this figure as result of the inherent inaccuracies involved with numerical differentiation.

In the case of the compressible flow, the meniscus tip starts to accelerate at $t = 1$ μs, reaching its maximum acceleration value of 2×10^6 g at $t = 1.9$ μs (within *TZ3*),

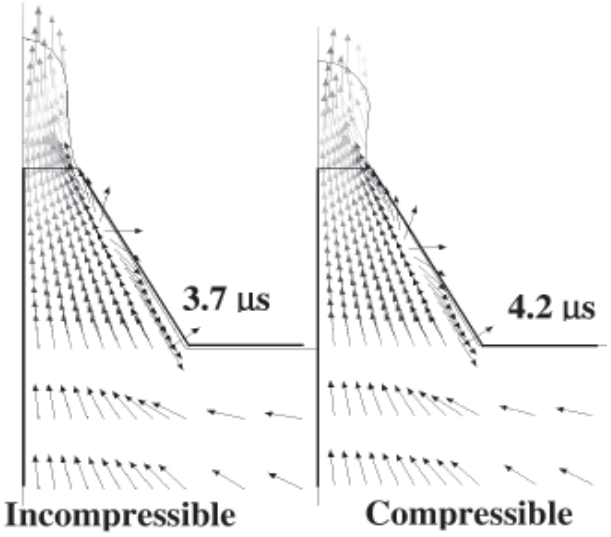

Figure 8. Onset of flow reversal at the tapered exit section of the nozzle for compressible (t = 4.2 μs) and incompressible (t = 3.7 μs) flows. The magnitude of the velocity vectors is indicated by their shading from black (lowest velocity) to gray (highest velocity).

and at t = 2.8 μs, the meniscus tip starts to decelerate. Intermittently, it gains relatively minor positive acceleration values of 3×10^4 g and 1×10^4 g at t = 5.3 μs and 8.6 μs respectively (Δt = 3.3 μs, both in *TZ6*). For the incompressible flow the meniscus tip accelerates almost instantaneously reaching a maximum value of 2.6×10^6 g at t = 0.6 μs. For times past 1.1 μs, the meniscus tip decelerates, with one exception occurring during *TZ4* and *TZ5*.

Inspection of the changes in the velocity field taking place in the nozzle exit region reveals that the meniscus acceleration induces suction of ink towards the exit plane from its adjacent surroundings. This behavior is observed for the compressible[8] as well as the incompressible flow. In the case of incompressible flow, the induced suction affects the entire ink chamber and the flow field is directed everywhere towards the nozzle exit. In contrast, for the compressible flow the suction induced by the drop is opposed by the pressure and flow reflections from walls and boundaries acting in the opposite direction.[8] Yet, in the tapered section the flow patterns are qualitatively similar for both models as shown in Fig. 8. The uniformly directed flow toward the exit at the tapered section of the nozzle is interrupted by the reversal of the flow field setting in near the wall of the tapered section (25 μm from the nozzle exit). The onset of flow reversal is first observed at t = 4.2 μs for compressible flow and at t = 3.7 μs for incompressible flow (see Fig. 8). At this point most of the ink in the vicinity of the nozzle plate flows outwards following the meniscus motion with a small portion of the liquid at a certain point near the walls flowing inwards. With time the extent of the inwards-flow zone increases in size, expanding towards the drop base and towards the center line and eventually it leads to formation of a bifurcation plane between the drop and the bulk of the ink.

Discussion

The results shown above clearly demonstrate the large differences in flow behavior resulting from the incorporation of acoustic effects. This is despite the fact that for 10 atm, the maximum pressure variation in our flow system, density variation (cf. Eq. 1) is at most 0.5 kg/m^3 which is equivalent to 0.05% of the liquid equilibrium density.

For incompressible flow as expected, the pressure in the ink chamber builds up instantaneously and almost uniformly. The maximum pressure is four times higher than that observed near the pze wall in compressible flow, in which the pressure builds up gradually and propagates with time toward the nozzle exit. The fourfold decrease in pressure values for the compressible flow cannot be fully attributed to the minor compressibility of the ink although some of the pze impact energy is probably absorbed by ink compression. The main source for the difference in pressure values stems from the fact that in the incompressible flow the mechanical energy is transferred instantaneously to the exit wall giving rise to the pressure surge. The magnitude of the pressure is in par with values estimated from a simple macroscopic mechanical energy balance.[12] Whereas, in the compressible flow the time it takes the mechanical energy or the velocity (cf. Figs. 4 and 6) fronts to reach the exit plane and the associated relatively large axial pressure (and hence velocity) gradients allow for additional dissipation of the mechanical energy.

In the case of compressible flow, strong coupling is found[8,9] between the pressure reflections at the nozzle plate end and the meniscus acceleration. The meniscus accelerates exactly at the instant the pressure wave arrives at the meniscus, and reaches its maximum acceleration value at the same time the reflected pressure reaches its peak value (t ~ 1.8 μs). This is also partially true for the incompressible flow: the meniscus starts accelerating at the onset of pze deformation since pressure propagation in incompressible flow is instantaneous, and the maximum acceleration is related to maximum pressure. Yet, time and magnitudes of these features vary between the two flows.

The evolution of meniscus acceleration depicted in Fig. 7 shows qualitatively similar features for both types of flows in the form of small bursts of acceleration in the deceleration region past the large acceleration peak: in the compressible flow they occur at t = 5.3 and 8.6 μs (*TZ6*) and in the incompressible flow at t = 4.3 μs (*TZ5*). Yet, despite the superficial similarity between the two models, the physical mechanism responsible for these features is very different. In the case of compressible flow the small bursts of meniscus acceleration were found to be related to secondary pressure wave reflections on the nozzle plate. This cannot be the source of the single burst observed for the incompressible flow since the latter is not subjected to acoustic propagation and reflections. Intuitively, one would expect an increase rather than the observed decrease, in meniscus deceleration during *TZ4* and *TZ5* due to the backwards motion of the pze (cf. Fig. 2). Initially, we attributed this acceleration surge to surface tension forces arising from the inclination towards detachment of the drop as the free surface area is increased by the forward motion of the meniscus. Yet, solving the same problem excluding surface tension forces from the model resulted in qualitatively similar behavior, ruling out surface tension as the source of acceleration surge in incompressible flow.

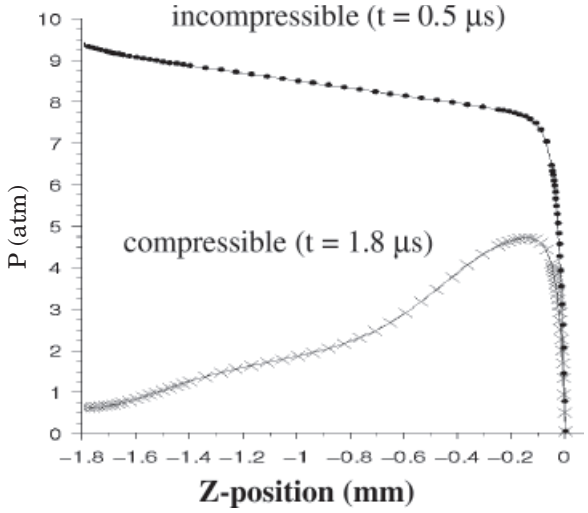

Figure 9. The axial pressure distribution along the symmetry axis upon reaching the highest pressure value in the system. Comparison between the compressible (t = 1.8 μs, within *TZ3*) and incompressible (t = 0.5 μs, within *TZ1*) flows.

The physical mechanism responsible for this feature was finally identified[8] as the flow of ink into the ink chamber through the porous wall during the backward motion of the pze during *TZ4* and *TZ5*.

The pressure profile curves along the symmetry axis at the corresponding times at which the maximum pressure value has been attained for each flow model are shown in Fig. 9. The largest pressure magnitudes are observed at t = 1.8 μs (*TZ3*) and t = 0.5 μs (*TZ1*) for the compressible and incompressible flows, respectively. Since as indicated in Fig. 9, the largest pressure in the incompressible flow is considerably larger than that for compressible flow it is natural to expect correspondingly higher meniscus velocity and acceleration in the former. Yet, Fig. 6 shows a slightly larger meniscus velocity for the compressible flow and although the maximum acceleration of the incompressible meniscus tip is higher than that of the compressible flow (Fig. 7), the difference does not reflect the large difference in pressure values (Fig. 9). This discrepancy is attributed to the short lived increase and decrease of the pressure in the case of incompressible flow, as opposed to the relatively slow pressure reflection at the nozzle exit section in the compressible flow.[8]

Finally, the flow reversal in the tapered section of the nozzle discussed at the end of the previous section, can give rise to instabilities which, in turn, may contribute to the formation of satellite droplets due to its close proximity to the forming drop. The finding that flow reversal is independent of liquid compressibility leads to the surprising conclusion that this important drop formation flow feature is not acoustically driven.

Conclusions

A numerical investigation comparing compressible and incompressible flow models was undertaken in order to examine the importance of ink compressibility in DOD nozzle internal operation and drop formation. The maximum pressure generated in the incompressible flow is 10 atm adjacent to the pze wall. The resulting relative change in density is extremely small on the order of 5×10^{-4}. Nevertheless, the very-slightly-compressible flow and the incompressible flow are very different in many aspects of the flow and drop evolution characteristics.

It is concluded that acoustic effects cannot be ignored in this flow system despite the low Mach number and the small condensation. The propagation of pressure along the ink chamber cannot be considered instantaneous relative to the fast motion of the pze wall. Thus, the incorporation of ink compressibility in the physical analysis of this flow system is essential. It should be noted that in some instances it may prove useful to examine as well, specific flow features in the absence of compressibility as a way to determine whether acoustic effects are responsible for that feature. The reversal of the flow field near the nozzle exit may serve as an example in which this type of comparison was employed, leading to the important finding that acoustic phenomena were not responsible for it.

Acknowledgment. We thank Prof. Jonatan Wachtel and Mr. Haggai Karlinski from "Aprion Digital" for many fruitful discussions and for sharing their knowledge with us. We are grateful for the financial support provided by the DPI Magnet program established by Israel Ministry of Industry and Trade. Publication expenses have been funded by the Reimund Stadler Minerva Center for Mesoscale Macromolecular Engineering. Minerva is funded through the BMBF.

References

1. J. D. Beasley, Model for fluid ejection and refill in an impulse drive jet, *Photogr. Sci. Eng.* **21,** 78 (1977).
2. J. Q. Feng, A general fluid dynamic analysis of drop ejection in drop-on-demand jet devices, *J. Imaging Sci. Technol.* **46,** 398 (2002).
3. D. E. Bogy and F. E. Talke, Experimental and theoretical study of wave propagation phenomena in drop-on-demand ink jet devices, *IBM J. Res. Dev.* **28,** 314 (1984).
4. T. W. Shield, D. E. Bogy and F. E. Talke, Drop formation by DOD ink jet nozzle: A comparison of experimental and theoretical simulation, *IBM J. Res. Dev.* **31,** 96 (1987).
5. C. Ping-Hei, P. Hsin-Yah, L. Hsin-Yi, S. L. Chang, T. I. Wu, and C. Chiang-Ho, Pressure response and droplet ejection of a piezoelectric inkjet printhead, *Int'l. J. Mech. Sci.* **41,** 235 (1999).
6. B. V. Antohe and D. B. Wallace, Acoustic phenomena in a demand mode piezoelectric ink jet printer, *J. Imaging Sci. Technol.* **46,** 409 (2002).
7. G. Strang and G. J. Fix, *An Analysis of the Finite Element Method*, Prentice-Hall, Englewood Cliffs, N.J., 1973.
8. E. Magen and M. Gottlieb, Pressure distribution and flow field inside a DOD piezoelectric ink jet nozzle, *J. Imaging Sci. Technol.* in press.
9. E. Magen, *CFD simulations of the flow inside a piezoelectric ink jet nozzle*, M.Sc. Thesis, Ben Gurion Univ., Beer Sheva, Israel, 2003.
10. H. Karlinski and J. Wachtel, Aprion Digital, personal communication, 2001.
11. L. E. Kinsler, A. R. Frey, A. B. Coppens, and J. V. Sanders, *Fundamentals of Acoustics*, 3rd ed., John Wiley and Sons, New York, 1982.
12. R. B. Bird, W. E. Stewart, and E. N. Lightfoot, *Transport Phenomena*, John Wiley and Sons, New York, 2002.
13. *Polyflow User Manual*, Version 3.6.0, Louvain-La-Neuve, Belgium, 1998.
14. L. D. Landau and E. M. Lipshitz, *Fluid Mechanics*, Pengamon Press, Oxford, 1959, pp. 24, for an alternative discussion of this issue.

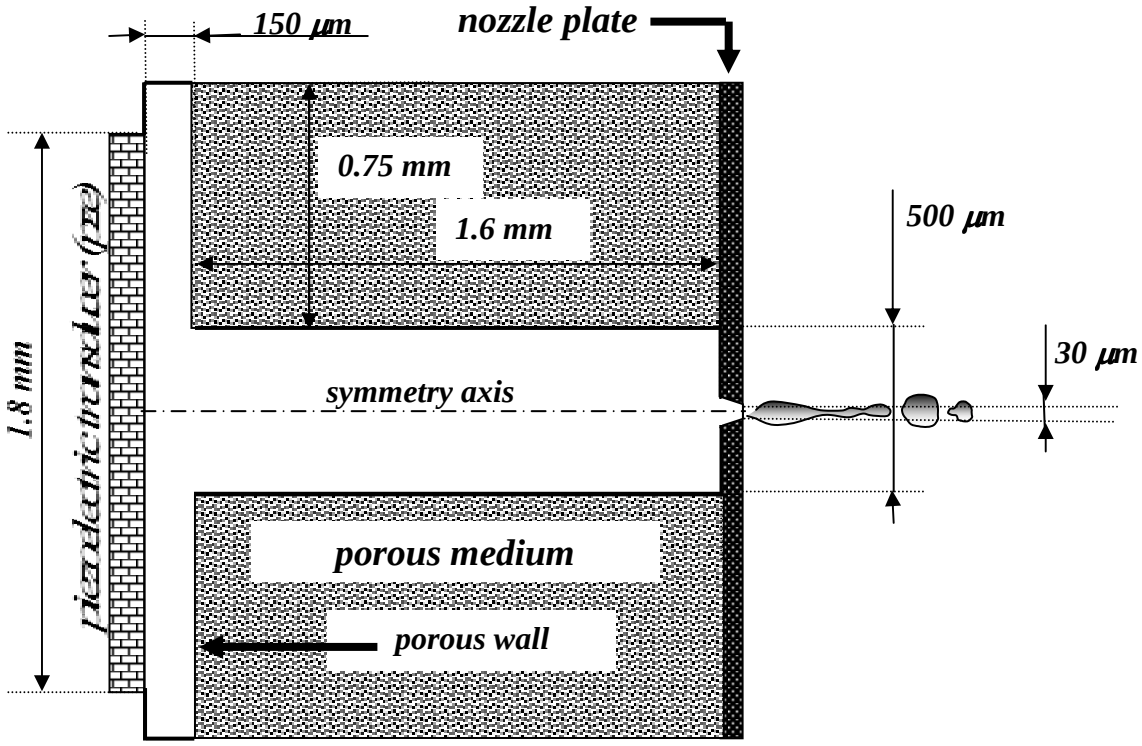
150 μm
nozzle plate
0.75 mm
1.6 mm
500 μm
30 μm
1.8 mm
piezoelectric tube
symmetry axis
porous medium
porous wall

Figure 1

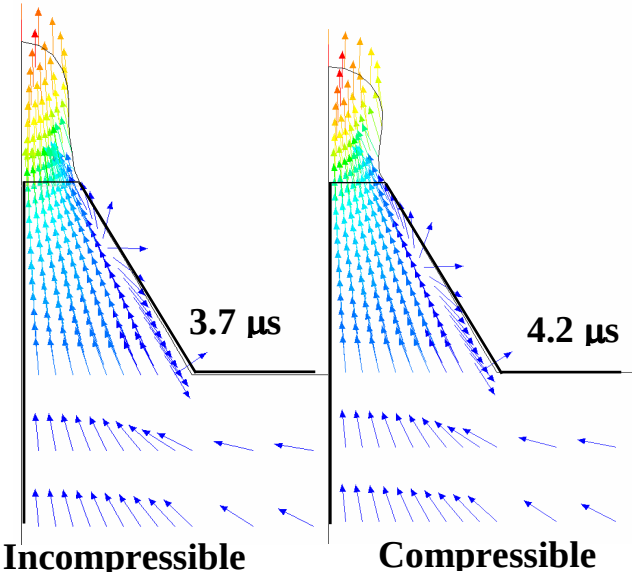

Figure 8

ELSEVIER

Polymer Degradation and Stability 74 (2001) 465–474

Polymer Degradation and Stability

www.elsevier.com/locate/polydegstab

Distribution of a brominated acrylate flame retardant in polypropylene

H. Dvir[a], M. Goldraich[a], M. Gottlieb[a,*], S. Daren[b], J. Lopez Cuesta[c]

[a]*Chemical Engineering Department and Stadler Minerva Center for Mesoscopic Macromolecular Engineering, Ben Gurion University, Beer Sheva 84105, Israel*

[b]*Dead-Sea Bromine Group Ltd, POB 180 Beer Sheva, Israel*

[c]*Centre des Materiaux de Grande Diffusion, Ecole des Mines d'Ales, 6 Avenue de Clavieres, 30319 Ales Cedex, France*

Abstract

Thermal polymerization of pentabromobenzylacrylate (PBBMA) in a polypropylene (PP) composite that contains glass fibers and magnesium hydroxide has been studied using scanning and transmission electron microscopy techniques coupled with energy-dispersive spectrometry. The addition of PBBMA imparts flame retardant (FR) properties to the PP composite but also affects adversely its mechanical properties. It is of practical importance to determine the spatial distribution and the extent of polymerization of the FR in the PP composite in order to understand better its role in the system. The methods presented here allow the distinction between the monomeric and polymeric forms of the FR and to determine their spatial distributions. PP itself shows poor adhesion to the glass fibers, which may be improved by the addition of the reactive PBBMA. The latter is polymerized during reactive extrusion through an antimony-catalyzed reaction. Antioxidant hinders self-thermal polymerization but the presence of antimony overcomes this interference. PP shows good adhesion to sized $Mg(OH)_2$ as expected from a properly surface-treated filler.

Keywords: Polypropylene; Flame retardant; Electron microscopy; Bromine; Energy dispersive spectrometry (EDS); Pentabromobenzylacrylate

1. Introduction

Pentabromobenzylacrylate-(PBBMA) is a crystalline monomer classified as a vapor-phase active flame retardant whose activity is achieved through a halogen radical mechanism. Its chemical structure is shown in Fig. 1a. This type of flame retardant (FR) interferes with the chemical process of combustion. Heat flux formed during combustion is reduced as result of the less energetic reaction of the halogen radical which competes with the combustion enhancing radicals. This in turn reduces the amount of flammable gas fumes that fuel the combustion process [1]. PBBMA is capable of polymerizing by radical polymerization of the unsaturated acrylic group. This polymerization may be initiated thermally during reactive extrusion to produce poly(pentabromobenzylacrylate) (PBBPA) whose structure is shown in Fig. 1b [2]. The thermal properties of PBBMA are shown in Fig. 2. The DSC trace of the monomeric FR (Fig. 2a) shows two endothermic peaks at ~120 °C, which correspond to the melting of two polymorphic crystals, immediately followed by an exothermic thermal polymerization process. The DTGA trace (Fig. 2b) indicates thermal stability up to 290 °C and accelerated breakdown at 330 °C. Due to its stability beyond the processing temperatures of poly(propylene) (PP), generally 210–250 °C, and its degradation at temperatures concurrent with degradation of PP, PBBMA is suitable for use as a FR for PP composites [2]. PP is one of the most versatile and cost-effective polymers available today. It is a semi-crystalline (~60% crystallinity) polymer ($T_m = 160$ °C, $T_g = -8$ ~ −11 °C). At high extrusion temperatures (stable up to ~240 °C), PP may form a tertiary carbo-cation which may undergo oxidation or β-scission [3,4]. PBBMA may react with PP to form either PP-g-PBBPA [2], or attach itself as an end-group to form low molecular weight PP chains. The non-polar nature of the PP hinders its interaction and adhesion to common polar fillers such as magnesium hydroxide or glass fibers. Various types of surface treatments exist for these fillers in order to improve the compatibility with PP and thus its mechanical properties [5]. The grafting of PBBMA may increase the polarity of the PP and thus may

* Corresponding author. Tel.: +972-8-646-1486; fax: +972-8-647-2916.

E-mail address: moshe@inca.bgu.ac.il (M. Gottlieb).

0141-3910/01/$ - see front matter
PII: S0141-3910(01)00169-0

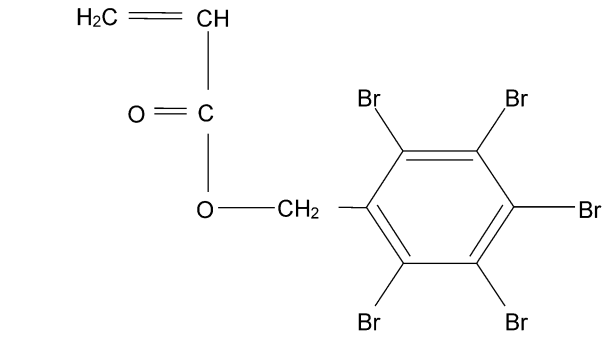

(a)

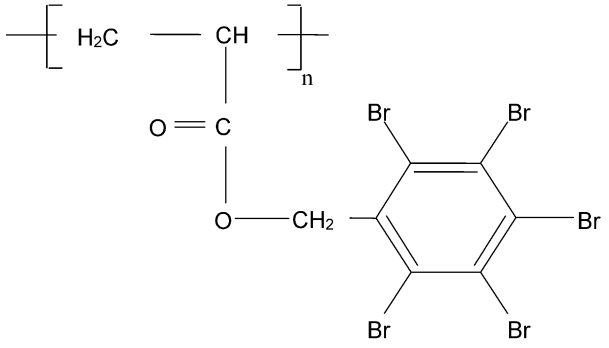

(b)

Fig. 1. Chemical structure of the FR: (a) monomer (PBBMA), (b) polymer (PBBPA).

enhance its adhesion to polar fillers [2], a role which presently is undertaken by modifiers such as maleic anhydride. Although the addition of PBBMA imparts flame retardant properties to the PP composite and possibly, improves its compatibility as discussed above, it also affects adversely the mechanical properties of the composite. Thus, it is of practical importance to determine the spatial distribution of the FR in the PP composite and to determine the extent of its polymerization during extrusion in order to better understand its role in the system. In this paper, we describe two methods for the determination of these variables: (i) spatial distribution is obtained by means of transmission (TEM) and scanning (SEM) electron microscopy coupled with energy-dispersive spectrometry (EDS) and (ii) extent of polymerization is determined by means of Fourier transform infra red (FTIR) microscopy.

In order to obtain the spatial distribution of the FR it is necessary to distinguish between its monomeric and polymeric forms. The double bond distinguishes between the otherwise chemically identical units of PBBMA and PBBPA. Here we developed a method based on the assumption that due to its reactivity, this double bond is selectively stained by osmium tetraoxide (OsO_4). The OsO_4 staining technique has been previously employed in imaging unsaturated polymers such as polyisoprene and polybutadiene [6].

2. Experimental

2.1. Materials

The materials are all technical grade, commercially available and were used as received. A typical formulation was prepared by compounding the following materials:

- Polypropylene (3120MN1, Appryl, France) as the basic polymer matrix;
- PBBMA (FR1025M, DSBG, Israel) as a primary FR;
- Antimony trioxide, masterbatch of 80% Sb_2O_3 and 20% Low Density Poly(ethylene), characteristic diameter 1.5 μm (L0112 Kafrit, Israel) as an FR synergistic additive that enhances the FR properties via a different radical mechanism. For optimal FR activity [5], it is added in 1:3 ratio Antimony to PBBMA;
- Irganox (B225, blend of Irganox 1010-hindered phenol type and Irgafos 168-phosphate type, Ciba Giegy, Germany) an antioxidant, in order to prevent PP oxidation during compounding (the commercial PP above contains ~800 ppm of this antioxidant);
- Magnesium Hydroxide, (FR20, DSBG, Israel) as a filler with flame retardant properties, a secondary FR coated with 2% stearic acid;
- Chopped glass fibers characteristic length 4.5 mm and characteristic diameter ~10 μm, $d = 2.6$ g/cm^3 (P355, Vetrotex, France) as a primary filler, in order to improve mechanical properties; the fiber surface is treated with silane-based coupling agent for better compatibility with PP;
- Maleic anhydride (Exxelor VM42E, Exxon, USA) $d = 0.9$ g/cm^3, used as a compatibilizer, grants the PP a somewhat polar nature;
- Poly(ethylene) wax (AC-6A, Allied, USA) added in order to lower sheer stresses developed during extrusion.

A 4% OsO_4 aq. solution (Aldrich, USA) was employed for selective staining of the FR double bond.

2.2. Formulation

All formulations were compounded in a twin screw extruder (Berstorff ZE25 co-rotating, open vent, extruder

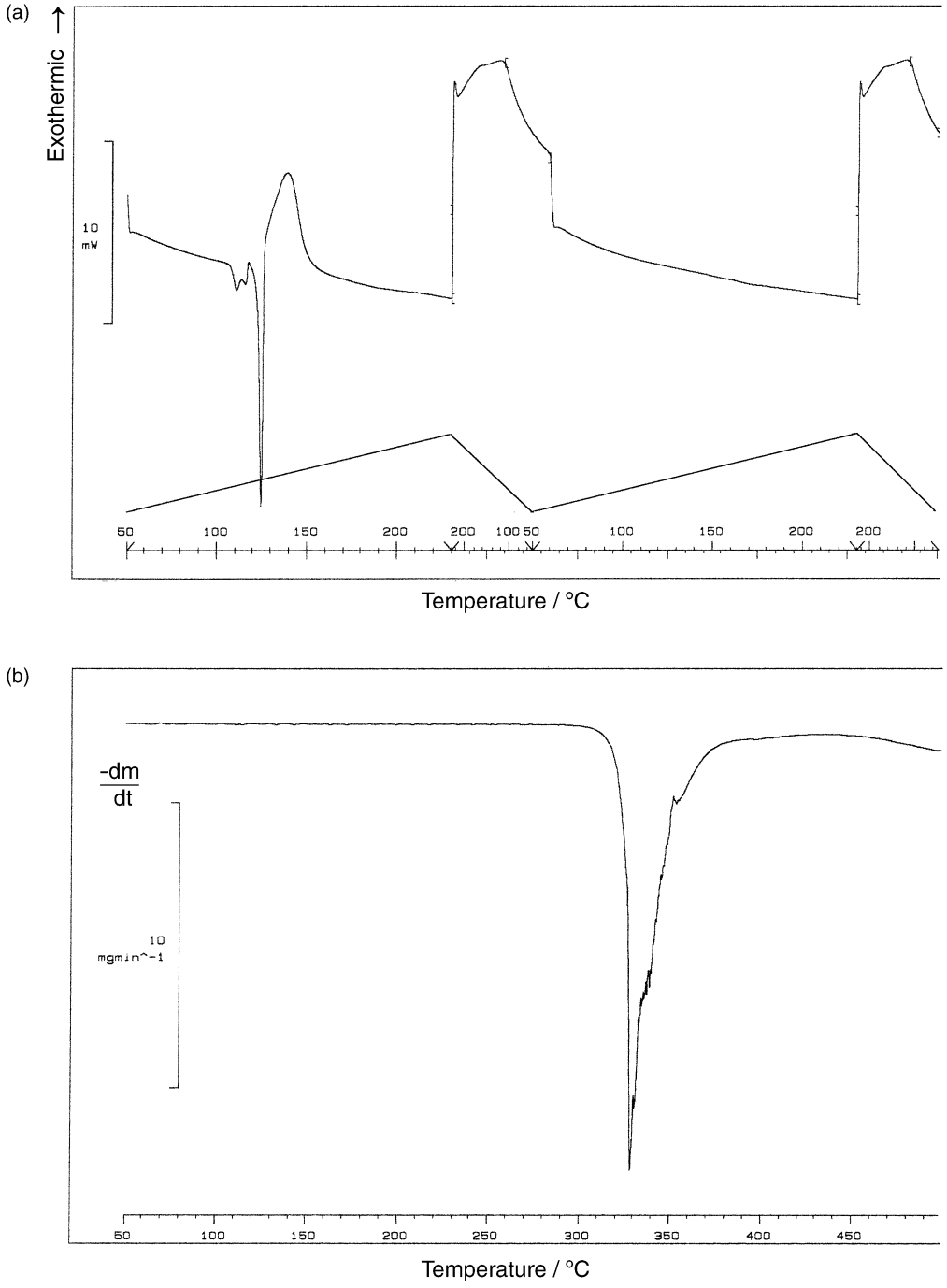

Fig. 2. Thermal properties of PBBMA. (a) DSC thermogram of PBBMA. The thermogram describes heating cycle (at 5 °C/min) from 50 to 230°C, fast quench to 50 °C, followed by a second heating cycle. In the first cycle two melting endotherms (110 °C, 123 °C) followed by polymerization exotherm (onset 125 °C) are observed. In the 2nd cycle no features are detected for the amorphous PBBPA. (b) DTGA analysis of PBBMA. Figure depicts mass-loss rate as function of temperature (heated at 10 °C/min). Onset of mass loss is at 290 °C and maximal rate at 330 °C.

L/D = 32) at 250 °C, (the angular velocity of the screws rotation was 350 rad/min) and subsequently pelletized. The pellets were dried overnight. The formulations were injected by means of Arburg Allrounder 320S injection molding machine into 'dog- bones'. A Nozzle temperature of 240 °C and an injection pressure of 1300 bar were employed. The formulations are specified in Table 1.

2.3. FTIR microscopy

The samples were cut into ~40 μm thick slabs by means of a Microm HM355 rotary microtome (feed range of 0.25–500 μm) at room temperature. The samples were examined in transmission mode in 600–4000 cm^{-1} range using Bruker FTIR microscope (Equinox 55

Table 1
Formulations of polypropylene composites (in wt.%) and flame retardant properties

	Sample 1	Sample 2	Sample 3	Sample 4
Polypropylene	60	60	43.5	46.5
PBBMA	30	29.7	14	14
Antimony oxide	10	10	4.6	4.6
Antioxidant (Irganox B225)		0.3	0.3	0.3
Glass fibers			25	20
Magnesium hydroxide			11.4	13.4
Maleic anhydride			1	1
PE wax			0.2	0.2
UL94 VB	V-0	V-0	Non rated	Non rated
LOI-limiting oxygen index (LOI, PP ~ 18)			24–24.5	23.5–24

spectrometer, IR scope II microscope with 15× magnification, IR objective and MCT detector, liquid N_2 cooled). Interferograms were collected by OPUS FTIR software. Interferograms were deciphered and examined using Omnic FTIR software.

2.4. Microscopy

2.4.1. SEM + EDS

The samples were cut into cube shaped pieces of 2-mm edge size. Each piece was held for 3 days in a desiccator over the OsO_4 solution. After staining, the samples were prepared for SEM analysis by gold coating using Polaron 5100 coater. The samples were examined using a Jeol JSM35CF scanning electron microscope operated at 25 kV, coupled with EDS using an Oxford detector and AN10000 analyzer. EDS analyses have been carried out in two modes: mapping an element over the entire sample or zooming-in at a particular spot in the micrograph and collecting the overall spectra. An example is shown in Fig. 11 to be discussed later. In this figure, the largest peaks correspond to bromine (from the FR) and magnesium [from $Mg(OH)_2$ particle]. Gold is due to the surface coating for SEM, silicone is due to the glass fiber. Traces of Os are also detected in this sample.

2.4.2. TEM + EDS

For TEM microstudy, after staining, 50 nm thick slabs were cut with glass knives by means of Reichert-Jong model FC4E Ultracut cryo-ultramicrotome at a temperature of −100 °C. The slabs were placed on 200 mesh microscope copper grids and restored to room temperature. The samples were examined using CM120 Philips transmission electron microscope operated at 120 kV equipped with CCD camera mounted beneath the sample. Electron micrographs were processed using Gatan's Digital Micrograph software and further processed if necessary by Adobe PhotoShop software. The stained samples were also examined by EDS operated at 100 kV in a 2000 FX JEOL TEM.

3. Results and discussion

3.1. FTIR measurements

The collected interferograms were deciphered and two distinct peaks were chosen as reference values to PBBMA and PBBPA. A carbonyl stretching-mode peak at about 1720 cm^{-1} is a common peak corresponding to both PBBMA and PBBPA. A vinyl stretching-mode peak at ~1405 cm^{-1} corresponds solely to PBBMA (cf. Fig. 3). We have found the peak size to depend on the macroscopic sample variables (such as exact thickness, flatness, etc.), but the ratio values between the areas under different peaks (indicated in Fig. 3) were found to be independent of the sample surface and thickness and represents only its composition. The ratio between the chosen peak areas (after conversion into respective mass based on previously determined calibration) shows the fraction of monomer that did not polymerize during extrusion, i.e. residual monomer. This information allows the calculation of the conversion of PBBMA to PBBPA, as shown in Table 2. Two representative interferograms corresponding to samples 1 and 3 are depicted in Fig. 3. From the comparison between samples 1 and 2, one can deduce the role of the antioxidant Irganox. The incorporation of this antioxidant, which is a radical scavenger, may interfere with the polymerization of the FR in the composite. In sample 1 that contains no Irganox, the vinyl peak does not show up at all in the interferogram which means PBBMA has polymerized completely during compounding. Whereas in sample 2 to which Irganox has been added, PBBMA polymerization has been largely inhibited. This effect is also observed in samples 3 and 4. The smaller differences in conversion between samples 2, 3, and 4 are due to variations of the composition and relative amounts of additional solid ingredients which influence the polymerization rate.

Additional experiments have been carried out to examine the homogeneity of the FR distribution throughout the sample. A cross-sectional cut of the 'dog-bone' formed from Sample 3 was examined and

Table 2
PBBMA conversion as determined by FTIR microscopy

Formulation no.	PBBMA compounded (wt.%)	PBBMA in product (wt.%)	PBBMA conversion (%)
1	30.0	~0	~100
2	29.7	19.6	34.1
3	14.0	10.1	28.1
4	14.0	7.7	45.1

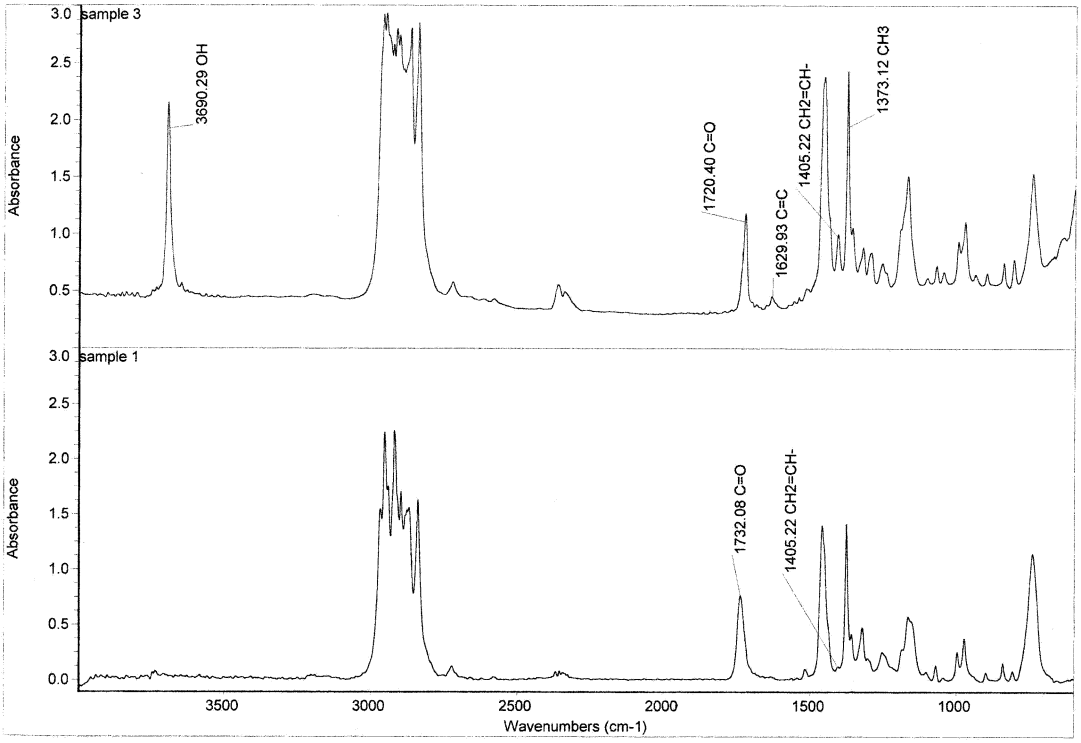

Fig. 3. Interferograms of samples 1 and 3. Assignments for the main peaks are indicated.

FTIR spectra have been collected at 10 points, 0.5 μm apart along a line stretched along the cross-section from the sample edge to its center. At each point the ratio between the carbonyl and vinyl peaks (which corresponds to the total-FR/PBBMA ratio) and the ratio between the vinyl (PBBMA) peak and a peak corresponding to the PP (–CH_3 symmetrical deformation mode at $\sim$1370 cm^{-1}) were measured. At all points except for the edge point, the obtained ratio values were within the experimental error 5% . The edge point differed significantly from the other points but this is attributed to the inaccurate measurement at the edge as result of surface irregularities. From these experiments, we conclude that the FR is evenly distributed in the PP matrix and the extent of polymerization is identical throughout the sample.

3.2. TEM morphological microstudy

In Figs. 4 and 5, TEM micrographs of samples 1 and 2 respectively, are shown. In both micrographs, the polypropylene matrix appears as the whitish background. This is confirmed by the EDS analysis, which indicates the complete absence of any heavy elements (Br, Os) in this region. The black dark spots have been identified as antimony oxide by the distinct peak observed in EDS spectra. In the gray areas, a peak of bromine is detected indicating the presence of the FR, either in its monomeric or polymeric form. Two types of gray areas exist in Fig. 4: areas enclosing Sb_2O_3 particles and areas with no trace of antimony. In both cases OsO_4 was not detected. Furthermore OsO_4 was not detected anywhere in this sample. In contrast, OsO_4 is detected in Fig. 5, but only in the gray areas that are relatively removed from the antimony particles. The presence of OsO_4 in these gray areas exposes the PBBMA (which contains an unsaturated bond capable of interacting with the OsO_4) whereas gray areas with no detectable OsO_4 contain mostly PBBPA. Hence, the combined TEM and EDS analysis allows the distinction between PBBMA and PBBPA regions. The role of the Irganox B225 in the composition is clearly deduced from the comparison of the two figures and supports our earlier observations by FTIR described above. As previously shown, the Irganox antioxidant suppresses the polymerization of the PBBMA during extrusion. In sample 1 (Fig. 4) which contains no Irganox, more PBBMA has polymerized either by self-thermal polymerization (areas without Sb_2O_3) or by Sb_2O_3 catalyzed reaction (in areas around antimony). Addition of Irganox B225 (Fig. 5) suppresses mostly the self-thermal polymerization and as a result, monomer (detected by OsO_4) is found in large amounts in the isolated FR regions. In contrast, in the regions in the vicinity of Sb_2O_3 the catalytic activity of the latter overcame the hindrance of the Irganox and the FR has polymerized (no OsO_4).

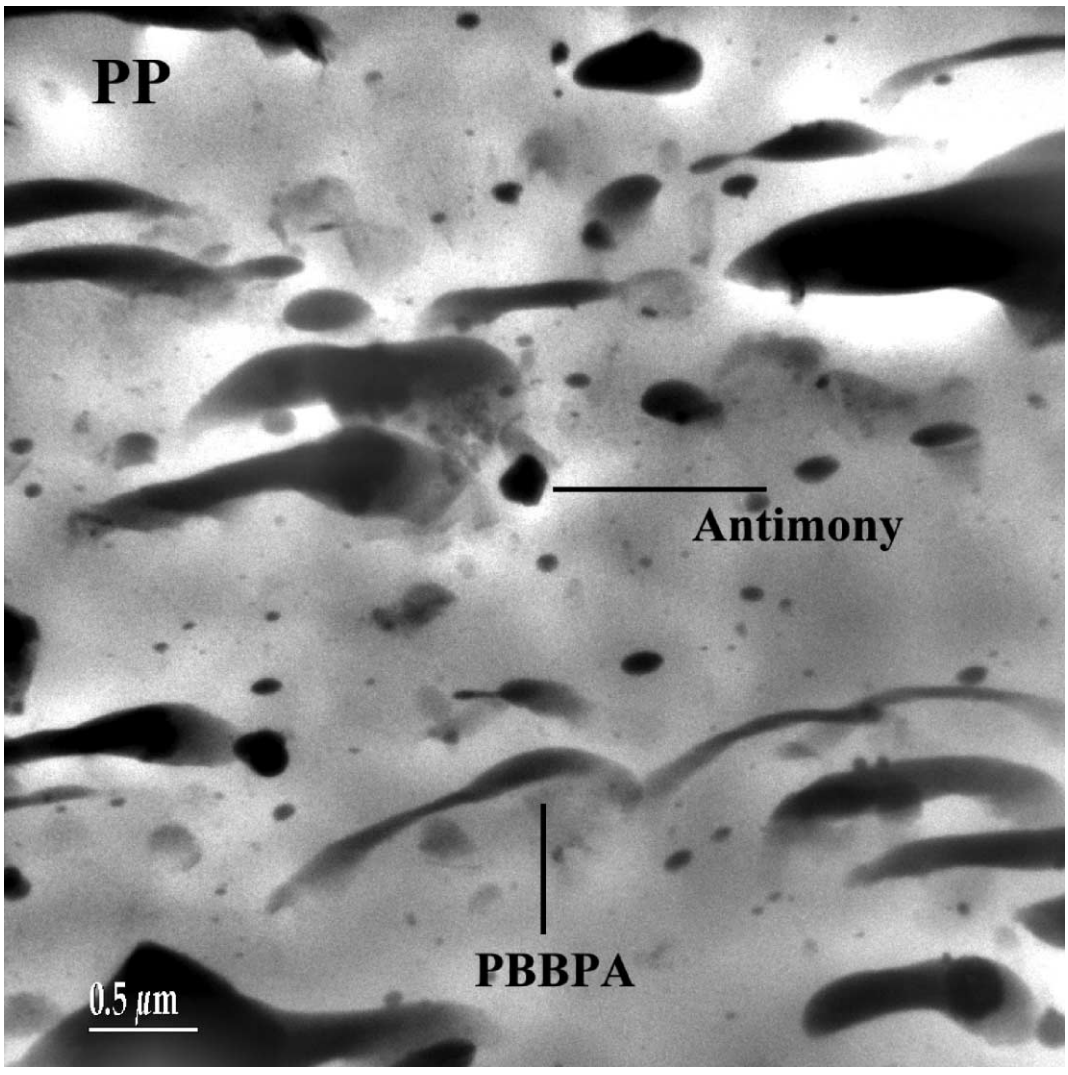

Fig. 4. TEM micrograph of sample 1. White background, PP; dark black spots— antimony; grey areas, PBBPA. No PBBMA is detected here.

3.3. SEM morphological microstudy

In Figs. 6 and 7 SEM micrographs of samples 2 and 3 respectively are shown. In both micrographs the PBBMA particle appears as a white bright spot. A distinct peak of bromine and osmium was observed by EDS at this particle. Small particles that are embedded in PP layers were identified by EDS as Sb_2O_3. It can be seen that Sb_2O_3 is dispersed homogeneously throughout the PP matrix. EDS spectra at the vicinity of the Sb_2O_3 particles show the presence of bromine without osmium identifying it as PBBPA. Once again, the combined SEM and EDS analyses allow the distinction between PBBMA and PBBPA. As shown before, the Sb_2O_3 plays the role of a catalyst for the polymerization of the monomer. Polymerization does not occur relatively far from Sb_2O_3 particles. Sb_2O_3 is a FR synergistic additive that enhances the flame retardation properties of the polymeric system. The encapsulation of Sb_2O_3 by PBBPA is ideal for this purpose. The dispersion of the PBBPA with the antimony in the PP matrix is expected to increase the efficiency of the FR [7]. It has been suggested that the difference in viscosity and hence the flowability of the FR relative to the PP may damage its efficiency, but when the FR is embedded in PP, they must flow together. PBBMA particles appear in Figs. 6 and 7 to be undissolved in the PP matrix, whereas the polymerized PBBPA around Sb_2O_3 is better dispersed in the PP phase. A third type of particle has also been observed. These particles that are partially embedded in the PP matrix contain antimony, bromine and osmium. This means that PBBMA has only partially polymerized. Since it does not dissolve in the PP it forms a separate phase that is drawn toward the PP phase by the polymerized fraction of the particle. In this case, the ability of the PP and the PBBMA to flow together is improved.

In Figs. 8 and 9, SEM micrographs of samples 3 and 4 respectively are shown. Chopped glass fibers are imaged

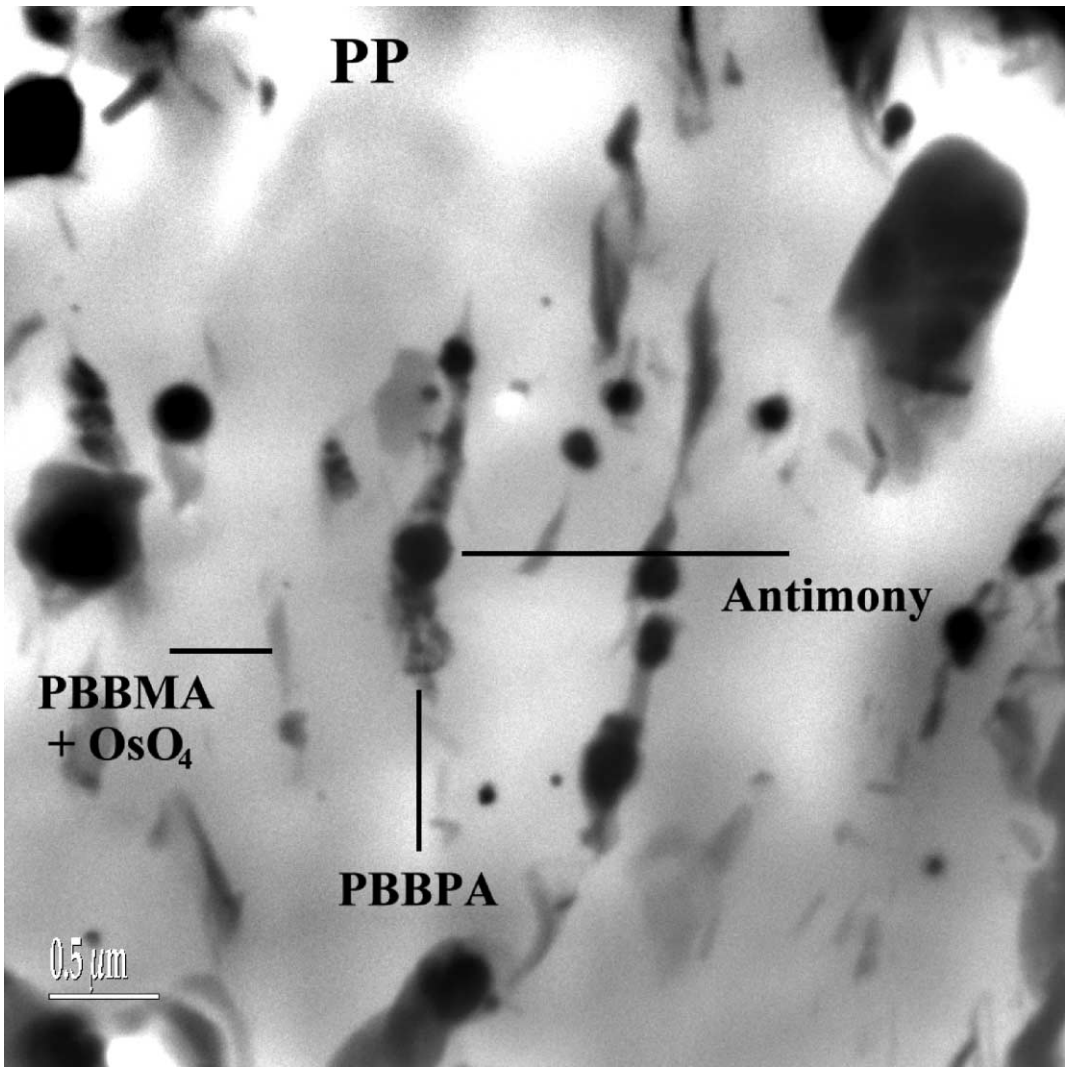

Fig. 5. TEM micrograph of sample 2. White background, PP; dark black spots, antimony, gray areas enclosing antimony particles, PBBPA; other gray areas—PBBMA.

in both micrographs. EDS analysis revealed that the small 'spots' observable on the glass fibers and indicated by an arrow in both figures, contain only bromine. In contrast, the larger particles, also observed on the fiber in Fig. 9, contain osmium as well. In addition to the 'spots' and particles an elongated fibrillar feature is also observed attached to the glass fiber in Fig. 9. From elemental analysis as well as from the size and shape of the fibril, we are able to identify this fibril as composed of mostly PP with traces of bromine near its base (attachment area to the glass fiber).

From these figures, it is possible to conclude the following: (a) The relatively bare surface of the glass fibers indicates that there is poor adhesion between the PP and the glass fibers despite the surface treatment with the silane-based coupling agent. (b) The small spots that contain bromine suggest that a reaction may have taken place between the reactive FR monomer and a functional group on the fiber surface. The lack of osmium also indicates that this reaction is probably part of the FR polymerization process. (c) In the larger particles, the polymerization is incomplete and the osmium identifies the presence of PBBMA in the proximity of the surface. (d) The bromine identified near the base of the fibril suggests that the reactive FR monomer acts as a binder, a coupling agent between the PP and the sizing agent on the surface of the glass fiber. A possible coupling mechanism is based on the formation of a chemical bond between the silane surface treatment and PBBMA and between the latter and PP. The existence of such a bonding is beneficial for the dispersion of stress loads developed along the interface between PP and glass fibers in the composite and the improvement of its mechanical properties.

In Fig. 10, which depicts an SEM micrograph of sample 3, a magnesium hydroxide particle is observed.

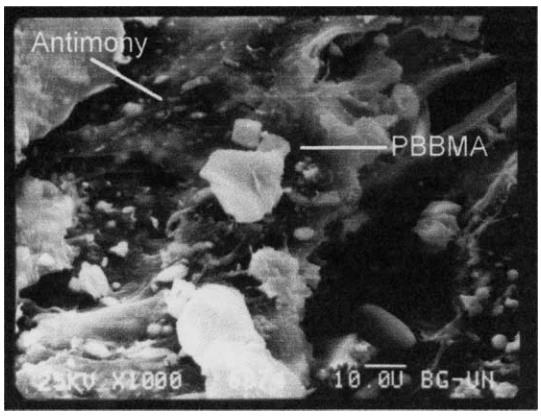

Fig 6. Scanning electron micrograph of sample 2. White PBBMA particle is identified in the micrograph. Small antimony particles are also indicated.

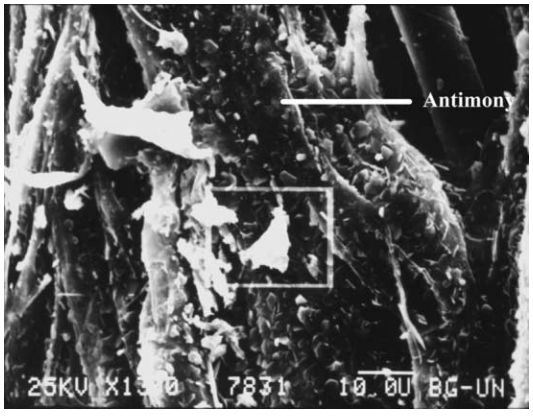

Fig 7. Scanning electron micrograph of sample 3. This sample contains glass fibers. White particle inside the white square is a PBBMA particle. Small antimony particles are indicated.

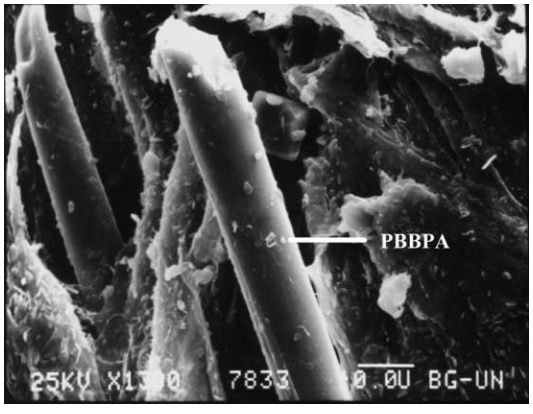

Fig 8. Scanning electron micrograph of sample 3. No PP adhesion to the glass fiber is observed. Small spots are identified as PBBPA.

This identification is based on the detection of magnesium by EDS as shown in Fig. 11. The original magnesium hydroxide particles have a characteristic diameter of ~1.5 μm and are surface treated with 2 wt.% stearic

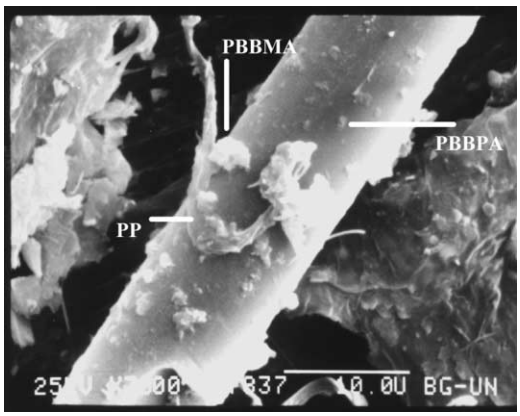

Fig 9. Scanning electron micrograph of sample 4. In this image PBBPA spots, PBBMA particle, and a PP fibril are observed. PBBPA is detected at the base of the fibril near the glass fiber.

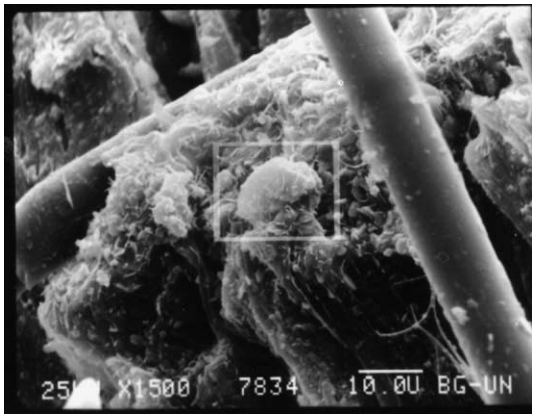

Fig 10. Scanning electron micrograph of sample 3. The particle marked by the frame is magnesium hydroxide. It is covered by PP and contains bromine in its shell.

acid. The particle observed has a diameter of about 10 μm and EDS spectra shows also the presence of large amounts of bromine. Thus, the particle is encapsulated by a spherical PP shell which also contains PBBPA on its surface [8]. Traces of osmium are detected but their relatively small amount precludes the presence of considerable amounts of PBBMA in the particle. The $Mg(OH)_2$ shows good adhesion to PP and is embedded in the polymer matrix. The successful incorporation of the magnesium hydroxide particles in the polymer is desirable from the point of view of flame retardance since the embedded particle will be carried by the flowing PP during combustion and will not separate from the matrix upon melting. The $Mg(OH)_2$ also shows good adhesion to the reactive FR, which may further improve its flame retarding properties. This may explain the lower required amounts of brominated FR when combined with $Mg(OH)_2$ in the same composite [9].

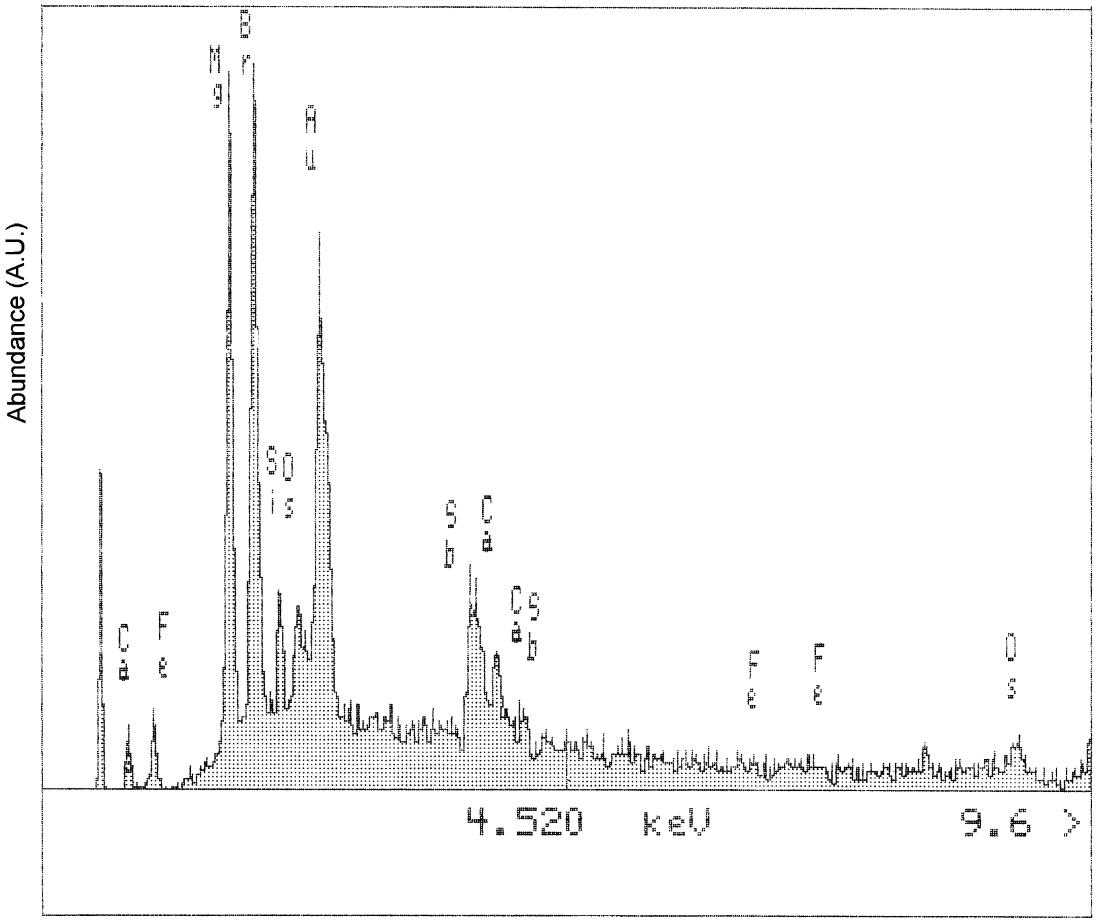

Fig 11. EDS spectra of the framed section in Fig. 10 (magnesium hydroxide particle).

4. Conclusions

A powerful method has been developed for the visualization of pentabromobenzylacrylate in polypropylene composites and the identification of the monomeric and polymeric forms of this flame retardant. It allows the study of the distribution of the FR in the composite by means of SEM and TEM coupled with EDS. The ability to distinguish between the monomeric and the polymeric forms of the FR is based on the use of OsO_4 as a selective staining reagent.

In a typical PP composite studied here we observe that the residual monomer is undissolved in the composite, whereas the polymeric FR is homogeneously dispersed in PP matrix. By the combination of the electron-microscopy methods and FTIR microscopy it was determined that the polymerization reaction is highly hindered by the presence of the antioxidant and takes place only in the presence of antimony oxide.

Poor adhesion is observed between PP and the glass fibers. Better adhesion is observed for the polymerized FR. The poor adhesion of PP may be improved by the reactive FR monomer that seems to play the role of a coupling agent. PP shows good adhesion to $Mg(OH)_2$ as expected from a surface treated filler and it allows the polymerization of the FR in its vicinity.

Acknowledgements

This work has been financially supported by the Ariel program for French-Israeli cooperation. We are grateful to V. Erukhimovipch (BGU Institute for Applied Biology), Y. Yagen (Minerva Labs) and Y. Cernomerdic (DSBG) for their help in FTIR Microscopy and analysis, L. Soifer for help in carrying out DSC and TGA experiments, A. Kiriaty for help in SEM/EDS imaging.and Dr. O. Regev for helpful comments.

References

[1] Mark HF, Bikales N, Overberger CG, Menges G, editors. Encyclopedia of polymer science and engineering, Vol. 7: Flammability. 2nd ed. New York: John Wiley & Sons, p. 154–210.
[2] Muskatel M, Utevski L, Shenker M, Daren S, Peled M, Charit Y. J Appl Polym Sci 1997;64:601–61.

[3] Cartier H, Hu GH. Polym Eng Sci 1998;38:177–85.
[4] Clavons M, Carlier V, De Roover B, Franquinet P, Legras R. J Appl Polym Sci 1996;62:1205–10.
[5] Katz HS, Milewski JV, editors. Handbook of fillers for plastics. New York: Van Nostrand Reinhold Company, 1987. p. 279–291.
[6] Sawyer LC, Grubb DT, editors. Polymer microscopy. 2nd ed. London: Chapman and Hall, 1996. p. 83–173.
[7] Chang EP, Kirsten R, Salovey R. Polym Eng Sci 1975;15:697–702.
[8] Gutman E, Bobovitch A, Pinski A, Utevski L, Sondak D, Muskatel M. J Thermal Anal 1996;46:1541–61.
[9] Bobovitch A, Gutman E, Schenker M, Utevski L, Muskatel M. Mater Lett 1995;23:317–20.

Investigation of Micelle Formation by Fluorescence Correlation Spectroscopy (FCS)

Heiko Zettl[1,*], Yariv Portnoy[2], Moshe Gottlieb[2], Georg Krausch[1]

[1] *Physikalische Chemie II, Universität Bayreuth, 95440 Bayreuth, Germany*

[2] *Department of Chemical Engineering, Ben Gurion University of the Negev, 84105 Beer-Sheva, Israel*

Abstract

We show that non-covalently bound dye molecules can be used as labels in single molecule fluorescence experiments for the determination of aggregate formation in standard surfactant systems. Aqueous solutions of AOT, CTAC, and $C_{12}E_5$ have been studied by Fluorescence Correlation Spectroscopy (FCS) using commercially available dyes. The translational diffusion coefficient and the critical micelle concentrations (*cmc*) have been determined and compare well to values reported in literature. The respective charges of the surfactant and of the dye molecule are crucial for the effectiveness of the presented method.

1 Introduction

Self-aggregation of surfactants is a key issue in a variety of industrial processes such as cleaning, pharmaceutical formulation, and polymerisation. In this context, precise knowledge of the size of the aggregates and a quantitative determination of the critical micelle concentration (*cmc*) is indispensable. Usually data is drawn from light scattering, surface tensiometry, or conductivity and osmotic pressure measurements [1]. These techniques, however, are limited in sensitivity, need considerable amounts of material, and are highly costly and time consuming. Here we explore the potential of fluorescence correlation spectroscopy (FCS) as an alternative method to characterise the self aggregation behaviour of surfactants, using a non-covalently attached dye as fluorophore.

Previous FCS studies of surfactant systems relied on the synthesis of dye-labelled molecules, which were blended with the bare molecules under consideration [3, 4]. This establishes a major disadvantage, since the labelling process is extremely costly and time consuming. Therefore FCS has not been very common in surfactant analysis so far. Covalent binding of the dye may, however, not be necessary. Depending on the respec-

tive polarities of the surfactant head group and the dye, one can anticipate physical aggregation of the dye to the micelle. In the present contribution, we systematically study the ability of free dye molecules to act as a label in aggregate-forming systems. We show that a suitable choice of commercially available dyes allows a straightforward determination of both the aggregate size and the critical micelle concentration. Our results compare well to values determined by the "classical" techniques mentioned above.

Since FCS is based on single-molecule fluorescence-detection, this technique provides both extreme sensitivity and access to a large range of concentrations, which exceeds that of different techniques by orders of magnitude [2]. The small focus volume of around 1 fl, which is addressed by FCS, permits the use of only smallest amounts of material. Moreover, the fastness of the experiments makes them well suited for high throughput investigations.

2 Experimental

2.1 Fluorescence Correlation Spectroscopy

The basics of FCS were developed in the early 1970s by Elson and Madge [5, 6, 7]. The diffusion of a single molecule is measured by monitoring its fluorescence upon diffusion through a microscopically small volume defined by a highly focussed laser beam. From the average time needed to pass this volume, the hydrodynamic radius can be inferred. Particles of different mobility, in our case single dye molecules and dye molecules bound to a micelle, are easily distinguishable.

The experiments were performed with a ConfoCor2 FCS setup (Carl Zeiss Jena), using an argon-ion laser at a wavelength of 514 nm for excitation of the dye molecules. The laser beam is focussed by a C-Apochromat 40× water immersion objective with a numerical aperture of 1.2. The fluorescence light is collected by the same objective and separated from the excitation beam by a dichroic mirror. The emission beam is then mapped onto a pinhole in the image plane of the objective. Emmission filters in front of the pinhole absorb scattered light from the excitation laser. Fluorescence is detected by an avalanche photodiode in single photon counting mode. The experimental setup of FCS is given in detail by Elson [6]. All experiments were performed at room temperature without further temperature control.

Comparison of the fluorescence with diffusion-based models can most conveniently be done by analysing the autocorrelation of the fluorescence signal. For this purpose, a software correlator yields the autocorrelation function $G(\tau)$:

$$G(\tau) = \frac{\langle F(0) \cdot F(\tau) \rangle}{\langle F \rangle^2}, \qquad (1)$$

where F indicates the fluorescence intensity at times 0 and τ and where $\langle\ \rangle$ denotes the time average. For the modelling of the autocorrelation function we assume a Gaussian

intensity profile of the laser beam with waist radii w_{xy} and w_z perpendicular and along the optical axis, respectively.

$$I(x,y,z) = I_0\, e^{-\frac{2(x^2+y^2)}{w_{xy}} - \frac{2z^2}{w_z}} \qquad (2)$$

If we allow for K fractions of fluorophores with different mobilities (e.g. free dye molecules or dye molecules bound to aggregates of different sizes), the autocorrelation function $G(\tau)$ is given by [9]

$$G(\tau) = \frac{1 + \frac{T}{1-T}\cdot e^{-\frac{\tau}{\tau_{tr}}}}{N} \cdot \cdot \sum_{i=1}^{K} \frac{\phi_i}{1+\frac{\tau}{\tau_i}} \frac{1}{\sqrt{1+\frac{\tau}{S^2\cdot\tau_i}}} + 1, \qquad (3)$$

where τ_i is the average time needed by the dye molecules of fraction i to pass the excitation volume. T denotes the fraction of dye molecules that are in the triplet state with a lifetime τ_{tr}. N is the average number of dye molecules within the excitation volume and ϕ_i is the fraction of the i^{th} component. Finally, S is the structure parameter, which describes the shape of the excitation volume and which is defined as the ratio of the waist radii

$$S = \frac{w_z}{w_{xy}}, \qquad (4)$$

The diffusion times are related to the respective diffusion coefficients D_i

$$\tau_i = \frac{w_{xy}^2}{4\cdot D_i}, \qquad (5)$$

which then allow us to calculate the hydrodynamic radii $r_{h,i}$ by use of the Stokes-Einstein equation

$$r_{h,i} = \frac{k_{\text{B}}T}{4\pi\eta_0 D_i}, \qquad (6)$$

with k_{B} the Boltzmann constant, T the absolute temperature and η_0 the solvent viscosity.

2.2 Data Analysis

For quantitative data analysis equation (3) is fitted to the experimental autocorrelation function. The fits are performed by using a Levenberg-Marquardt algorithm. To determine the geometry of the laser focus, we first measure an aqueous solution of Rhodamin 6G. A single-particle fit ($K = 1$) yields the structure parameter S. Using the published value for the diffusion coefficient of Rhodamin 6G of $2.8 \cdot 10^{-10}$ m^{2}s^{-1}, we can estimate $w_{xy} \approx 200\,$nm according to equation (5). For the fitting of all subsequent measurements S is kept constant. To determine whether a single-particle fit ($K = 1$) is sufficient or whether a two-particle fit ($K = 2$) is required, a statistical F-test was performed [11].

2.3 Sample Preparation

In our experiments, three surfactants, hexadecyltrimethylammonium chloride (CTAC), sulfosuccinic acid bis(2-ethylhexyl) ester sodium salt (AOT), and pentaethylene glycol monododecyl ether ($C_{12}E_5$) were used as purchased from Fluka. The dyes Sulforhodamine G, Sulforhodamine B and Rhodamin B Base were purchased from Sigma-Aldrich GmbH. Rhodamin 6G and Cresyl Violet were obtained from Lambda Physics. The exact

dye concentration in the delivered powder is unknown for most of the dyes. All chemicals were used without further purification. The solutions were prepared with Milli-Q water. The same water was used as immersion medium for the objective.
All surfactant solutions were prepared with a dye concentration of 10^{-8} M. The FCS measurements were performed on droplets of 40μl placed onto a coverglass. The focus of the objective was placed $200\,\mu m$ above the coverglass to avoid interactions between the glass surface and the investigated molecules. Each FCS measurement (duration: 60 s) was repeated three times.

3 Results

Cationic surfactant. The cationic surfactant CTAC was measured with the anionic dyes Sulforhodamine B and Sulforhodamine G and the cationic dye Cresyl Violet. We start discussing the results obtained with the anionic dyes. Figure 1A shows two typical autocorrelation functions for CTAC concentrations of $8.0 \cdot 10^{-4}$ M and $1.5 \cdot 10^{-3}$ M, respectively. Figure 2 (top) shows the diffusion time as a function of CTAC concentration obtained by single-particle fits throughout the entire concentration range. The dashed vertical line indicates the published value of the *cmc* obtained using "classical techniques". We observe an increase of the diffusion time starting at a surfactant concentration of $5.0 \cdot 10^{-4}$ M, i.e. at a concentration considerably below the *cmc*. Note that a single-particle fit assumes all dye molecules to

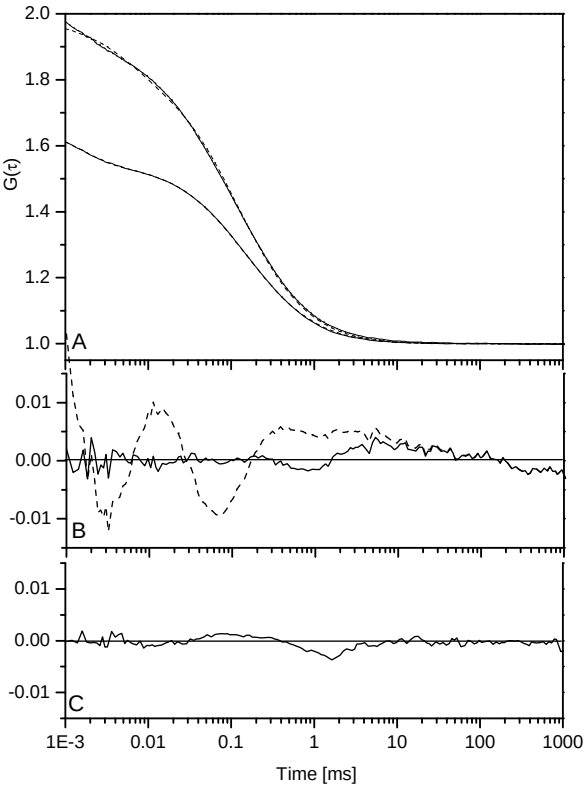

Figure 1: The experimental autocorrelation curves (—) of the two CTAC concentrations $8.0 \cdot 10^{-4}$ M and $1.5 \cdot 10^{-3}$ M with an amplitude of 2.0 and 1.6 are plotted together with the single-particle fit (– – –) in part A. Part B represents the residuals of the single particle and two-particle fits at a CTAC concentration of $8.0 \cdot 10^{-4}$ M, respectively. The residuals of the single-particle fit (– – –) are considerably larger than the ones of the two particle-fit (—). In part C the residuals of the single-particle fit to the data at $1.5 \cdot 10^{-3}$ M are shown. For this concentration a single-particle fit is sufficient.

diffuse at the same average speed. In case of aggregate formation this implies that all dye molecules have associated to aggregates of the same size. In order to check whether different fractions of dye molecules are present in the solution, the autocorrelation functions were also fitted with a two-particle model ($K = 2$) and an F-test was applied to determine which of the two models is more suitable to represent the experimental data. The main criterion of the F-test is the value of χ^2, which leads to an intuitive understanding of the F-test; only if the residuals (and thus χ^2) are significantly lowered, the complicated model is justified. For c(CTAC) = $8.0 \cdot 10^{-4}$ M χ^2 is 0.015 for the single-particle fit and 0.00075 for the two-particle fit. This means that the two-particle model improves χ^2 by a factor of twenty and therefore is the model to be chosen. Not very surprisingly, also the F-test recommends the two-particle model. Repeating this procedure for the whole concentration range, it turns out that for the CTAC system a two-particle fit is needed between $5.0 \cdot 10^{-4}$ M and the *cmc* resulting from classical techniques. Below and above this concentration range, a single-particle fit is sufficient. To further visualise this procedure, we compare in figure 1B the residuals of a single-particle and a two-particle fit to an autocorrelation function obtained in the intermediate concentration regime. Here, the two-particle fit clearly leads to smaller residuals. In figure 1C, we show the residuals for a single-particle fit to an autocorrelation function obtained above the *cmc*. Here, the residuals are considerably smaller and a two-particle model does not lead to a significant improvement. Figure 2 (bottom) shows the results for the diffusion times resulting from two particle fits in the intermediate CTAC concentration regime.

The two particles represent the free dye molecule (dominant at low CTAC concentrations) exhibiting a diffusion time of $\tau_1 \approx 30\mu$s and a dye molecule bound to a micelle (dominant at high CTAC concentrations) exhibiting a diffusion time of $\tau_2 \approx 150\ \mu$s. This value is nearly constant up to a CTAC concentration of $1.5 \cdot 10^{-3}$ M. At intermediate concentrations slightly below the *cmc*, both free dye molecules and dye molecules bound to micelles coexist. The diameter of the micelles calculated from τ_2 according to equations (5) and (6) yields 6.3 nm. This is in good agreement with the value of 7.9 nm reported by Lindman and coworkers [12]. Figure 3 shows the increase of the fraction of dye molecules associated to micelles as a function surfactant concentration.

In a third series of experiments, the cationic CTAC system was also studied together with the cationic dye Cresyl Violet (figure 2 open triangles). The results of the single-particle fits show considerably smaller increase in diffusion time signalling for a large number of free dye molecules even well above the *cmc*. The F-test indicates a much broader concentration range in which two fractions of particles coexist. Consistingly, the fraction of dye molecules associated with micelles, which is obtained from the two-particle fit, is quite small (Figure 3). It is very likely that repulsive electrostatic interaction is the origin of the ineffective physical aggregation of Cresyl Violet to the CTAC micelles.

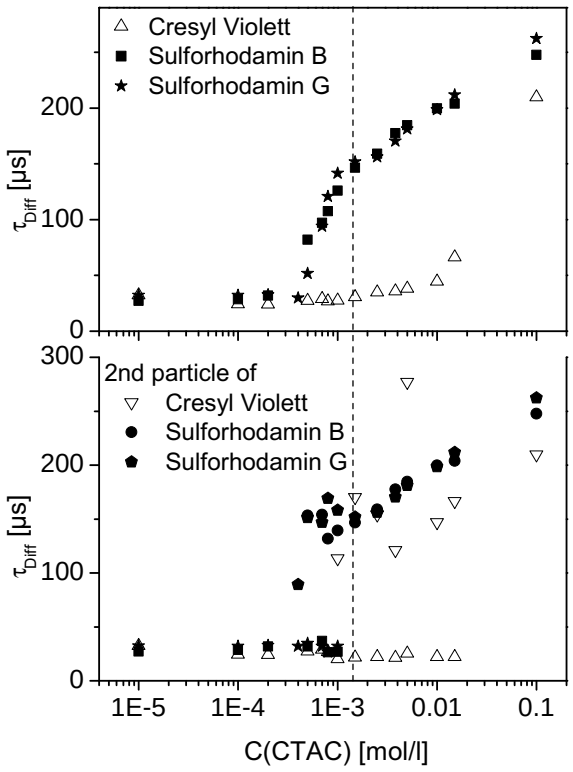

Figure 2: Diffusion times determined for CTAC solutions of different concentrations. The data result from fitting equation (3) to the experimental FCS autocorrelation functions. The dashed line indicates the *cmc* value determined by classical methods. The top graph shows the results obtained for single-particle fits ($K = 1$). The bottom graph shows data obtained when using a two particle fit. In order to determine whether a single or a two-particle fit should be used, we applied a hypothesis test (F-test) with a 5% confidence level. In case of anionic dye molecules the two-particle fit was required only at concentrations below the dashed vertical line. For the cationic dye molecule the two-particle fit was necessary up to a concentration of $1.5 \cdot 10^{-2}$ M.

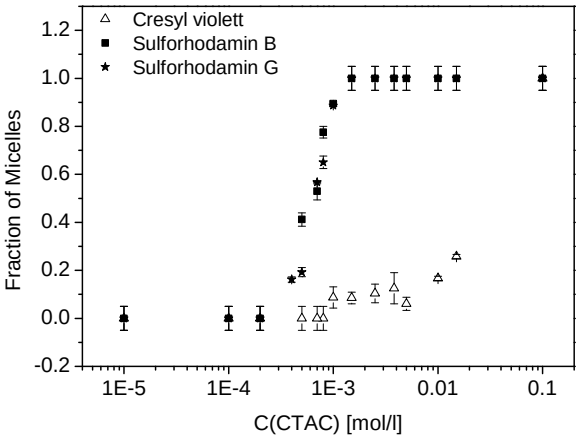

Figure 3: Fraction of dye molecules associated with micelles. Whenever a two-particle fit was required, the value of the fraction was taken from the fit. When using the single-particle model, the value was set to 0 at low and to 1 at high concentrations and an error of 5% was assumed. For the anionic Sulforhodamines we obtain a much faster increase than for the cationic dye Cresyl Violet.

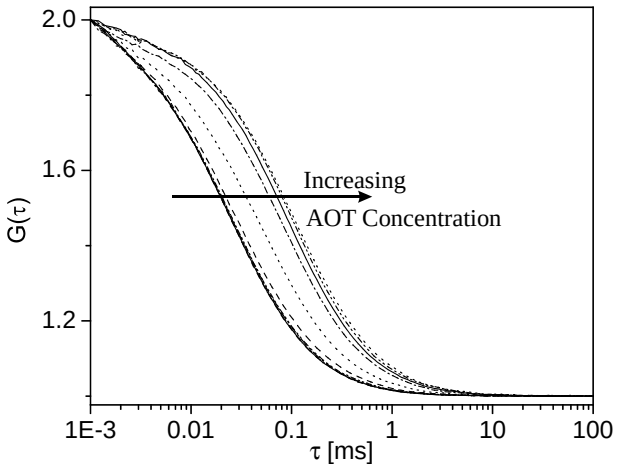

Figure 4: Normalised autocorrelation curves of AOT measured with Cresyl Violet. The five curves (—), corresponding to AOT concentrations of $2.3 \cdot 10^{-5}$ M to $8.0 \cdot 10^{-4}$ M., do not differ in shape and cannot be distinguished. At an AOT concentration of $1.5 \cdot 10^{-3}$ M (– – –) the diffusion time starts to increase. Here we find two particles with different diffusion times as shown in Figure 5. The curve at *cmc* ($2.5 \cdot 10^{-3}$ M) ($\cdots$) shows a diffusion time much longer than that of the free dye. With increasing AOT concentration the diffusion time converges to an upper limit of $\approx 100\,\mu$s.

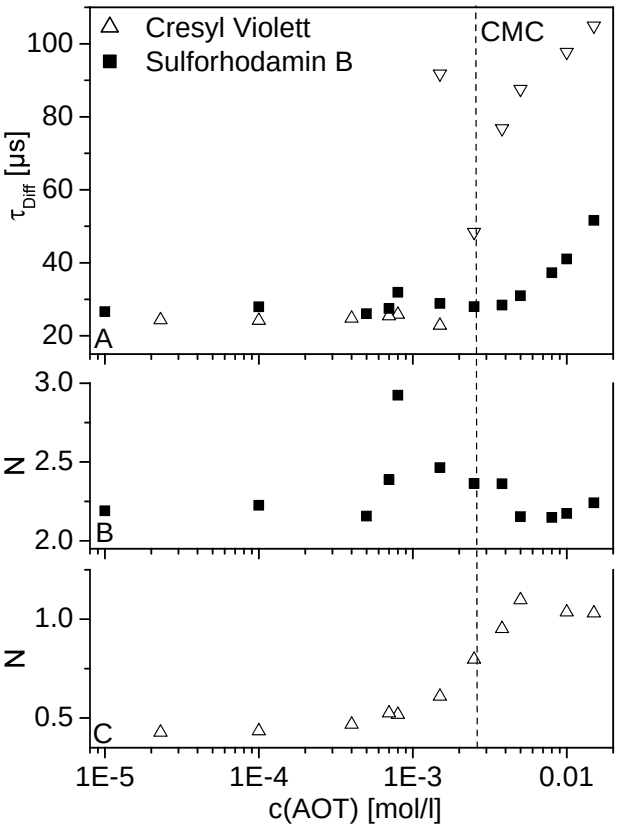

Figure 5: Characteristic diffusion times (A) and number of dye molecules in the excitation volume (B,C) for AOT solutions measured with Cresyl Violet and Sulforhodamine B, respectively. At low AOT concentrations only free Cresyl Violet molecules with a diffusion time of $\approx 25\,\mu$s are detected. At an AOT concentration of $1.5 \cdot 10^{-3}$ M a second fraction of particles with a diffusion time of $90\,\mu$s appears. At higher AOT concentrations, a single fraction of particles is observed with a diffusion time significantly longer than that of the free dye. The solution with Sulforhodamine B shows an increase in the diffusion time at $5{\cdot}10^{-3}$M. Figures B and C show the change in the number of fluorescent particles in the excitation volume. This number increases with increasing surfactant concentration for Cresyl Violet (C) but does not display any distinct trend for Sulforhodamine B (B).

Anionic surfactant. The anionic surfactant AOT was analysed with each of the dyes Cresyl Violet and Sulforhodamine B (figure 5).

Figure 4 shows the normalised autocorrelation curves of AOT analysed with Cresyl Violet in an AOT concentration range of $2.3 \cdot 10^{-5}$ M to $1.5 \cdot 10^{-2}$ M. At concentrations below $1.5 \cdot 10^{-3}$ M the autocorrelation signal is independent of surfactant concentration and resembles that of pure dye solutions. At concentrations between $1.5 \cdot 10^{-3}$ M and $3.8 \cdot 10^{-3}$ M the autocorrelation curves shift to higher diffusion times, indicating the

beginning of the formation of micelles. At $1.5{\cdot}10^{-3}$M free dye molecules and micelles coexist. At high surfactant concentrations the autocorrelation signal is, again, independent of surfactant concentration, indicating that all dye molecules are attached to micelles. The fitting of the data leads to the concentration dependence of the diffusion time shown in figure 5. At AOT concentrations below $1.5 \cdot 10^{-3}$ M the fit clearly yields a single fraction of molecules and thus, the observed diffusion time is attributed to free Cresyl Violet molecules. At $1.5 \cdot 10^{-3}$ M a second fraction of particles with a diffusion time of $91 \pm 9\,\mu s$ is observed. At and above $2.5 \cdot 10^{-3}$ M the data are, again, well represented by a single fraction with a characteristic diffusion time, which increases from a value of of $48.4{\pm}0.2\mu$s up to 104.9 ± 0.2 μs with increasing surfactant concentration. Thus, we find a one-to-one correspondence to the CTAC system measured with anionic dyes but with the polarities inversed: At low surfactant concentrations only free dye molecules are observed, while above the "classical" *cmc* all dye molecules are bound to micelles. At concentrations slightly below the *cmc* both free dye molecules and dye molecules bound to micelles are present in the solution.

Along the same lines the data obtained with the anionic dye Sulforhodamine B resemble the scenario observed for CTAC with the cationic dye Cresyl Violet. The data can be fitted with a single fraction of particles throughout the entire concentration range. The diffusion time increases only slightly and even above the classical *cmc* predominantly free dye molecules are observed.

We now turn to the discussion of the number of particles N within the excitation volume, which is the second important fitting parameter. According to equation (3) N is proportional to $1/(G(\tau) - 1)$ for single particle systems. Figure 5C shows the concentration dependence of the number of particles of Cresyl Violet. Although all solutions were prepared with identical dye concentration we observe an increase in the number of particles at the very concentration at which the diffusion time starts to increase. In other words, the concentration of dye molecules increases exactly at the onset of micelle formation. We attribute this to the ability of micelles to dissolve dye molecules that at low surfactant concentrations (below cmc) are adsorbed at the surfaces of the sample chamber.

Measuring the same surfactant with Sulforhodamine B, we do not observe a significant change in the number of particles beyond the statistical scatter in the data points (figure 5B).

Finally, we have analysed the surfactant sodium dodecyl sulfate (SDS) in the same manner and qualitatively find the same behaviour as seen for the AOT system (data not shown here).

Non-ionic surfactants. The non-ionic surfactant $C_{12}E_5$ shows a different behaviour than the ionic species. This surfactant could only be investigated by FCS with Rhodamine B Base. All other dyes studied with this surfactant did not show any change in diffusion time with increasing surfactant concentration. For Rhodamine B Base we de-

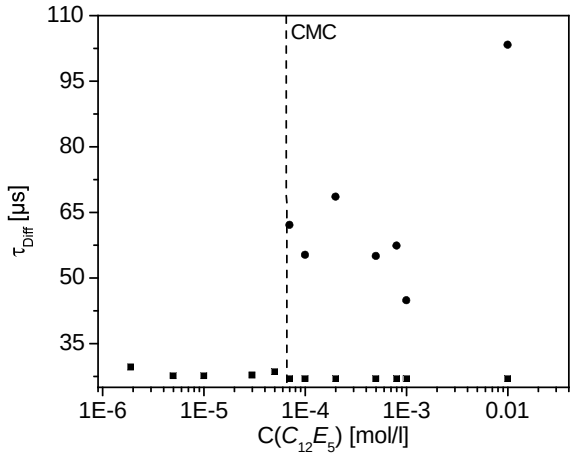

Figure 6: For the non-ionic surfactant up to a concentration of $6.5 \cdot 10^{-5}$M no interaction with the Rhodamin B Base can be noted. At this concentration a second particle with a longer diffusion time of $62 \pm 5 \mu$s and a fraction of 12% appears. With increasing surfactant concentration the fraction of this particle increases up to 80%.

tect a single fraction of particles (free dye molecules) at surfactant concentrations below $6.5 \cdot 10^{-5}$ M. At this concentration a second fraction of particles appears with a characteristic diffusion time of $\approx 60\ \mu$s. The fraction of this species is 12%. With increasing surfactant concentration the fraction increases up to 80%. The scatter in diffusion time of the micelles is relatively large and therefore its value is not specified.

4 Discussion

For all ionic surfactants studied here, we find a quite general behaviour. Well below the *cmc* only free dye molecules are observed. At and above the *cmc* value obtained by classical techniques, micelles are observed provided that the dye molecules are chosen to have the opposite polarity of the surfactant (see table 1). Well below and above the classical *cmc* the FCS autocorrelation function can be fitted by assuming a single fraction of particles corresponding to free dye molecules (at low concentrations) and to dye molecules bound to micelles (at high concentrations), respectively. In the concentration range between about 0.3 *cmc* and the actual *cmc* the situation is more complex and indeed more interesting. Here, the FCS data clearly indicate the coexistence of two fractions of dye molecules, one characterised by the diffusion time of the free dye and the other one characterised by a considerably larger diffusion time. This finding suggests the formation of aggregates already below the *cmc*. The width of the concentration range below the *cmc*, where aggregate formation is observed, varies slightly from system to system. However, the observation of aggregate formation below the *cmc* is a distinct result of the FCS experiments. In addition, for dye molecules suitable for *cmc* analysis a systematic increase of the number of particles within the excitation volume is observed when approaching the *cmc*.

	cmc [M]		
surfactant	cationic	anionic	conductivity
CTAC	7×10^{-3}	1.5×10^{-3}	1.46×10^{-3}
AOT	2.5×10^{-3}	4×10^{-3}	2.4×10^{-3}

Table 1: *cmc* values for the ionic surfactant systems as obtained from conductivity measurements and from FCS measurements with anionic and cationic dyes.

It is assumed that dye molecules located at the glass surface (and therefore not accessible to FCS) will be dissolved on the onset of micelle formation.
One may argue that the formation of micellar aggregates at surfactant concentrations below the classical *cmc* may be induced by the presence of the dye molecule and thereby be considered an artefact of the FCS technique [8]. In order to test this hypothesis, we have quantified the influence of Sulforhodamine G and Cresyl Violet on the micelle formation in CTAC solutions by conductivity measurements. The results are summarised in table 2. Irrespective of the polarity of the dye the addition of up to $1 \cdot 10^{-4}$ M of dye molecules did not lead to any measurable change of the *cmc*. Only at a dye concentration of $1 \cdot 10^{-3}$M a slight shift of the *cmc* is observed. We note that this concentration is five orders of magnitude larger than the concentration used for the FCS experiments. The shift is independent of the polarity of the dye molecule. In addition, the *cmc* happens to shift to higher concentrations in contrast to the observation of aggregation at concentrations *below* the *cmc*. Therefore it seems unlikely that the *pre-cmc* aggregation is induced by the dye. Thus, it is rather probable that a small number of aggregates is indeed formed below the *cmc*. The sensitivity of the FCS technique requires no more than $1 \cdot 10^{-9}$ M of aggregates in order to lead to the observed results. Such small number of aggregates could not be detected by any other technique.

The observation of pre-micellar aggregation may also raise the question of how to determine a critical micelle concentration from FCS experiments. For most practical purposes, we may define a *cmc* from FCS experiments as the lowest surfactant concentration at which the FCS autocorrelation function can be well represented by a single fraction of dye molecules bound to micelles. Because of the inherent experimental errors typical of the classical techniques for *cmc* determination, this value is in quantitative agreement with the published *cmc* values.
As for the choice of the dye molecules, our experiments indicate that different polarity between surfactant head group and dye molecule is advantageous. Indeed, the clearest results are obtained when anionic surfactants are combined with cationic dyes and *vice versa*. If the same polarity is chosen for surfactant and dye, the results are ambiguous and hardly any conclusions on the value of the *cmc* can be drawn. Our experiments further indicate that the ionic interaction between dye and surfactant rather than the solubility of the dye is the crucial parameter for a successful *cmc* measurement by FCS [2]. This fully accords with the finding that for

	cmc [M]	
Dye Conc. [M]	Sulforhodamine G	Cresyl violet
0	1.43×10^{-3}	1.43×10^{-3}
1×10^{-7}	1.4×10^{-3}	1.4×10^{-3}
1×10^{-4}	1.5×10^{-3}	1.4×10^{-3}
1×10^{-3}	3.0×10^{-3}	1.9×10^{-3}

Table 2: *cmc* values for the cationic surfactant CTAC with different concentrations of Sulforhodamine G and Cresyl Violet. The values are measured by conductivity.

non-ionic surfactants the detection of a *cmc* is more difficult and the change in the diffusion time is not as large as in ionic surfactants (see figure 6). In this case a second fraction of particles appears at $6.5 \cdot 10^{-5}$ M, which coincides with the *cmc* value obtained by classical methods.

5 Conclusion

We have explored the potential of fluorescence correlation spectroscopy (FCS) for the characterisation of surfactant aggregation in aqueous solution. Rather than using covalently dye-labelled surfactant molecules, we have investigated the physical aggregation of dye molecules to micelles. Our results show that FCS can be used for *cmc* determination in ionic surfactant systems provided that attractive ionic interactions are present. In consequence, the advantages characteristic of FCS (small sample volume, fast measurements) apply and make this technique an attractive alternative to the classical methods for *cmc* detection. We note that the high sensitivity of the technique (typical dye concentrations in the 10^{-8} M regime) allows the detection of *cmcs* in concentration regimes, which are not accessible by any of the classical techniques [10].

6 Acknowledgements

The authors acknowledge financial support through the *Deutsche Forschungsgesellschaft (SFB481, TP A11)* at Bayreuth University, through the *Reimund Stadler Minerva Center for Mesoscale Macromolecular Engineering* at Ben Gurion University and through the *Israel Science Foundation*. We thank H. Hänsel for fruitful discussions.

References

[1] Evans, D.F.; Wennerstrom, H *The Colloidal Domain where Physics, chemistry and Biology meet*, Wiley-VCH: New York, **1999**.

[2] Schuch, H.; Klingler, J.; Rossmanith, P.; Frechen, T.; Gerst, M.; Feldthusen, J.; Mueller, A. H. *Macromolecules*, **2000**, *33*, 1734–1740.

[3] Petersen, N. O. *Biophysical Journal*, **1986**, *49*, 809–815.

[4] Palmer, A. G.; Thompson, N. L. *Biophysical Journal*, **1987**, *52*, 257–270.

[5] Magde, D.; Webb, W. W.; Elson, E. *Physical Review Letters*, **1972**, *29*, 705–708.

[6] Elson, E. L.; Magde, D. *Biopolymers*, **1974**, *13*, 1–27.

[7] Magde, D.; Elson, E. L.; Webb, W. W. *Biopolymers*, **1974**, *13*, 29–61.

[8] Niu, S.; Gopidas K. R.; Turro N. J.; Gabor G. *Langmuir*, **1992**, *8*, 1271–1277.

[9] Schwille, P. *Cell Biochemistry and Biophysics*, **2001**, *34*, 383–408.

[10] Erhardt, R.; Böker, A.; Zettl, H.; Kaya, H.; Pyckhout-Hintzen, W.; Krausch, G.; Abetz, V.; Müller, A. H. E. *Macromolecules*, **2001**, *34*, 1069–1075.

[11] Meseth, U.; Wohland, T.; Rigler, R.; Vogel, H. *Biophysical Journal*, **1999**, *76*, 1619–1631.

[12] Lindman, B.; Puyal, MC.; Kamenka, N.; Rymden, R.; Stilbs, P. *Journal of Physical Chemistry*, **1984**, *88*, 5048–5057.